Fluctuations in the Cosmic Microwave Background

by

Matias Zaldarriaga

Submitted to the Department of Physics
in partial fulfillment of the requirements for the degree of

Doctor of Philosophy

at the

MASSACHUSETTS INSTITUTE OF TECHNOLOGY

May 1998

© Matias Zaldarriaga, MCMXCVIII. All rights reserved.

The author hereby grants to MIT permission to reproduce and
distribute publicly paper and electronic copies of this thesis
document in whole or in part, and to grant others the right to do so.

Author . . . .
Department of Physics
May 1, 1998

Certified by . . . .
Edmund Bertschinger
Professor
Thesis Supervisor

Certified by . . . .
Uroš Seljak
Harvard Smithsonian Center for Astrophysics Fellow
Co-Supervisor

Accepted by . . . .
Thomas J. Greytak
Associate Department Head for Education

Fluctuations in the Cosmic Microwave Background

by

Matias Zaldarriaga

Submitted to the Department of Physics
on May 1, 1998, in partial fulfillment of the
requirements for the degree of
Doctor of Philosophy

Abstract

In this thesis we investigate several aspects related to the theory of fluctuations in the Cosmic Microwave Background. We develop a new algorithm to calculate the angular power spectrum of the anisotropies which is two orders of magnitude faster than the standard Boltzmann hierarchy approach (Chapter 3). The new algorithm will become essential when comparing the observational results of the next generation of CMB experiments with theoretical predictions. The parameter space of the models is so large that an exhaustive exploration to find the best fit model will only be feasible with this new type of algorithm. We also investigate the polarization properties of the CMB field. We develop a new formalism to describe the statistics of the polarization variables that takes into account their spin two nature (Chapter 2). In Chapter 4 we explore several physical effects that create distinct features in the polarization power spectrum. We study the signature of the reionization of the universe and a stochastic background of gravitational waves. We also describe how the polarization correlation functions can be used to test the causal structure of the universe. Finally in Chapter 5 we quantify the amount of information the next generation of satellites can obtain by measuring both temperature and polarization anisotropies. We calculate the expected error bars on the cosmological parameters for the specifications of the MAP and Planck satellite missions.

Thesis Supervisor: Edmund Bertschinger
Title: Professor

Co-Supervisor: Uroš Seljak
Title: Harvard Smithsonian Center for Astrophysics Fellow

Acknowledgments

The time has come to thank all the people that made this work possible. I would like to thank Ed for his support and for giving me the freedom to pursue my own interests and collaborate with other people. When I arrived at MIT three years ago he suggested I should talk to Uroš. This proved to be an excellent suggestion. We started working on CMBFAST, not to enthusiastically at times, "well it is faster, so what?" we thought. Since then we have done several other things together and I think we had and are having a lot of fun. This is in my mind the most important thing. I have benefited immensely from talking and working with him, and hopefully this will continue into the future (if he has time to spend with the rest of us mortals now that he will become a distinguished professor).

I want to thank the members of my thesis committee for their suggestions, in particular Ed and Uroš for going carefully through the thesis to help improve my poor english. At MIT I enjoyed the company other graduate students and postdocs, Greg, Jim, Lam and Rennan among them.

I also want to thank David Spergel, several parts of this thesis were done in collaboration with him. It was a real pleasure to be able to work with him both during my visits to Princeton and over e-mail. I am very grateful for his support. I also want to thank John Bahcall for inviting me to Princeton for extended periods of time giving me the chance to work more closely with Dave and talk with the people at the IAS.

Several people have made these years much more fun. My "roommates" Alejandro, Fernando, Lucas and Susana share among them extremely important qualities. Formidable cooking abilities, exquisite taste for movies, obsession for cleanness, passion for sports and all other necessary characteristic of the perfect roommate. Patricio and our "ex-social chair" Pablo contributed to my well-being providing up to date party information and many fun weekday lunches. I also enjoyed keeping e-mail and phone contact with my old friends from the university and high school. Special thanks go to Fernando for his periodic updates on the absurd twists of argentinian politics

and his regular one line messages to learn how things were going, "JJ the great" for explaining me much more that I ever wanted to know about X-ray lasers and other perhaps more useful thoughts about life and Arturo, my friend from the "real world" with whom I have shared lots of things since our highschool days.

My parents and brothers have been a constant source of support. I enjoyed greatly our regular phone calls and visits which remind me that there are people who care about me back home. Hopefully the large "spatial distance" that separates us will not get in our way.

Contents

List of Figures

10

List of Tables

Chapter 1

Introduction

Since the initial discovery of anisotropies in the temperature of the microwave background radiation (CMB) by COBE in 1992 [1], the field has been transformed from a theoretical exercise to an active experimental area of research. The large amount of data from CMB experiments and other observations is beginning to revolutionize cosmology and has the potential of changing dramatically our view of the universe. In the next decade we might obtain answers to very fundamental questions such as the age, size and fate of the universe we live in. A few percent accuracy on most cosmological parameters seems achievable in the very near future, when the next CMB satellite missions fly. Should the inflationary paradigm prove to be correct, detailed measurements of the anisotropies coming from a number of ground based, balloon borne and satellite experiments could be used to determine a large set of cosmological parameters such as the density of the universe (Ω_0) or the Hubble constant (H_0) with unprecedented accuracy [2, 3, 4].

At the time the anisotropies in the microwave background were produced the universe was almost perfectly homogeneous. The fluctuations were at the 10^{-5} level and a linear approximation to the evolution equations suffices. This allows us to make very accurate predictions which are to be compared with experiments [5, 6, 7, 8]. Both the physics and the equations to be solved are relatively simple. CMB anisotropies are very clean from the theoretical point of view. This distinguishes them from other more local probes of cosmology where nonlinear effects complicate the theoretical

interpretation of the data.

A large number of other detections have followed the initial discovery by COBE [9, 10, 11, 12, 13, 14, 15, 16, 17, 18, 19, 20, 21]. Figure 1-1 shows all the results in the literature at the time this thesis was written (April 1998) in terms of the angular power spectrum of the temperature fluctuations, C_l. The easiest way to understand the meaning of the angular power spectrum is to consider a small region of the sky (for example the simulation in Figure 2-1). In that case the temperature map can be expanded in Fourier modes and the C_l is the power (mean square amplitude) as a function of the spatial frequency denoted with l. The rapid evolution of the field will make the figure outdated soon. We can expect new results from several ground and balloon borne experiments in the near future. The MAP satellite from NASA will be launched by the year 2000 and a few years later Planck from ESA should be launched too. The sensitivity and angular resolution of these satellites will be outstanding; MAP is expected to have a noise level of $20\mu K$ per resolution element (of approximately $0.3° \times 0.3°$). This translates into an uncertainty for each multipole due to noise in the detectors of $\Delta C_l \approx \sqrt{2/(2l+1)} \times (0.11\mu K)^2$. The Planck satellite will be equipped with very sensitive bolometers in the highest frequency channels (above 100 GHz). These channels will also have the best angular resolution, $\sim 0.1°$. For Planck the noise in the multipoles is expected to be $\Delta C_l \approx \sqrt{2/(2l+1)} \times (0.01\mu K)^2$. The high sensitivity of the experiments coupled to the accurate theoretical predictions are the primary motivation for using CMB anisotropies as a probe for cosmology.

The impressive angular resolution and noise levels of the future satellite missions create certain technical problems for the data analysis. The first step in the analysis is to go from the time ordered data (temperature or temperature differences measured by the different detectors on the satellite at each time) to maps of the CMB sky. A computationally feasible algorithm for doing this has recently been developed [22]. In the next step one wants to optimally measure the power spectrum of the anisotropies from the maps which have $10^5 - 10^6$ pixels. Direct evaluation of the likelihood function involves the inversion of a huge correlation matrix and is computationally too expensive. A practical algorithm solving this problem has recently been developed

16
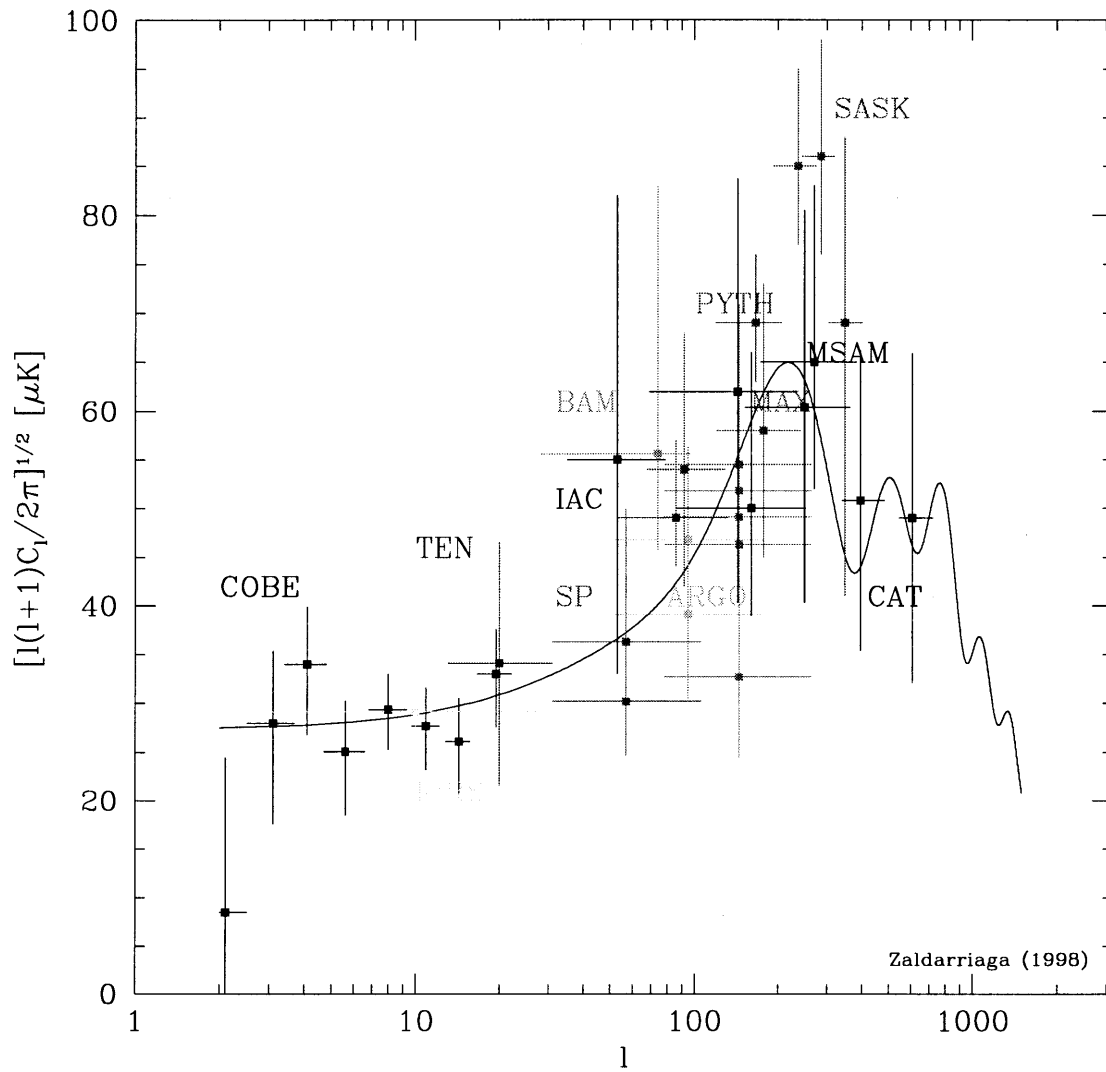
Figure 1-1: Compilation of measurements of the CMB anisotropy power spectra (from Tegmark http://www.sns.ias.edu/~max/cmb/experiments.html). The theoretical prediction for COBE normalized SCDM is shown for comparison.

for MAP [23].

Once the power spectrum of the anisotropies has been measured we would like to find the model that best fits the data and the confidence intervals on the model parameters. The power spectrum of the CMB anisotropies depends on a large number of parameters. We would like to learn about the total density of the universe Ω_0, Hubble constant H_0, baryon density Ω_b, the cosmological constant Λ and the amplitude and scale dependence of the initial fluctuations. The exploration of this vast parameter space that characterizes the models will require many calculations of the theoretical power spectrum. This is computationally too expensive with the usual Boltzmann codes which need to solve a large system of differential equations at a large number of wavenumbers. This computational barrier was overcome by the development of a new algorithm based on a line of sight integral [8] which we present in Chapter 3. This algorithm has proved very useful for the rapid exploration of the phenomenology of CMB anisotropies. The power spectrum for any cosmological model can be obtained in only a few minutes on a normal workstation. It has also been extended to include active sources (as opposed to the primeval potential fluctuations of standard models), so that it can be used to make accurate predictions of the anisotropies produced by topological defect models [24]. The development of this new line of sight algorithm is one of the most important results presented in this thesis.

There is still a need to develop ways of extracting additional information from the CMB maps not encoded in the temperature power spectrum, which could prove important if topological defects or other non-gaussian sources are shown to be the cause of the anisotropies. If inflationary models are correct, the power spectrum fully describes the statistical properties of the primary anisotropies, but secondary effects like gravitational lensing can leave interesting information in higher moments. These effects tend to be small, at least on large angular scales.

The CMB radiation field is also expected to be linearly polarized due to Thomson scattering of the photons with free electrons [25, 26, 27, 28, 29, 30]. The polarization of the CMB can provide in principle the same information about our universe that will become available from the temperature maps. The main disadvantage of polarization

is that the CMB is predicted to be only $1 - 10\%$ polarized depending on the angular scale. Future satellite missions will have the required sensitivity and the most likely source of problems will be contamination from galactic foregrounds. The nature and level of the foregrounds for polarization remain uncertain and we may have to wait until the satellites fly for a definitive answer. There will also be several ground based experiments before the satellites, eg. [35, 36]. They may help determine the level of foreground contamination to be expected for the satellite missions and may also detect cosmological polarization.

The detection of polarization is challenging but nevertheless the rewards can be great. We have shown that polarization may be able to constrain the ionization history of the universe very accurately [31]. We know that the light from the first generation of objects reionized the universe after recombination, but the time when this occurs remains very uncertain. The scatterings of the CMB photons with the electrons after reionization will leave a signature in the CMB polarization that could be our first direct detection of the epoch of reionization. We will also show that large angular scale correlations in the polarization can be used to test the causal structure of the universe and could provide a direct test of the inflationary paradigm [32]. Finally the pattern of the polarization vectors can be used to detect the presence of a stochastic background of gravitational waves [33, 34]. We will discuss all of these issues in Chapter 4.

The polarization of the CMB has the potential of providing very interesting tests for our theories of the universe. The study of the properties of the polarization is a unifying theme of this thesis. In Chapter 2 we introduce the physics of CMB anisotropy and polarization and we develop a statistical description for the CMB polarization field. Chapter 3 describes the algorithm for computing both temperature and polarization spectra. In Chapter 4 we look at several ways in which polarization can provide extra information not available in the temperature power spectrum. In Chapter 5 we quantify the benefits of using polarization for the determination of cosmological parameters by the MAP and Planck satellites.

The anisotropies in the CMB radiation field encode an enormous amount of infor-

mation about the universe we live in. In the next years the main driver of the field will be the rapid progress of experimental research. The results of these experiments will be used in conjunction with the results of other observations to test our theories of the universe with an accuracy which was unimaginable just a decade ago. It is a great time for cosmology, the availability of large quantities of data is making all the difference and hopefully will provide several interesting surprises.

Bibliography

[1] G. F. Smoot, C. L. Bennet, A. Kogut, E. L. Wright, J. Aymon, N. W. Boggess, E. S. Cheng, G. De Amici, S. Gulkis, M. G. Hauser, G. Hinshaw, P. D. Jackson, M. Janssen, E. Kaita, T. Kensall, P. Keegtra, C. Lineweaver, K. Loewenstein, P. Lubin, J. Mather, S. S. Meyer, S. H. Moseley, T. Murdock, L. Rokke, R. F. Silverberg, L. Tenorio, R. Weiss & D. T. Wilkinson, Astrophys. J. **396**, L1 (1992).

[2] G. Jungman, M. Kamionkowski, A. Kosowsky, & D. N. Spergel, Phys. Rev. Lett. **76**, 1007 (1996); Phys. Rev. D **54** 1332 (1996).

[3] J. R. Bond, G. Efstathiou & M. Tegmark, Mon. Not. R. Astron. Soc. **291**, 33 (1997).

[4] M. Zaldarriaga, D. N. Spergel & U. Seljak, Astrophys. J. **488**, 1 (1997).

[5] J. R. Bond & G. Efstathiou, Mon. Not. R. Soc. **226**, 655 (1987).

[6] W. Hu, D. Scott, N. Sugiyama & M. White, Phys.Rev. D **52** , 5498 (1995).

[7] J. R. Bond, 1996, in Cosmology and Large Scale Structure, ed R. Schaeffer et. al. (Elsevier Science: Netherlands).

[8] U. Seljak & M. Zaldarriaga, Astrophys. J. **469**, 7 (1996).

[9] K. Ganga et al., Astrophys. J., **432**, L15 (1994).

[10] Hancock et al., Mon. Not. R. Astron. Soc. **289**, 505 (1997).

[11] J. O. Gundersen et al., Astrophys. J. **443**, L57 (1995).

[12] G. S. Tucker et al., Astrophys. J. **475**, 73 (1997).

[13] S. Masi et al., Astrophys. J. **463**, L47 (1996).

[14] S. T. Tanaka et al., Astrophys. J. **468**, L81 (1996).

[15] S. R. Platt et al, Bull. American Astron. Soc. **191** 112 (1997).

[16] B. Femenia et al., preprint astro-ph/9711225.

[17] L. Piccirillo & P. Calisse, Astrophys. J. **411**, 411 (1993).

[18] E. S. Cheng et al., Astrophys. J. **488**, L59 (1997).

[19] C. B. Netterfield et al., Astrophys. J. **474**, 47 (1997).

[20] P. F. Scott et al., Astrophys. J. **461**, L1 (1996).

[21] K. Ganga et al.,Astrophys. J. **484**, 517 (1997).

[22] E. L. Wright, G. Hinshaw & C. L. Bennett, Astrophys. J. **458**, L53 (1996).

[23] S. P. Oh, D. N. Spergel & G. Hinshaw, in preparation.

[24] U. Pen, U. Seljak & N. Turok, Phys. Rev. Lett. **79**. 1611 (1997)

[25] J. R. Bond & G. Efstathiou, Mon. Not. R. Astr. Soc. **226**, 655 (1987).

[26] R. Crittenden, R. L. Davis & P. J. Steinhardt, Astrophys. J. **417**, L13 (1993).

[27] R. A. Frewin, A. G. Polnarev & P. Coles, Mon. Not. R. Astron. Soc. **266**, L21 (1994).

[28] Coulson, D., Crittenden, R. G., & Turok, N. Phys. Rev. Lett. **73**, 2390(1994).

[29] R. G. Crittenden, D. Coulson & N. G. Turok, Phys. Rev. D **52**, 5402 (1995).

[30] M. Zaldarriaga & D. Harari, Phys. Rev. D **52**, 3276 (1995).

[31] M. Zaldarriaga, Phys. Rev. D **55**, 2822 (1997).

[32] D. N. Spergel, & M. Zaldarriaga, Phys. Rev. Lett. **79**, 2180 (1997).

[33] U. Seljak & M. Zaldarriaga, Phys. Rev. Lett. **78**, 2054 (1997).

[34] M. Kamionkowski, A. Kosowsky & A. Stebbins, Phys. Rev. D **55** 7368 (1997).

[35] B. Keating et al., Astrophys. J. **495**, 580 (1998).

[36] Visit http://astro.caltech.edu/ lgg/polatron/psci.html for information on pola-tron.

Chapter 2

Statistical Treatment of CMB

Fluctuations[1]

In this chapter we will develop the statistical description of the CMB radiation field. We will enphasize the spin 2 nature of polarization and the mathematical tools needed to analyze it. We will present a physical interpretation of the new variables introduced by making a connection with the theory of gravitational lensing and a brief summary of the mechanisms that can produce anisotropies and polarization in our universe.

Figure 2-1 shows a simulated map of CMB anisotropies (both temperature and polarization) for the standard cold dark matter model (SCDM)[2]. The anisotropies can tell us about the state of the universe at a very early time, only 300.000 years after the big bang when hydrogen recombined and the universe became transparent to the CMB photons. Since then the photons have been able to travel an enormous distance, approximately 10^{10} light years. Thus the CMB anisotropies map the most distant parts of our universe at a very early stage.

The main cause for the temperature anisotropies are fluctuations in the photon density at recombination. We see more photons coming from what were denser regions, producing a hot spot in the map. Photons coming from different directions

---

[1]Partially based on M. Zaldarriaga & U. Seljak, Phys. Rev. D **55**, 1830 (1997).

[2]This model has $\Omega_0 = 1$, $\Omega_\Lambda = 0$, $\Omega_b = 0.05$, $H_0 = 50$ km/sec/Mpc, a COBE normalized power spectrum of initial fluctuations with a spectral index $n = 1$ and no stochastic background of gravitational waves.

also come from regions which were moving at different velocities relative to us; the consequent difference in the Doppler shifts they suffered also cause anisotropies. Gravitational redshift is the last source of anisotropies. Fluctuations in the gravitational potential will lead to different amounts of gravitational redshift for photons coming from different parts of the universe. We can also consider the presence of a stochastic background of gravitational waves. They will also create temperature anisotropies as photons get redshifted or blueshifted by different amounts according to their direction of propagation relative to that of the gravity wave.

Polarization is produced by Thomson scattering of the CMB photons and electrons. Thus it can only be produced when hydrogen is ionized. Furthermore only radiation that is anisotropic can lead to non zero polarization because by symmetry if the radiation incident on an electron is isotropic there is no preferred direction for the polarization of the scattered light. The sources of anisotropies described in the previous paragraph will create some polarization when Thomson scattering is present.

2.1   Characterization of the Radiation Field

The aim of this section is to develop the mathematical tools needed to describe the CMB anisotropies. We will emphasize the description of the polarization which is new to this thesis. The CMB anisotropy field is characterized by a 2×2 intensity tensor I_{ij}. For convinience we normalize this tensor so it represents the fluctuations in units of the mean intensity ($I_{ij} = \delta I / I_0$), it is dimensionless. The intensity tensor is a function of direction on the sky $\hat{n}$ and two directions perpendicular to $\hat{n}$ that are used to define its components ($\hat{e}_1, \hat{e}_2$). The Stokes parameters Q and U are defined as $Q = (I_{11} - I_{22})/4$ and $U = I_{12}/2$, while the temperature anisotropy is given by $T = (I_{11} + I_{22})/4$ (the factor of 4 relates fluctuations in the intensity with those in the temperature, $I \propto T^4$). In Figure 2-1 we represent the polarization using vectors with magnitude $P = \sqrt{Q^2 + U^2}$ that form an angle $\alpha = \frac{1}{2} \arctan(U/Q)$ with $\hat{e}_1$. In principle the fourth Stokes parameter V that describes circular polarization would also be needed, but in cosmology it can be ignored because it cannot be generated through Thomson

scattering[3]. While the temperature is invariant under a right handed rotation in the plane perpendicular to direction $\hat{n}$, Q and U transform under rotation by an angle ψ as

$$
\begin{aligned}
Q' &= Q\cos 2\psi + U\sin 2\psi \\
U' &= -Q\sin 2\psi + U\cos 2\psi
\end{aligned}
\tag{2.1}
$$

where $\hat{e}'_1 = \cos\psi\,\hat{e}_1 + \sin\psi\,\hat{e}_2$ and $\hat{e}'_2 = -\sin\psi\,\hat{e}_1 + \cos\psi\,\hat{e}_2$. We can construct two quantities from the Stokes Q and U parameters that have a definite value of spin (see Appendix A for a review of spin-weighted functions and their properties),

$$
(Q \pm iU)'(\hat{n}) = e^{\mp 2i\psi}(Q \pm iU)(\hat{n}).
\tag{2.2}
$$

We may therefore expand each of the quantities in the appropriate spin-weighted basis

$$
\begin{aligned}
T(\hat{n}) &= \sum_{lm} a_{T,lm} Y_{lm}(\hat{n}) \\
(Q + iU)(\hat{n}) &= \sum_{lm} a_{2,lm}\, _2Y_{lm}(\hat{n}) \\
(Q - iU)(\hat{n}) &= \sum_{lm} a_{-2,lm}\, _{-2}Y_{lm}(\hat{n}).
\end{aligned}
\tag{2.3}
$$

Q and U are defined at each direction $\hat{n}$ with respect to the spherical coordinate system $(\hat{e}_\theta, \hat{e}_\phi)$. Using the first equation in (A.5) one can show that the expansion coefficients for the polarization variables satisfy $a^*_{-2,lm} = a_{2,l-m}$. For the temperature the relation is $a^*_{T,lm} = a_{T,l-m}$.

---

[3]The presence of a large magnetic field at recombination could generate a small component of circular polarization.
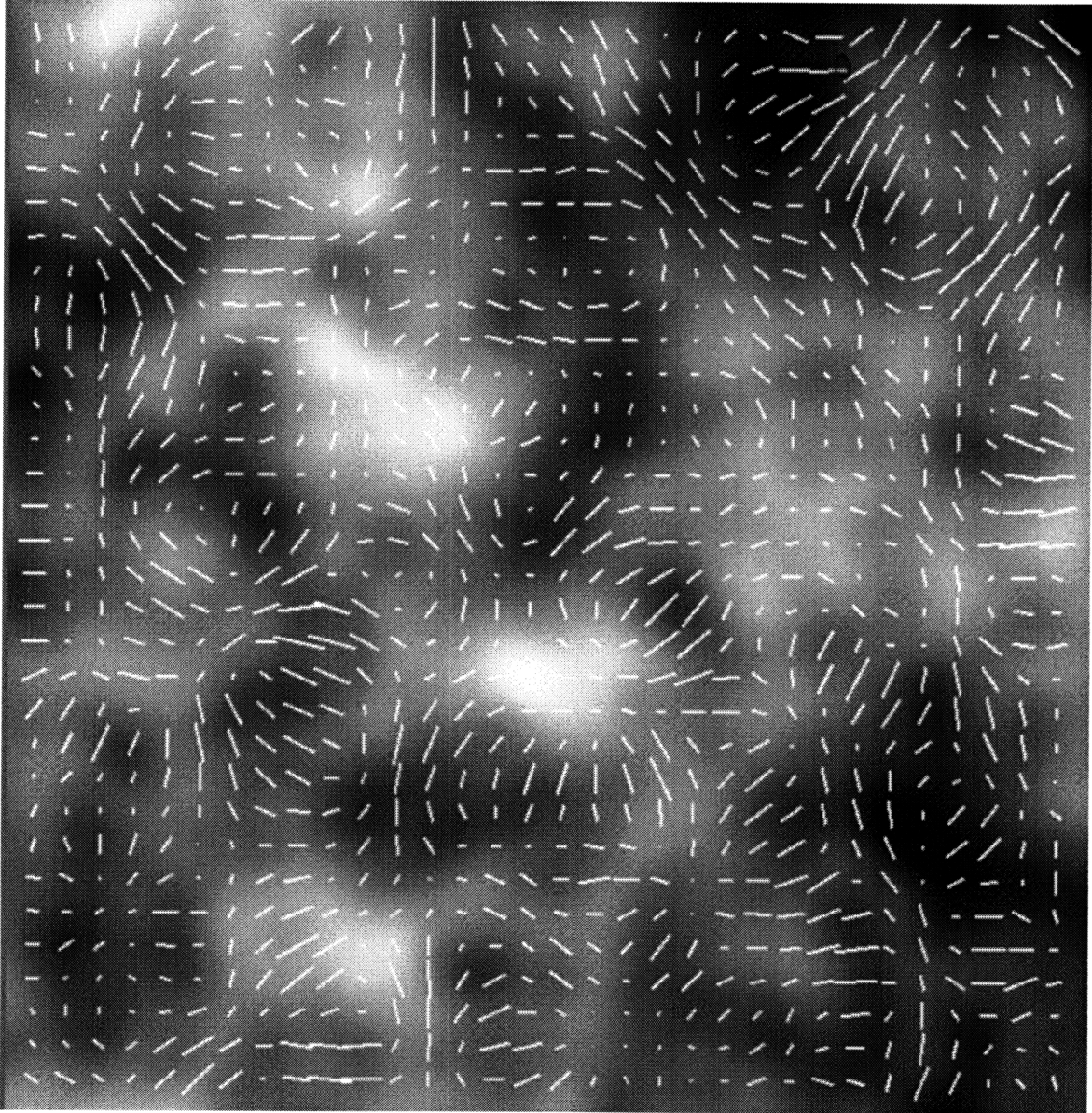
Figure 2-1: Simulated temperature and polarization map for SCDM ($2.5^\circ \times 2.5^\circ$ field). The polarization vectors are shown together with the map of the temperature. The temperature ranges from $-1690\mu K < T < 1810\mu K$ while the maximum amplitude of the polarization vectors is $P = 128\mu K$.

The main difficulty when computing the power spectrum of polarization in the past originated in the fact that the Stokes parameters are not invariant under rotations in the plane perpendicular to $\hat{n}$ (equation 2.1). The usual approach starts by expanding all perturbations in Fourier modes with wavevector $\boldsymbol{k}$. While Q and U are easily calculated in a coordinate system where the wavevector $\boldsymbol{k}$ is parallel to $\hat{z}$, the superposition of the different modes is complicated by the behavior of Q and U under rotations. For each wavevector $\boldsymbol{k}$ and direction on the sky $\hat{n}$ one has to rotate the Q and U parameters from this $\boldsymbol{k}$ and $\hat{n}$ dependent basis where the calculation is done into a fixed basis on the sky before adding them. Only in the small scale limit is this process well defined. This approximation had always been assumed in previous work [1, 2, 3, 4, 5, 6]. However, one can use the spin raising and lowering operators $\eth$ and $\bar{\eth}$ defined in Appendix A to obtain spin zero quantities. These have the advantage of being rotationally invariant like the temperature and no ambiguities connected with the rotation of coordinate system arise. Acting twice with $\eth$, $\bar{\eth}$ on $Q \pm iU$ in equation (2.3) leads to

$$\bar{\eth}^{2}(Q+iU)(\hat{n}) = \sum_{lm} \left[\frac{(l+2)!}{(l-2)!}\right]^{1/2} a_{2,lm}Y_{lm}(\hat{n})$$

$$\eth^{2}(Q-iU)(\hat{n}) = \sum_{lm} \left[\frac{(l+2)!}{(l-2)!}\right]^{1/2} a_{-2,lm}Y_{lm}(\hat{n}). \tag{2.4}$$

The expressions for the expansion coefficients are

$$a_{T,lm} = \int d\Omega\, Y_{lm}^{*}(\hat{n})T(\hat{n})$$

$$a_{2,lm} = \int d\Omega\, {}_{2}Y_{lm}^{*}(\hat{n})(Q+iU)(\hat{n})$$

$$= \left[\frac{(l+2)!}{(l-2)!}\right]^{-1/2} \int d\Omega\, Y_{lm}^{*}(\hat{n})\bar{\eth}^{2}(Q+iU)(\hat{n})$$

$$a_{-2,lm} = \int d\Omega\, {}_{-2}Y_{lm}^{*}(\hat{n})(Q-iU)(\hat{n})$$

$$= \left[\frac{(l+2)!}{(l-2)!}\right]^{-1/2} \int d\Omega\, Y_{lm}^{*}(\hat{n})\eth^{2}(Q-iU)(\hat{n}). \tag{2.5}$$

Instead of $a_{\pm 2, lm}$ it is convenient to introduce their linear combinations [7],

$$
\begin{aligned}
a_{E,lm} &= -(a_{2,lm} + a_{-2,lm})/2 \\
a_{B,lm} &= i(a_{2,lm} - a_{-2,lm})/2.
\end{aligned}
\tag{2.6}
$$

We can define two quantities in real space,

$$
\begin{aligned}
E(\hat{n}) &= \sum_{l,m} a_{E,lm}\, Y_{lm}(\hat{n}) \\
B(\hat{n}) &= \sum_{l,m} a_{B,lm}\, Y_{lm}(\hat{n}).
\end{aligned}
\tag{2.7}
$$

The temperature is a scalar quantity under a rotation of the coordinate system, $T'(\hat{n}' = \mathcal{R}\hat{n}) = T(\hat{n})$, where $\mathcal{R}$ is the rotation matrix. We denote with a prime the quantities in the transformed coordinate system. Equation (2.5) shows that up to an l-dependent factor $a_{\pm 2, lm}$ are the expansion coefficients of two spin zero quantities $\bar{\eth}^{\,2}(Q + iU)$ and $\eth^{\,2}(Q - iU)$. As a result $E(\hat{n})$ and $B(\hat{n})$ are also invariant under rotations.

It is interesting to analyze the behavior of E and B under a parity transformation. We will consider the case where we reverse the sign of the x coordinate but leave the others unchanged. In spherical coordinates this amounts to changing the sign of ϕ while θ and r remain the same. Under this transformation $\hat{e}'_\phi = -\hat{e}_\phi$ and $\hat{e}'_\theta = \hat{e}_\theta$ so the Stokes parameters transform as $Q'(\hat{n}') = Q(\hat{n})$ and $U'(\hat{n}') = -U(\hat{n})$. With the aid of equation (A.2) we can show that

$$
\begin{aligned}
\bar{\eth}^{\,2}(Q + iU)'(\hat{n}') &= \eth^{\,2}(Q - iU)(\hat{n}) \\
\eth^{\,2}(Q - iU)'(\hat{n}') &= \bar{\eth}^{\,2}(Q + iU)(\hat{n}).
\end{aligned}
\tag{2.8}
$$

This implies that (equations 2.5 2.6 and 2.7),

$$
\begin{aligned}
E'(\hat{n}') &= E(\hat{n}) \\
B'(\hat{n}') &= -B(\hat{n}).
\end{aligned}
\tag{2.9}
$$

These two new variables behave differently under parity: while E remains unchanged B changes sign [7], in analogy with electric and magnetic fields. The sign convention in equation (2.6) makes these expressions consistent with those defined previously in the small scale limit [5].

To characterize the statistics of the CMB perturbations only four power spectra are needed, those for T, E, B and the cross correlation between T and E. The cross correlation between B and E or B and T vanishes because B has the opposite parity to T or E. The power spectra are defined as the rotationally invariant quantities

$$
\begin{aligned}
C_{Tl} &= \frac{1}{2l+1} \sum_m \langle a^*_{T,lm} a_{T,lm} \rangle \\
C_{El} &= \frac{1}{2l+1} \sum_m \langle a^*_{E,lm} a_{E,lm} \rangle \\
C_{Bl} &= \frac{1}{2l+1} \sum_m \langle a^*_{B,lm} a_{B,lm} \rangle \\
C_{Cl} &= \frac{1}{2l+1} \sum_m \langle a^*_{T,lm} a_{E,lm} \rangle
\end{aligned}
\tag{2.10}
$$

in terms of which,

$$
\begin{aligned}
\langle a^*_{T,l'm'} a_{T,lm} \rangle &= C_{Tl} \delta_{l'l} \delta_{m'm} \\
\langle a^*_{E,l'm'} a_{E,lm} \rangle &= C_{El} \delta_{l'l} \delta_{m'm} \\
\langle a^*_{B,l'm'} a_{B,lm} \rangle &= C_{Bl} \delta_{l'l} \delta_{m'm} \\
\langle a^*_{T,l'm'} a_{E,lm} \rangle &= C_{Cl} \delta_{l'l} \delta_{m'm} \\
\langle a^*_{B,l'm'} a_{E,lm} \rangle &= \langle a^*_{B,l'm'} a_{T,lm} \rangle = 0.
\end{aligned}
\tag{2.11}
$$

The brackets $\langle \cdots \rangle$ are ensemble averages.

2.1.1 Correlators in Real Space

Sometimes it is useful to investigate the correlations in real space. These expressions are needed, for example, to write the likelihood function of a measured CMB map.

We rewrite equation (2.3) as

$$
\begin{aligned}
T(\hat{n}) &= \sum_{lm} a_{T,lm} \, Y_{lm}(\hat{n}) \\
Q(\hat{n}) &= -\sum_{lm} a_{E,lm} \, X_{1,lm}(\hat{n}) + i a_{B,lm} \, X_{2,lm}(\hat{n}) \\
U(\hat{n}) &= -\sum_{lm} a_{B,lm} \, X_{1,lm}(\hat{n}) - i a_{E,lm} \, X_{2,lm}(\hat{n}).
\end{aligned}
\tag{2.12}
$$

We have introduced $X_{1,lm}(\hat{n}) = (\, _2Y_{lm} + \, _{-2}Y_{lm})/2$ and $X_{2,lm}(\hat{n}) = (\, _2Y_{lm} - \, _{-2}Y_{lm})/2$. They satisfy $X_{1,lm}^* = X_{1,l-m}$ and $X_{2,lm}^* = -X_{2,l-m}$ which together with $a_{E,lm} = a_{E,l-m}^*$ and $a_{B,lm} = a_{B,l-m}^*$ make Q and U real quantities.

In fact, $X_{1,lm}(\hat{n})$ and $X_{2,lm}(\hat{n})$ can be written in the form $X_{1,lm}(\hat{n}) = \sqrt{(2l+1)/4\pi} \, F_{1,lm}(\theta) \, e^{im\phi}$ and $X_{2,lm}(\hat{n}) = \sqrt{(2l+1)/4\pi} \, F_{2,lm}(\theta) \, e^{im\phi}$, where $F_{(1,2),lm}(\theta)$ can be expressed in terms of Legendre polynomials [8] [4]:

$$
\begin{aligned}
F_{1,lm}(\theta) &= 2\sqrt{\frac{(l-2)!(l-m)!}{(l+2)!(l+m)!}} \Bigg\{ -\left[\frac{l-m^2}{\sin^2\theta} + \frac{1}{2}l(l-1)\right] P_l^m(\cos\theta) \\
&\quad + (l+m)\frac{\cos\theta}{\sin^2\theta} P_{l-1}^m(\cos\theta) \Bigg\} \\
F_{2,lm}(\theta) &= 2\sqrt{\frac{(l-2)!(l-m)!}{(l+2)!(l+m)!}} \, \frac{m}{\sin^2\theta} \Big[-(l-1)\cos\theta P_l^m(\cos\theta) \\
&\quad + (l+m) P_{l-1}^m(\cos\theta) \Big].
\end{aligned}
\tag{2.13}
$$

Note that $F_{2,lm}(\theta) = 0$ if $m = 0$, a necessary condition given that the Stokes parameters are real.

The correlation functions can be calculated using equations (2.11) and (2.12),

$$
\begin{aligned}
\langle T(1)T(2) \rangle &= \sum_l C_{Tl} \left[\sum_m {}_0Y_{lm}^*(1) \, {}_0Y_{lm}(2) \right] \\
\langle Q(1)Q(2) \rangle &= \sum_l C_{El} \left[\sum_m X_{1,lm}^*(1) X_{1,lm}(2) \right] + C_{Bl} \left[\sum_m X_{2,lm}^*(1) X_{2,lm}(2) \right] \\
\langle U(1)U(2) \rangle &= \sum_l C_{El} \left[\sum_m X_{2,lm}^*(1) X_{2,lm}(2) \right] + C_{Bl} \left[\sum_m X_{1,lm}^*(1) X_{1,lm}(2) \right]
\end{aligned}
$$

---

[4]A subroutine that calculates these functions is available at http://arcturus.mit.edu/~matiasz/CMBFAST .

$$\langle T(1)Q(2)\rangle = \sum_l C_{Cl}\left[\sum_m {}_0Y^*_{lm}(1)X_{1,lm}(2)\right]$$

$$\langle T(1)U(2)\rangle = i\sum_l C_{Cl}\left[\sum_m {}_0Y^*_{lm}(1)X_{2,lm}(2)\right] \qquad (2.14)$$

where 1 and 2 stand for the two directions in the sky $\hat{n}_1$ and $\hat{n}_2$. These expressions can be further simplified using the addition theorem for the spin harmonics,

$$\sum_m {}_{s_1}\bar{Y}^*_{lm}(\hat{n}_1)\, {}_{s_2}Y_{lm}(\hat{n}_2) = \sqrt{\frac{2l+1}{4\pi}}\, {}_{s_2}Y_{l-s_1}(\beta,\psi_1)e^{-is_2\psi_2}, \qquad (2.15)$$

where β is the angle between $\hat{n}_1$ and $\hat{n}_2$, and (ψ_1,ψ_2) are the angles $(\hat{e}_\theta,\hat{e}_\phi)$ at $\hat{n}_1$ and $\hat{n}_2$ need to be rotated to become aligned with the great circle going through both points. In the case of the temperature, equation (2.15) gives the usual relation,

$$\langle T_1 T_2\rangle = \sum_l \frac{2l+1}{4\pi}C_{Tl}P_l(\cos\beta). \qquad (2.16)$$

For polarization the addition relations for $X_{1,lm}$ and $X_{2,lm}$ are calculated from equation (2.15),

$$\sum_m X^*_{1,lm}(1)X_{1,lm}(2) = \frac{2l+1}{4\pi}\left[F_{1,l2}(\beta)\cos 2\psi_1\cos 2\psi_2 - F_{2,l2}(\beta)\sin 2\psi_1\sin 2\psi_2\right]$$

$$\sum_m X^*_{2,lm}(1)X_{2,lm}(2) = \frac{2l+1}{4\pi}\left[F_{1,l2}(\beta)\sin 2\psi_1\sin 2\psi_2 - F_{2,l2}(\beta)\cos 2\psi_1\cos 2\psi_2\right]$$

$$\sum_m X^*_{1,lm}(1)X_{2,lm}(2) = i\frac{2l+1}{4\pi}\left[F_{1,l2}(\beta)\sin 2\psi_1\cos 2\psi_2 + F_{2,l2}(\beta)\cos 2\psi_1\sin 2\psi_2\right]$$

$$\sum_m {}_0Y^*_{lm}(1)X_{1,lm}(2) = \frac{2l+1}{4\pi}F_{1,l0}(\beta)\cos 2\psi_2$$

$$\sum_m {}_0Y^*_{lm}(1)X_{2,lm}(2) = -i\frac{2l+1}{4\pi}F_{1,l0}(\beta)\sin 2\psi_2. \qquad (2.17)$$

We can equivalently write $F_{1,l0}(\beta) = \sqrt{(l-2)!/(l+2)!}\, P^2_l(\beta)$.

The correlations in equation (2.14) with the sums given by equation (2.17) are all that is needed to analyze any given experiment. These relations are simple to understand [8]; the natural coordinate system to express the correlations is one in which the $\hat{e}_1$ vector for each point (1 and 2) is aligned with the great circle connecting

the two directions, the $\hat{e}_2$ vectors perpendicular to the $\hat{e}_1$. With this choice of reference frame we have [8],

$$
\begin{aligned}
\langle Q_r(1)Q_r(2)\rangle &= \sum_l \frac{2l+1}{4\pi}\Big[C_{El}F_{1,l2}(\beta) - C_{Bl}F_{2,l2}(\beta)\Big] \\
\langle U_r(1)U_r(2)\rangle &= \sum_l \frac{2l+1}{4\pi}\Big[C_{Bl}F_{1,l2}(\beta) - C_{El}F_{2,l2}(\beta)\Big] \\
\langle T(1)Q_r(2)\rangle &= -\sum_l \frac{2l+1}{4\pi}C_{Cl}F_{1,l0}(\beta) \\
\langle T(1)U_r(2)\rangle &= 0.
\end{aligned}
\tag{2.18}
$$

The subscript r here indicates that the Stokes parameters are measured in this particular coordinate system. We can use the transformation laws in equation (2.1) to write (Q, U) in terms of (Q_r, U_r). When we use equation (2.18) for their correlations we recover our final result given by equations (2.14) and (2.17).

2.1.2 Small Scale Limit

There are several temperature and polarization experiments being planned or built. Many of them will attempt to measure the anisotropies in small patches of the sky. In this limit the sky can be approximated as flat and spherical harmonics can be replaced by Fourier modes. This has important practical benefits because it allows the use of the fast Fourier transforms to reduce computational time. In this section we will study how polarization is described in this limit. In the small scale limit one considers only directions in the sky $\hat{n}$ which are close to $\hat{z}$, in which case instead of spherical decomposition one may use a plane wave expansion. For temperature anisotropies we replace

$$
\sum_{lm} a_{T,lm}Y_{lm}(\hat{n}) \longrightarrow \int d^2l \; T(l)e^{i\mathbf{l}\cdot\mathbf{\theta}},
\tag{2.19}
$$

so that

$$
T(\hat{n}) = (2\pi)^{-2}\int d^2l \; T(l)e^{i\mathbf{l}\cdot\mathbf{\theta}}.
\tag{2.20}
$$

34

The Fourier coefficients satisfy,

$$\langle T(\boldsymbol{l})T(\boldsymbol{l}')\rangle = (2\pi)^2 \; C_{Tl} \; \delta^D(\boldsymbol{l} - \boldsymbol{l}'). \tag{2.21}$$

To expand $s = \pm 2$ weighted functions we use

$$\,_2Y_{lm} = \left[\frac{(l-2)!}{(l+2)!}\right]^{\frac{1}{2}} \eth^{\,2}Y_{lm} \quad \longrightarrow \quad (2\pi)^{-2}\frac{1}{l^2}\eth^{\,2}e^{i\boldsymbol{l}\cdot\boldsymbol{\theta}}$$

$$\,_{-2}Y_{lm} = \left[\frac{(l-2)!}{(l+2)!}\right]^{\frac{1}{2}} \bar\eth^{\,2}Y_{lm} \quad \longrightarrow \quad (2\pi)^{-2}\frac{1}{l^2}\bar\eth^{\,2}e^{i\boldsymbol{l}\cdot\boldsymbol{\theta}}. \tag{2.22}$$

They lead to the following expression

$$(Q + iU)(\hat{\boldsymbol{n}}) = -(2\pi)^2 \int d^2\boldsymbol{l} \; [E(\boldsymbol{l}) + iB(\boldsymbol{l})]\frac{1}{l^2}\eth^{\,2}e^{i\boldsymbol{l}\cdot\boldsymbol{\theta}}$$

$$(Q - iU)(\hat{\boldsymbol{n}}) = -(2\pi)^2 \int d^2\boldsymbol{l} \; [E(\boldsymbol{l}) - iB(\boldsymbol{l})]\frac{1}{l^2}\bar\eth^{\,2}e^{i\boldsymbol{l}\cdot\boldsymbol{\theta}}. \tag{2.23}$$

From equation (A.2) we obtain in the small scale limit

$$\frac{1}{l^2}\eth^{\,2}e^{i\boldsymbol{l}\cdot\boldsymbol{\theta}} = -e^{-2i(\phi-\phi_l)}e^{i\boldsymbol{l}\cdot\boldsymbol{\theta}}$$

$$\frac{1}{l^2}\bar\eth^{\,2}e^{i\boldsymbol{l}\cdot\boldsymbol{\theta}} = -e^{2i(\phi-\phi_l)}e^{i\boldsymbol{l}\cdot\boldsymbol{\theta}}$$

$$\tag{2.24}$$

where $(l_x + il_y) = le^{i\phi_l}$.

The above expression was derived in the spherical basis where $\hat{e}_1 = \hat{e}_\theta$ and $\hat{e}_2 = \hat{e}_\phi$, but in the small scale limit one can define a fixed basis in the sky perpendicular to $\hat{z}$, $\hat{e}'_1 = \hat{e}_x$ and $\hat{e}'_2 = \hat{e}_y$. The Stokes parameters in the two coordinate systems are related by

$$(Q + iU)' = e^{-2i\phi}(Q + iU)$$

$$(Q - iU)' = e^{2i\phi}(Q - iU). \tag{2.25}$$

Combining equations (2.23)-(2.25) we find

$$
\begin{aligned}
Q'(\boldsymbol{\theta}) &= (2\pi)^{-2} \int d^2 \boldsymbol{l} \ [E(\boldsymbol{l})\cos(2\phi_l) - B(\boldsymbol{l})\sin(2\phi_l)]e^{i\boldsymbol{l}\cdot\boldsymbol{\theta}} \\
U'(\boldsymbol{\theta}) &= (2\pi)^{-2} \int d^2 \boldsymbol{l} \ [E(\boldsymbol{l})\sin(2\phi_l) + B(\boldsymbol{l})\cos(2\phi_l)]e^{i\boldsymbol{l}\cdot\boldsymbol{\theta}}.
\end{aligned}
\tag{2.26}
$$

These relations agree with those given in [5], which were derived in the small scale approximation. As already shown there, power spectra and correlation functions for Q and U used in previous work on the subject [1, 2, 3, 4, 6] can be simply derived from these expressions.

In the small scale limit the correlation functions are (in their natural coordinate system denoted with an r in equation 2.18),

$$
\begin{aligned}
C_T(\theta) &= \int \frac{d^2 \boldsymbol{l}}{(2\pi)^2} \ e^{il\theta\cos\phi_l} \ C_{Tl} \\
C_Q(\theta) &= \int \frac{d^2 \boldsymbol{l}}{(2\pi)^2} \ e^{il\theta\cos\phi_l} \ [C_{El}\cos^2(2\phi_l) + C_{Bl}\sin^2(2\phi_l)] \\
C_U(\theta) &= \int \frac{d^2 \boldsymbol{l}}{(2\pi)^2} \ e^{il\theta\cos\phi_l} \ [C_{El}\sin^2(2\phi_l) + C_{Bl}\cos^2(2\phi_l)] \\
C_C(\theta) &= \int \frac{d^2 \boldsymbol{l}}{(2\pi)^2} \ e^{il\theta\cos\phi_l} \ C_{Cl}\cos(2\phi_l),
\end{aligned}
\tag{2.27}
$$

or equivalently,

$$
\begin{aligned}
C_T(\theta) &= \int \frac{ldl}{2\pi} \ C_{Tl} \ J_0(l\theta) \\
C_Q(\theta) + C_U(\theta) &= \int \frac{ldl}{2\pi} \ (C_{El} + C_{Bl}) \ J_0(l\theta) \\
C_Q(\theta) - C_U(\theta) &= \int \frac{ldl}{2\pi} \ (C_{El} - C_{Bl}) \ J_4(l\theta) \\
C_C(\theta) &= -\int \frac{ldl}{2\pi} \ C_{Cl} \ J_2(l\theta),
\end{aligned}
\tag{2.28}
$$

J_ν are cylindrical Bessel functions.

These relations can be inverted to obtain the power spectra in terms of the corre-

lations,

$$
\begin{aligned}
C_{Tl} &= 2\pi \int_0^\pi \theta d\theta \; C_T(\theta) \; J_0(l\theta) \\
C_{El} &= 2\pi \int_0^\pi \theta d\theta \; \{[C_Q(\theta) + C_U(\theta)] \; J_0(l\theta) + [C_Q(\theta) - C_U(\theta)] \; J_4(l\theta)\} \\
C_{Bl} &= 2\pi \int_0^\pi \theta d\theta \; \{[C_Q(\theta) + C_U(\theta)] \; J_0(l\theta) - [C_Q(\theta) - C_U(\theta)] \; J_4(l\theta)\} \\
C_{Cl} &= -2\pi \int_0^\pi \theta d\theta \; C_C(\theta) \; J_2(l\theta).
\end{aligned} \tag{2.29}
$$

2.1.3 Analysis of All-Sky Maps

In this section we discuss issues related to simulating and analyzing all-sky polarization and temperature maps. This should be specially useful for future satellite missions [9, 10], which will measure temperature anisotropies and polarization over the whole sky with high angular resolution. Such an all-sky analysis will be of particular importance if reionization and tensor fluctuations are important, in which case polarization will have useful information on large angular scales (Chapter 4), where Fourier analysis (i.e. division of the sky into locally flat patches) is not possible. In addition, it is important to know how to simulate an all-sky map which preserves proper correlations between neighboring patches of the sky and with which small scale analysis can be tested for possible biases.

To make an all-sky map we need to generate the multipole moments $a_{T,lm}$, $a_{E,lm}$ and $a_{B,lm}$. This can be done by a generalization of the method given in [5]. For each l one diagonalizes the correlation matrix $M_{11} = C_{Tl}$, $M_{22} = C_{El}$, $M_{12} = M_{21} = C_{Cl}$ and generates from a normalized gaussian distribution two pairs of random numbers (for real and imaginary components of $a_{l\pm m}$). Each pair is multiplied with the square root of eigenvalues of M and rotated back to the original frame. This gives a realization of $a_{T,l\pm m}$ and $a_{E,l\pm m}$ with correct cross-correlation properties. For $a_{B,l\pm m}$ the procedure is simpler, because it does not cross-correlate with either T or E, so a pair of gaussian random variables is multiplied with $C_{Bl}^{1/2}$ to make a realization of $a_{B,l\pm m}$.

Once $a_{E,lm}$ and $a_{B,lm}$ are generated we can form their linear combinations $a_{2,lm}$ and $a_{-2,lm}$. Finally, to make a map of $Q(\hat{n})$ and $U(\hat{n})$ in the sky we perform the

sum in equation (2.3). To reconstruct the polarization power spectrum from a map of $Q(\hat{n})$ and $U(\hat{n})$ one first combines them in $Q + iU$ and $Q - iU$ to obtain spin ± 2 quantities. Performing the integral over $_{\pm 2}Y_{lm}$ (equation 2.5) projects out $_{\pm 2s}a_{lm}$, from which $a_{E,lm}$ and $a_{B,lm}$ can be obtained. It is important to remember that in this treatment Q and U are defined using the spherical coordinate system.

Once we have the multipole moments we can construct various power spectrum estimators and analyze their variances. In the case of full sky coverage one may generalize the approach in [11] to estimate the variance in the power spectrum estimator in the presence of noise. We will assume that we are given a map of temperature and polarization with N_{pix} pixels and that the noise is uncorrelated from pixel to pixel and also between T, Q and U. The rms noise in the temperature is σ_T and that in Q and U is σ_P. If temperature and polarization are obtained from the same experiment by adding and subtracting the intensities between two orthogonal polarizations then the rms noise in temperature and polarization are related by $\sigma_T^2 = \sigma_P^2/2$.

Under these conditions and using the orthogonality of the $_sY_{lm}$ we obtain the statistical property of noise,

$$
\begin{aligned}
\langle (a_{T,lm}^{\text{noise}})^* a_{T,l'm'}^{\text{noise}} \rangle &= \frac{4\pi\sigma_T^2}{N_{pix}} \delta_{ll'}\delta_{mm'} \\
\langle (a_{2,lm}^{\text{noise}})^* a_{2,l'm'}^{\text{noise}} \rangle &= \frac{8\pi\sigma_P^2}{N_{pix}} \delta_{ll'}\delta_{mm'} \\
\langle (a_{-2,lm}^{\text{noise}})^* a_{-2,l'm'}^{\text{noise}} \rangle &= \frac{8\pi\sigma_P^2}{N_{pix}} \delta_{ll'}\delta_{mm'} \\
\langle (a_{-2,lm}^{\text{noise}})^* a_{2,l'm'}^{\text{noise}} \rangle &= 0.
\end{aligned}
\tag{2.30}
$$

By assumption there are no correlations between the noise in temperature and polarization. With these and equations (2.6) and (2.11) we find

$$
\begin{aligned}
\langle a_{T,lm}^* a_{T,l'm'} \rangle &= (C_{Tl}e^{-l^2\sigma_b^2} + w_T^{-1})\delta_{ll'}\delta_{mm'} \\
\langle a_{E,lm}^* a_{E,l'm'} \rangle &= (C_{El}e^{-l^2\sigma_b^2} + w_P^{-1})\delta_{ll'}\delta_{mm'} \\
\langle a_{B,lm}^* a_{B,l'm'} \rangle &= (C_{Bl}e^{-l^2\sigma_b^2} + w_P^{-1})\delta_{ll'}\delta_{mm'} \\
\langle a_{E,lm}^* a_{T,l'm'} \rangle &= C_{Cl}e^{-l^2\sigma_b^2}\delta_{ll'}\delta_{mm'}
\end{aligned}
$$

$$\langle a^*_{B,l'm'} a_{E,lm} \rangle = \langle a^*_{B,l'm'} a_{T,lm} \rangle = 0. \tag{2.31}$$

For simplicity we characterized the beam smearing by $e^{l^2 \sigma_b/2}$ where σ_b is the gaussian size of the beam and we defined $w^{-1}_{T,P} = 4\pi \sigma^2_{T,P}/N_{pix}$ [5, 11].

The estimator for the temperature power spectrum is [11],

$$\hat{C}_{Tl} = \left[\sum_m \frac{|a_{T,lm}|^2}{2l+1} - w^{-1}_T \right] e^{l^2 \sigma^2_b} \tag{2.32}$$

Similarly for polarization and cross correlation the optimal estimators are given by,

$$\hat{C}_{El} = \left[\sum_m \frac{|a_{E,lm}|^2}{2l+1} - w^{-1}_P \right] e^{l^2 \sigma^2_b}$$

$$\hat{C}_{Bl} = \left[\sum_m \frac{|a_{B,lm}|^2}{2l+1} - w^{-1}_P \right] e^{l^2 \sigma^2_b}$$

$$\hat{C}_{Cl} = \left[\sum_m \frac{(a^*_{E,lm} a_{T,lm} + a_{E,lm} a^*_{T,lm})}{2(2l+1)} \right] e^{l^2 \sigma^2_b}. \tag{2.33}$$

The covariance matrix between the different estimators, $\text{Cov}(XX') = \langle (\hat{X} - \langle \hat{X} \rangle)(\hat{X}' - \langle \hat{X}' \rangle) \rangle$ is easily calculated using equation (2.31). The diagonal terms are given by

$$\text{Cov}(\hat{C}^2_{Tl}) = \frac{2}{2l+1}(C_{Tl} + w^{-1}_T e^{l^2 \sigma^2_b})^2$$

$$\text{Cov}(\hat{C}^2_{El}) = \frac{2}{2l+1}(C_{El} + w^{-1}_P e^{l^2 \sigma^2_b})^2$$

$$\text{Cov}(\hat{C}^2_{Bl}) = \frac{2}{2l+1}(C_{Bl} + w^{-1}_P e^{l^2 \sigma^2_b})^2$$

$$\text{Cov}(\hat{C}^2_{Cl}) = \frac{1}{2l+1} \left[C^2_{Cl} + (C_{Tl} + w^{-1}_T e^{l^2 \sigma^2_b})(C_{El} + w^{-1}_P e^{l^2 \sigma^2_b}) \right]. \tag{2.34}$$

The non-zero off diagonal terms are

$$\text{Cov}(\hat{C}_{Tl}\hat{C}_{El}) = \frac{2}{2l+1} C^2_{Cl}$$

$$\text{Cov}(\hat{C}_{Tl}\hat{C}_{Cl}) = \frac{2}{2l+1} C_{Cl}(C_{Tl} + w^{-1}_T e^{l^2 \sigma^2_b})$$

$$\text{Cov}(\hat{C}_{El}\hat{C}_{Cl}) = \frac{2}{2l+1} C_{Cl}(C_{El} + w^{-1}_P e^{l^2 \sigma^2_b}). \tag{2.35}$$

Note that the theoretical analysis is significantly more complicated if all four power spectrum estimators are used to deduce the underlying cosmological model. For example, to test the sensitivity of the spectrum to the underlying parameters one uses the Fisher information matrix approach [12, 13]. If only temperature information is given then for each l a derivative of the temperature spectrum with respect to the parameter under investigation is computed and this information is then summed over all l weighted by $\mathrm{Cov}^{-1}(\hat{C}_{Tl}^2)$. In the more general case discussed here instead of a single derivative we have a vector of four derivatives and the weighting is given by the inverse of the covariance matrix,

$$\alpha_{ij} = \sum_l \sum_{X,Y} \frac{\partial C_{Xl}}{\partial s_i} \mathrm{Cov}^{-1}(C_{Xl}C_{Yl}) \frac{\partial C_{Yl}}{\partial s_j}, \tag{2.36}$$

where α_{ij} is the Fisher information or curvature matrix, Cov^{-1} is the inverse of the covariance matrix, s_i are the cosmological parameters one would like to estimate and X, Y stands for T, E, B, C. For each l one has to invert the covariance matrix and sum over X and Y, which makes the numerical evaluation of this expression significantly more involved.

2.2   Understanding E and B Polarization

In the previous sections we have discussed in detail the mathematical formalism needed to characterize the anisotropies in the CMB. In this subsection we want to take another look at the new polarization variables we introduced, E and B. By doing so we will develop further intuition as to what E and B physically mean. We will also study the power spectra and correlation functions for SCDM to point out the similarities and differences between the temperature and polarization anisotropies.

2.2.1   E and B in Real Space

The main characteristic of the polarization field is that it is a spin-2 field. The new variables E and B allow us to describe it more conveniently in terms of two spin zero

quantities. So far we have done this in Fourier space (more generally in l-space when not working in the small scale limit). In this section we want to explore E and B-type polarizations directly in real space. We will work in the small scale limit to make the notation simpler; the generalization to all sky modes is straightforward.

As in equation (2.20) we can define

$$\begin{aligned} E(\boldsymbol{\theta}) &= (2\pi)^{-2} \int d^2l\; e^{i\boldsymbol{l}\cdot\boldsymbol{\theta}}\; E(\boldsymbol{l}) \\ B(\boldsymbol{\theta}) &= (2\pi)^{-2} \int d^2l\; e^{i\boldsymbol{l}\cdot\boldsymbol{\theta}}\; B(\boldsymbol{l}). \end{aligned} \tag{2.37}$$

These two quantities describe completely the polarization field. Figure 2-2 shows the E polarization field and the polarization vectors for the same simulation shown in Figure 2-1. There is only E-type polarization associated with SCDM because this is the only pattern that is produced by density perturbations and we did not include a stochastic background of gravity waves. We will discuss this point further in the next section and in Chapter 4.

In Figure 2-2 we can see that hot spots of the E map correspond to points with tangential polarization patterns (negative Q_r). We find radial polarization patterns around the cold spots of E. The polarization pattern in our simulation did not have any B-type polarization so to get a better intuition as to what B-type polarization means we can take the same E field in Figure 2-2 and pretend that it was actually B-type polarization. The polarization vectors are shown in Figure 2-3, they correspond to the ones in Figure 2-2 rotated by $45°$. Hot and cold spots of the B field correspond to places where the polarization vectors circulate around in opposite directions. It is clear from this Figure that the polarization pattern is not invariant under reflections. The distinction between E and B-type of polarization is not in the size or orientation of the polarization vector at a given point but in the relative orientations of the vectors, namely the pattern.

We can stress the characteristics of E and B-type of polarization by looking at Figure 2-4 which summarize what we found in the simulated maps. Places on the sky where the polarization pattern is tangential correspond to hot spots of E while a

41

radial pattern will produce a cold spot. The patterns that give rise to B are different in nature; while the radial and tangential patterns are symmetric under reflections those that create B are not. One pattern transforms into the other under a parity transformation. This is precisely what we mean when we say B is a pseudoscalar, if the pattern of polarization vectors on the sky was such that we had a hot spot of B when we looked at the mirror image of that pattern we would have a cold spot of B.

We can use Figure 2-4 to argue why density perturbations cannot create B-type polarization while gravity waves can, although the detailed mathematical proof is left for Chapter 3. We can consider only one Fourier mode of density perturbations because an arbitrary density field can always be expanded in Fourier modes. In the linear regime the total B generated by all the modes will be the sum of the contributions by each mode. We will prove the total B-type polarization is zero because the B polarization generated every mode is zero.

Figure 2-5 illustrates our point. In the upper half we consider the perturbations induced by a single density mode. The problem has two important symmetries, symmetry under rotation around $\hat{k}$ and symmetry under a reflection about any plane containing $\hat{k}$. It is clear that these two symmetries do not allow for a non zero U in the coordinate system shown in the figure. The polarization vectors must be either along $\hat{e}_\theta$ or $\hat{e}_\phi$. The two possible orientations of the polarization consistent with the symmetries are shown in the upper right hand side. This can be shown to imply that B-type polarization is zero. We first focus on the particular case when the direction of observation coincides $\hat{k}$ because it is easier to visualize. We can use Figure 2-4 with to recognize the polarization patterns that are allowed around $\hat{k}$. The two B-type polarization patterns cannot be produced because they are not invariant under parity. We leave the generalization of the argument to directions of observation different than $\hat{k}$ for later, when we introduce a way of calculating E and B directly in real space.
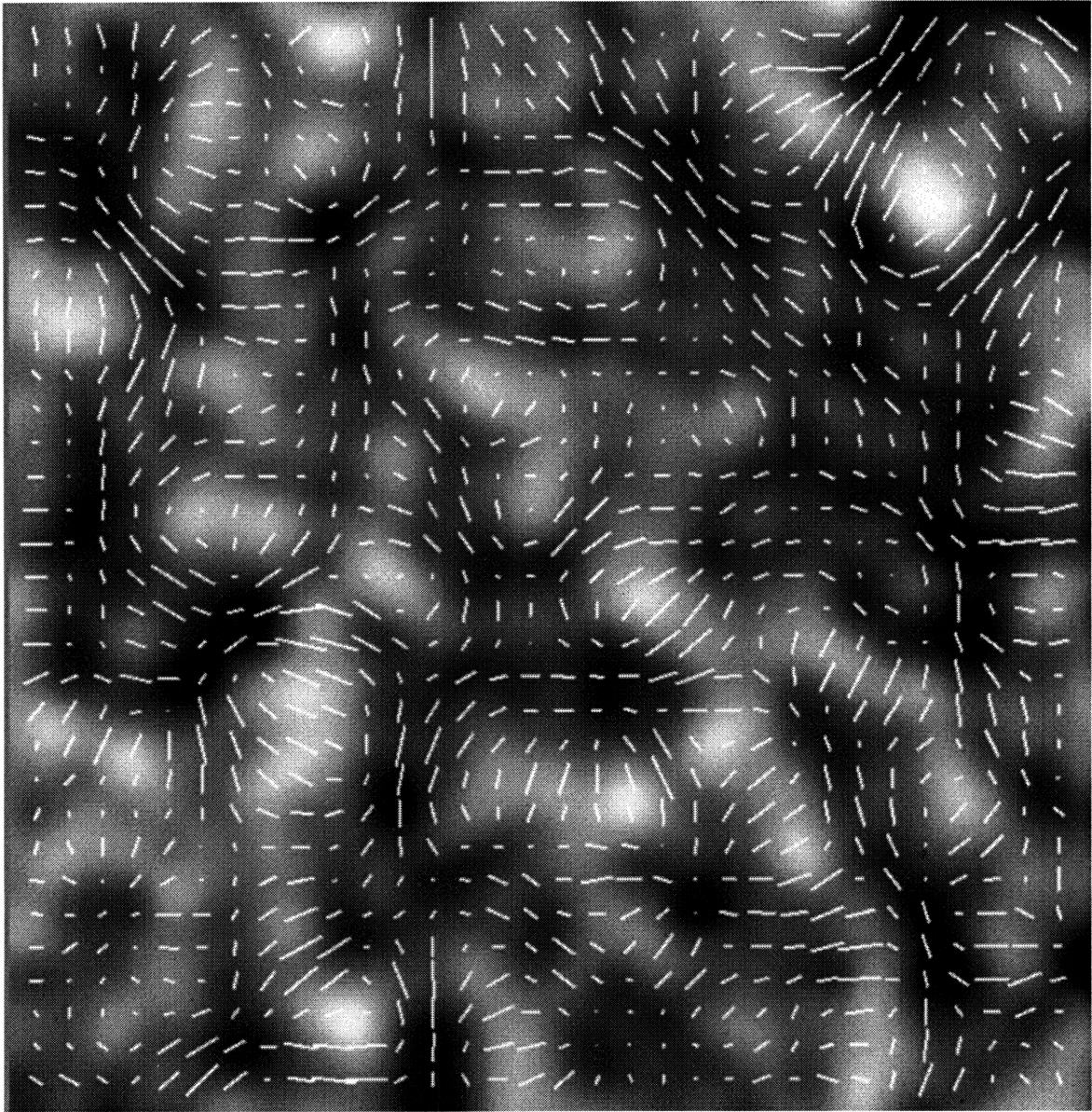
Figure 2-2: Simulated polarization map for SCDM($2.5^\circ \times 2.5^\circ$ field). The polarization vectors are shown together with the E-type polarization. The E field varies between $-140\mu K < E < 158\mu K$, the largest polarization vector has an amplitude $P = 128\mu K$.

Gravitational waves do not possess either rotational or reflection symmetry. We illustrate this in Figure 2-5 using the deformation of a ring of test particles in the $\hat{x} - \hat{y}$ plane when a gravitational wave traveling along the $\hat{z}$ passes by. The influence of a gravitational wave does not have the symmetry under reflections that made zero the B-type polarization for density perturbations and will thus produce some B.

We can combine equation (2.37) with the definition of $E(l)$ and $B(l)$ in terms of Q and U,

$$
\begin{aligned}
E(l) &= \int d^2\theta \; [Q(\theta)\cos(2\phi_l) + U(\theta)\sin(2\phi_l)] \; e^{-il\cdot\theta} \\
B(l) &= \int d^2\theta \; [U(\theta)\cos(2\phi_l) - Q(\theta)\sin(2\phi_l)] \; e^{-il\cdot\theta},
\end{aligned} \qquad (2.38)
$$

to obtain an expression relating E and B in real space directly to Q and U,

$$
\begin{aligned}
E(\theta) &= -\int d^2\theta' \; \omega(\tilde{\theta}) \; [Q(\theta')\cos(2\tilde{\phi}) - U(\theta')\sin(2\tilde{\phi})] \\
&= -\int d^2\theta' \; \omega(\tilde{\theta}) \; Q_r(\theta') \\
B(\theta) &= -\int d^2\theta' \; \omega(\tilde{\theta}) \; [U(\theta')\cos(2\tilde{\phi}) + Q(\theta')\sin(2\tilde{\phi})] \\
&= -\int d^2\theta' \; \omega(\tilde{\theta}) \; U_r(\theta').
\end{aligned} \qquad (2.39)
$$

The variables $(\tilde{\theta}, \tilde{\phi})$ are the polar coordinates of the vector $\theta - \theta'$. In equation (2.39) Q_r and U_r are the Stokes parameters in the polar coordinate system centered at θ. For example if θ is zero, $Q_r = \cos 2\phi' \; Q(\theta') - \sin 2\phi' \; U(\theta')$ and $U_r = \cos 2\phi' \; U(\theta') + \sin 2\phi' \; Q(\theta')$. The window can be shown to be $\omega(\theta) = 1/\pi\theta^2$ $(\theta \neq 0)$, $\omega(\theta) = 0$ $(\theta = 0)$. We can read directly from equation (2.39) the relations between the pattern of polarization and the sign of E and B, for example a tangential pattern of polarization which has negative Q_r will produce positive E (hot spot of E).

From equation (2.39) we can understand how we achieve two rotationally invariant quantities out of the spin 2 field: to get $E(\theta)$ and $B(\theta)$ we average the values of Q_r and U_r respectively, over circles centered at θ. Each circle is weighted by $\omega(\tilde{\theta})$. By construction these two quantities are rotationally invariant: the Stokes parameters Q_r and U_r do not depend on the coordinate system, they are defined relative to the

$\theta - \theta'$ vector and the weight function ω is also rotationally invariant. We are giving the same weight to all the points in each circle and we are using the Stokes parameters defined in their natural coordinate system. The variable B is clearly a pseudoscalar because it is the average of U_r and U_r changes sign under parity.

We can use Equation (2.39) to prove that B-type polarization is zero in any direction for a single density mode. We had argued that this was the case when the direction of observation and $\hat{k}$ where the same. In general the two directions form an angle and $\hat{k}$ will intersect the plane perpendicular to $\hat{n}$ at a point different from $\hat{n}$. We illustrate this in Figure 2-5 where we considered the case in which the polarization vectors are radial around $\hat{k}$, but the argument is the same if they were tangential (the only allowed patterns at a given distance away from $\hat{k}$). To compute B we integrate U_r along circles centered at $\hat{n}$, but the polarization pattern has reflection symmetry across the line connecting $\hat{k}$ and $\hat{n}$ which implies that on opposite sides of the circle U_r has different signs and the integral cancels.

There is nothing special about the weight $\omega(\theta)$ as far as constructing a scalar and a pseudo-scalar, but this choice of weight has several important properties. It makes the correlation functions of E and B the closest to that of Q and U. For example with this choice $C_Q(\theta) + C_U(\theta) = C_E(\theta) + C_B(\theta)$. Another property is that this choice of weight preserves the nature of white noise. White noise in Q and U becomes white noise in E and B. On the other hand this choice of window requires integration over all θ and is non-local.
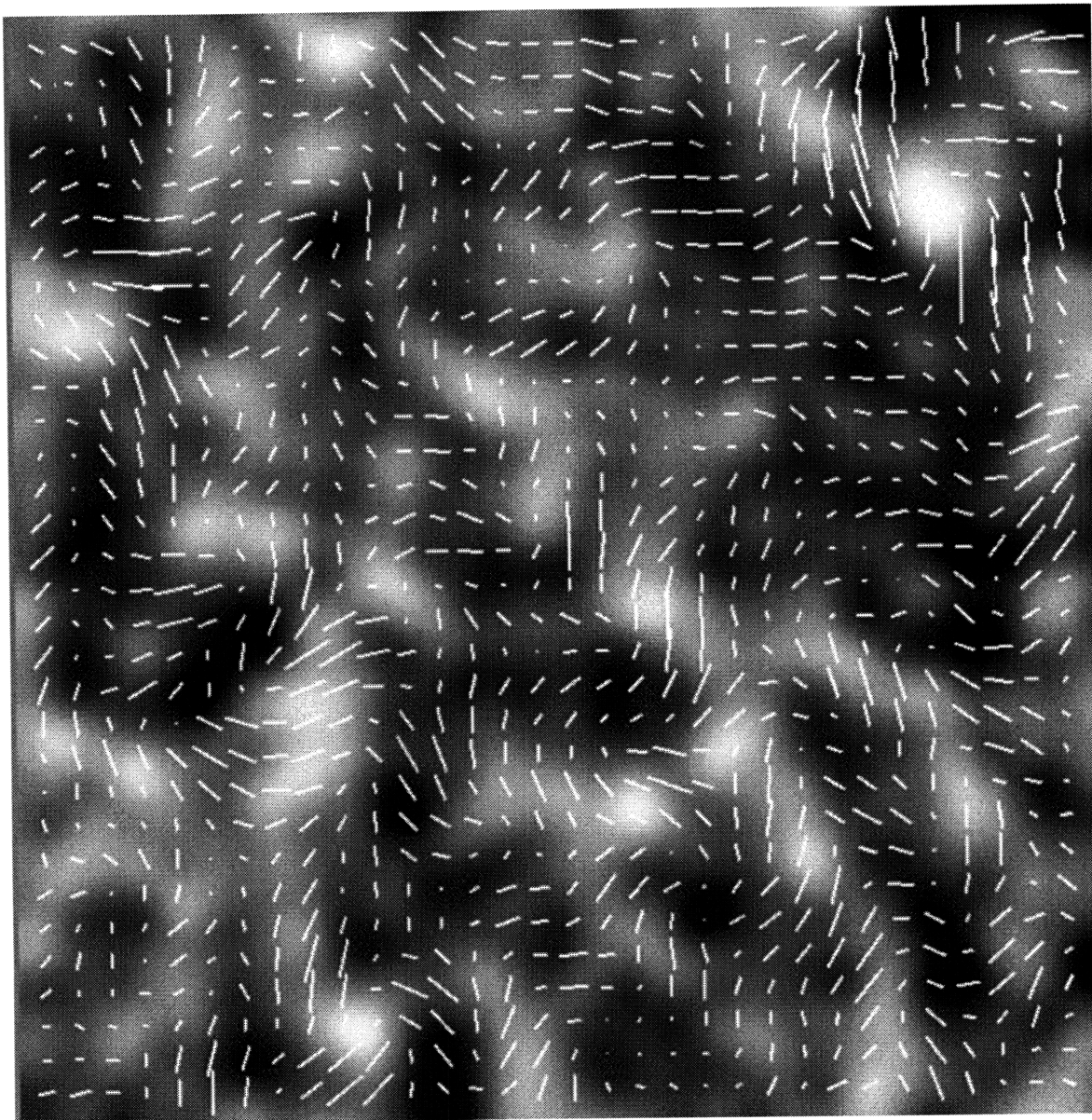
Figure 2-3: Simulated polarization map for SCDM($2.5°\times2.5°$ field) where the E-type polarization has been changed into B-type. The polarization vectors of the this figure are rotated $45°$ respect to the ones in previous ones.

Another expression for $E(\boldsymbol{\theta})$ and $B(\boldsymbol{\theta})$ can be obtained in terms of derivatives,

$$
\begin{aligned}
E(\boldsymbol{\theta}) &= \nabla^{-2}(\partial_x^2 - \partial_y^2)\, Q(\boldsymbol{\theta}) + \nabla^{-2}(2\partial_x\partial_y)\, U(\boldsymbol{\theta}) \\
B(\boldsymbol{\theta}) &= \nabla^{-2}(\partial_x^2 - \partial_y^2)\, U(\boldsymbol{\theta}) - \nabla^{-2}(2\partial_x\partial_y)\, Q(\boldsymbol{\theta}).
\end{aligned}
\tag{2.40}
$$

This equation makes the point that the extra l factors that would be introduced in the power spectra by the derivatives are compensated by the inverse Laplacian. This is what we mean when we say that the spectrum of E and B are the closest to that of Q and U. The inverse Laplacian is responsible for the non-local nature of $E(\boldsymbol{\theta})$ and $B(\boldsymbol{\theta})$ evident also in equation (2.39).

2.2.2 Analogy with Weak Lensing

There is a very close analogy between the E and B formalism we are using to describe CMB polarization and the mathematical framework used to study weak lensing. As photons travel across the universe their trajectories are deflected. As a result the observed intensity is related to the true one by $I_{obs}(\boldsymbol{\theta}) = I_{true}(\boldsymbol{\theta} + \delta\boldsymbol{\theta})$. This mapping will induce ellipticities in the images of the observed galaxies. The deformation tensor Φ_{ij} ($i,j = x,y$ in the small scale limit) can be calculated in terms of a projected gravitational potential ϕ_{proj}[5],

$$
\Phi_{ij} = \partial_i \partial_j \phi_{proj}.
\tag{2.41}
$$

The deformation tensor is usually decomposed into trace κ and the two components of the shear γ_1 and γ_2, $\Phi_{xx} = -\kappa - \gamma_1$, $\Phi_{yy} = -\kappa + \gamma_1$, $\Phi_{xy} = \Phi_{yx} = -\gamma_2$. The trace κ is also the dimensionless projected mass density. The shear part of the tensor can be obtained from the observed ellipticities of the galaxies [19].

The two quantities $\gamma_{(1,2)}$ are the analogues of (Q,U) for the CMB polarization field. They also form spin two variables $\gamma_1 \pm i\gamma_2$. Equations (2.40) and (2.41) can be used to show that the E variable in this case is nothing but the dimensionless

---

[5]The interested reader may find detailed expressions for the projected potential and other quantities in [14].

Q > 0   U = 0

Q < 0   U = 0

E < 0

E > 0

Q = 0   U < 0

Q = 0   U > 0

B < 0

B > 0
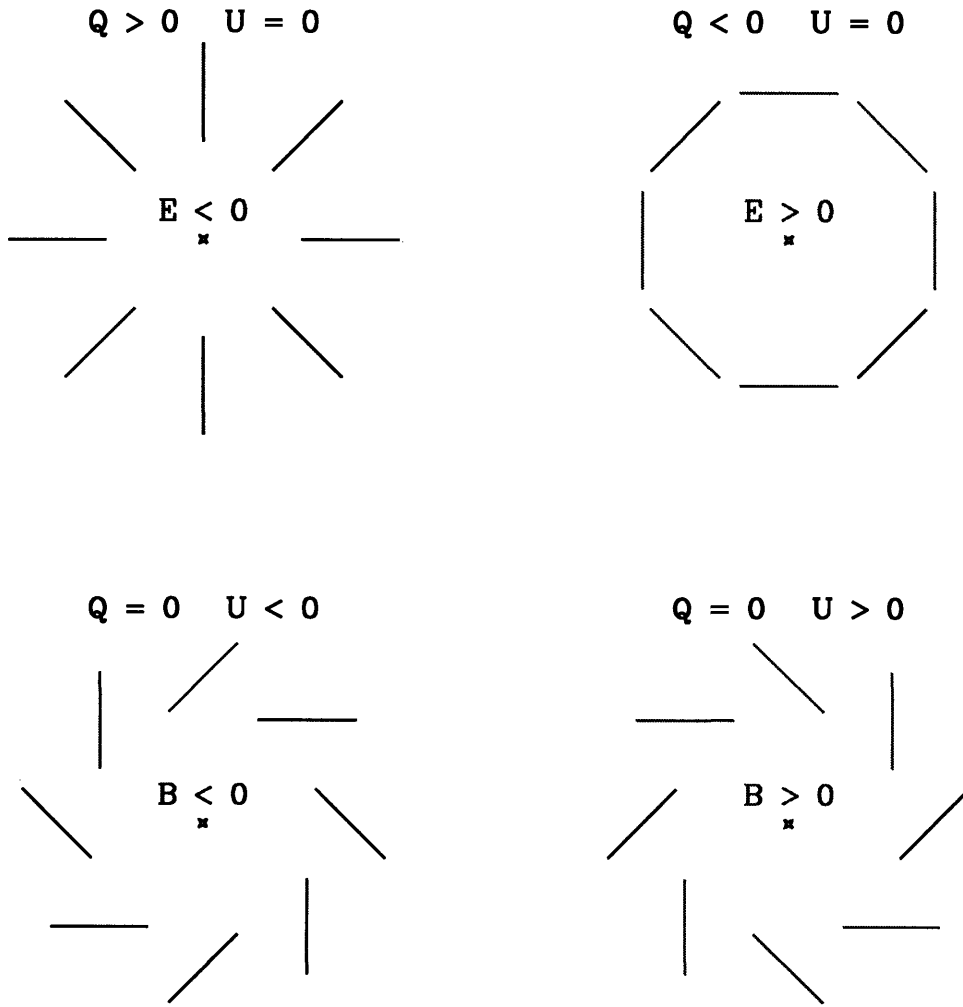
Figure 2-4: Polarization patterns that lead to positive and negative values of the E and B polarization fields. The Stokes parameters are measured in the polar coordinate system centered at the cross. All four patterns are invariant under rotation but the two patterns that generate B are not invariant under reflections.

50

Density Modes

ROTATION + PARITY
IMPLY U=0
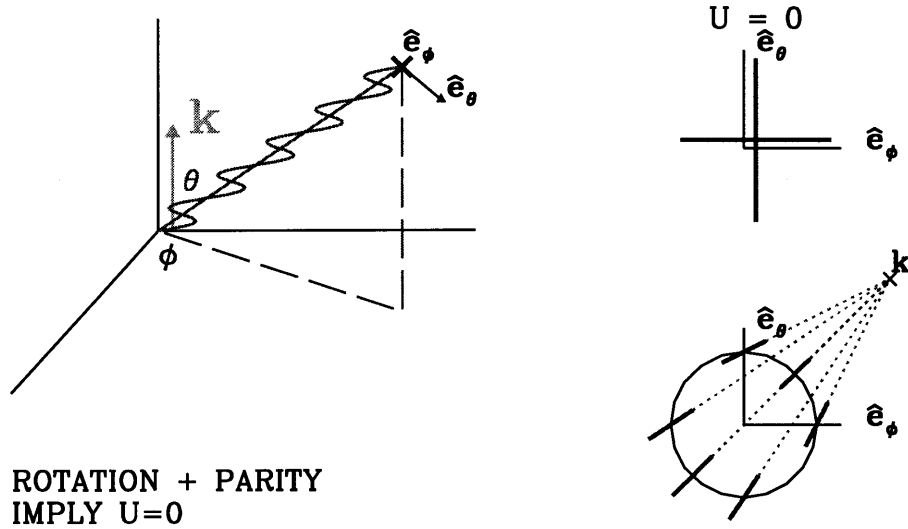
Gravitational Waves
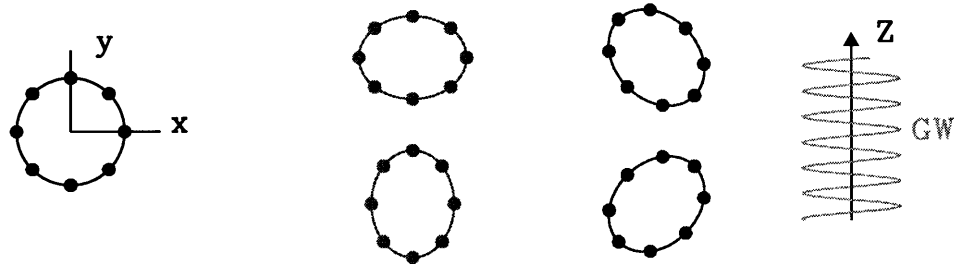
Figure 2-5: Upper half: A single mode of density perturbations has symmetries under rotation around the $\hat{k}$ axis and reflection about any plane containing it. Only I and Q Stokes parameters can be present in this reference frame and thus no B polarization is created. The integral along a circle of U_r, used to calculate B directly in real space, is zero because the pattern of polarization is symmetric under reflections across the line containing $\hat{k}$ and $\hat{n}$. Gravitational waves do not have these symmetries as illustrated by the deformation suffered by a ring of test particles as wave traveling along $\hat{z}$ passes by.

projected mass density κ,

$$E^{WL}(\boldsymbol{\theta}) = \nabla^{-2}(\partial_x^2 - \partial_y^2)\,\gamma_1(\boldsymbol{\theta}) + \nabla^{-2}(2\partial_{xy})\,\gamma_2(\boldsymbol{\theta}) = \nabla^2 \phi_{proj}(\boldsymbol{\theta}) = \kappa(\boldsymbol{\theta}) \qquad (2.42)$$

Thus in the case of weak lensing E has an important physical interpretation it is the projected mass density. This is clear in Figure 2-2: hot spots of the E field are the analog of high mass concentrations, so we see in the polarization vectors the typical orientation of the shear that we see in the deformation of galaxies around clusters. The analogous calculation of B for weak lensing is identically zero, as it is the $\hat{z}$ component of the curl of the gradient of the projected potential.

2.3   Correlators for SCDM

In this section we present the correlators for COBE normalized SCDM to point out some of the properties of CMB anisotropies and to understand their physical origin. Hydrogen recombination plays a crucial role in the generation of CMB anisotropies. As the universe expands it cools and around 3×10^5 years after the big bang hydrogen atoms are able to recombine to form neutral hydrogen and the universe becames transparent to the CMB photons. Recombination occurs very quickly. Before recombination photons and electrons scatter very efficiently forming a single fluid, while after recombination the photons are free to travel to the observer. The photons we detect coming from a particular direction come from a very small region of our universe (of size $\sim 50\ h^{-1}$ Mpc) at a distance $D \sim 6000\ h^{-1}$ Mpc away from us. The collection of all this regions in the universe is called the last scattering surface.

In order to understand the main features in Figure 2-1 one can work in the thin scattering surface approximation, where one assumes recombination occurs instantaneously. In this approximation the final temperature fractional anisotropy in direction $\hat{n}$ on the sky is

$$T(\hat{n}) = \frac{\delta_R}{4}\Big|_{\tau_*} - \hat{n} \cdot \mathbf{v_R}\big|_{\tau_*} - \frac{1}{2}\int_{\tau_*}^{\tau_0} d\tau\, \dot{h}_{ij}\hat{n}^i\hat{n}^j, \qquad (2.43)$$
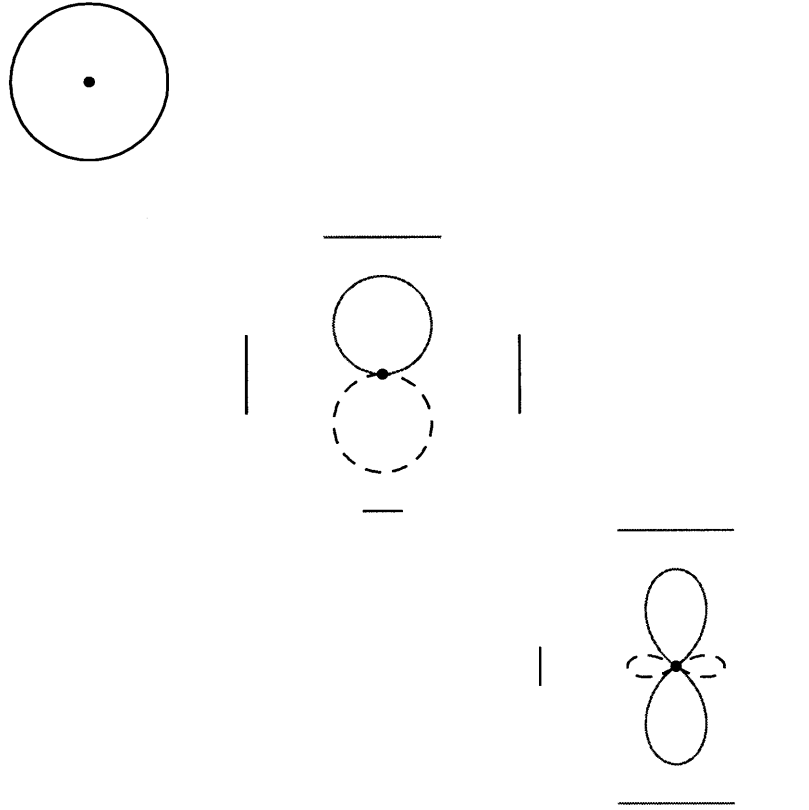
Figure 2-6: Intensity patterns incident on an electron and the resulting polarization of the scattered light in the direction perpendicular to the page. The dashed line indicates a smaller intensity while the full lines represent an excess in the number of photons. A uniform intensity field or a dipole pattern will produce no polarization. The rods around each diagram represent the direction of the polarization of the scattered light which come from that particular direction before the scattering. The total scattered light can be obtained by "adding" the four rods whose length is proportional to the amount of photons incident on the electron from each direction. Only the quadrupolar pattern will induce some polarization, because the summed lengths of the top and bottom rods differs from that of the left and right rods.

δ_R and $\mathbf{v_R}$ stand for the relative density perturbation and velocity of the photon-baryon plasma while h_{ij} describes the perturbation in the metric. Conformal time is denoted with τ; τ_0 and τ_* correspond to the times today and at recombination, respectively. The first two terms are evaluated at the last scattering surface and the third term is an integral along the line of sight. The anisotropies have three distinct origins: an overdensity of the photon baryon fluid somewhere on the last scattering translates into an increase in the measured temperature when we observe in that particular direction (first term). Furthermore, if the fluid is moving there will be an additional Doppler shift contribution (second term). Finally, gravitational redshift will change the photon temperature as photons travel toward us (third term). Note that this effect can take place anywhere along the path.

In order to generate polarization we need Thomson scattering between photons and electrons, which means that polarization cannot be generated after recombination (if there is no reionization). But Thomson scattering is not enough, the radiation incident on the electrons must also be anisotropic. Figure 2-6 illustrates this point. If the radiation incident on the electron is isotropic, by symmetry there can be no net polarization after the scattering. We consider a dipole anisotropy next: in the figure we illustrate the case where the intensity of the incident radiation is higher from the top and lower from the bottom, with the average intensity incident from the sides. The scattered radiation from photons incident from either the bottom or top will be polarized in the horizontal direction, while that coming from the sides will vertically polarized. The total degree of polarization is obtained by looking at all the scattered light, which in this case is unpolarized because the excess of radiation coming from above (relative to the sides) is compensated by the smaller amount coming from the bottom. Since a dipole pattern of anisotropies will not create any polarization, we need a quadrupolar pattern of intensity: an excess in photons must come from both top and bottom.

In the context of CMB, velocity gradients in the photon-baryon fluid will create the quadrupole that generates polarization. The photons that are scattered from a given electron come from places where the fluid has velocity $\mathbf{v}$. Because of the tight

coupling between photons and electrons the photon distribution function has a dipole term $T_1 = \hat{\mathbf{n}} \cdot \mathbf{v}$. Furthermore, gradients in the velocity field across the mean free path of the photons (λ_p) create a quadrupole $T_2 = \lambda_p n^i n^j \partial_i v_{Rj}$ in the photon distribution as seen in the rest frame of the electron. The velocity of the fluid will only create a dipole; one needs at least a velocity gradient to create a quadrupole.

The scattered radiation field is given by $(Q+iU) = -3/4\sigma_T \int d\Omega'/4\pi (\mathbf{m} \cdot \hat{\mathbf{n}}') T_2(\hat{\mathbf{n}}') \propto \lambda_p m^i m^j \partial_i v_j|_{\tau_*}$, where σ_T is the Thomson scattering cross section and we have written the scattering matrix as $P(\mathbf{m}, \hat{\mathbf{n}}') = -3/4\sigma_T |\mathbf{m} \cdot \hat{\mathbf{n}}'|^2$ with $\mathbf{m} = \hat{\mathbf{e}}_1 + i\hat{\mathbf{e}}_2$. In the last step we integrated over all directions of the incident photons $\hat{\mathbf{n}}'$. As photons decouple from the baryons their mean free path grows very rapidly, so a more careful analysis is needed to obtain the final polarization[6][15],

$$(Q + iU)(\hat{\mathbf{n}}) \approx 0.17\Delta\tau_* \mathbf{m}^i \mathbf{m}^j \partial_i v_j|_{\tau_*} \qquad (2.44)$$

where $\Delta\tau_*$ is the width of the last scattering surface and is giving a measure of the distance photons travel between their last two scatterings. The appearance of $m^i m^j$ in equation (2.44) assures that $(Q + iU)$ transforms correctly under rotations of $(\hat{\mathbf{e}}_1, \hat{\mathbf{e}}_2)$.

We can combine equations (2.40) and (2.44) to understand why B-type polarization is zero for anisotropies produced by density perturbations. We take $\hat{\mathbf{n}} = \hat{\mathbf{z}}$ and $\mathbf{m} = \hat{\mathbf{x}} + i\hat{\mathbf{y}}$. We then have $\nabla^2 B \propto (\partial_y^2 - \partial_x^2)U + 2\partial_x\partial_y Q$ which gives $\nabla^2 B \propto \nabla^2(\hat{\mathbf{z}} \cdot \nabla \times \mathbf{v})$ and is zero because the velocity field produced by density perturbations is irrotational, $\mathbf{v} = \nabla\psi$ and $\nabla \times \nabla\psi = 0$. On the other hand $\nabla^2 E \propto \nabla^2(\partial_x v_x + \partial_y v_y)$.

Before recombination Thomson scattering keeps the photons and baryons tightly coupled. They form a fluid with pressure provided by the photons and inertia by the baryons. This fluid supports the analog of acoustic oscillations where both the density and velocity are oscillating functions of time [17, 18]. The density is proportional to $\cos(c_s k\tau)$ while the velocity to $\sin(c_s k\tau)$, c_s is the sound speed. After hydrogen recombines the photons are free to travel to the observer without further scatterings.

We illustrate the important ingredients in the generation of the anisotropies with

---

[6]The velocity in this equation is in the conformal gauge.
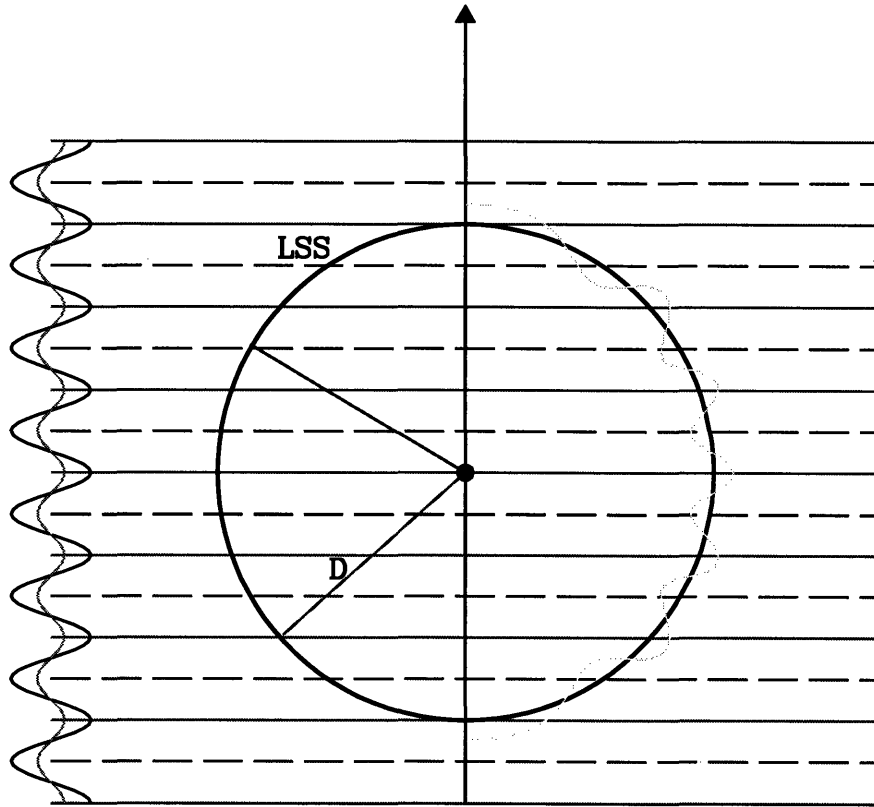
$$\Delta_T(\mathbf{k},\tau) \cos(\mathbf{kx})$$

Before Decoupling

$$\Delta_T(\mathbf{k},\tau) \sim \cos(\mathbf{k}\tau)$$

Figure 2-7: Two dimensional universe analogy. A particular density mode is oscillating in time before decoupling. At decoupling the photons are free to escape and have traveled a distance D to reach the observer (at the center of the circle). Although the density field has continued to evolve after recombination, the photons carry the information of the state of the plasma at the time the last scattered. We would see a pattern of hot and cold regions in this one dimensional sky because photons arriving from different directions come from places with varying photon energy density. This pattern is shown as a dotted line on the right side of the circle.

a two dimensional analogy in Figure 2-7. We show only one density mode which is oscillating as a function of time before recombination. Suddenly the hydrogen recombines when this mode was in a particular phase in the oscillation. The photons travel freely a distance D to the observer who sees more photons coming from the what were denser regions at recombination. The pattern of hot and cold temperature produced by this mode is not a perfect sinusoid because we are intersecting a plane wave with a circle, but it has a typical period. The contribution peaks at $l \sim kD$.

In Figure 2-8 we show the three power spectra needed to characterize the CMB anisotropies. The oscillations in the CMB spectra can be analytically understood within this picture. Waves of different wavenumber k are at different phases in their oscillations at this particular time, which translates into an oscillating amplitude for the modes as a function of k. Physical size and angle in the sky are related by the angular diameter distance to recombination, so the oscillating amplitude of the modes also produces acoustic peaks in l space. On small scales ($l \geq 1000$), when the wavelength of the perturbation becomes comparable to the mean free path of the photons prior to recombination, the anisotropies are suppressed by photon diffusion. Photons can diffuse out of density peaks, thereby erasing the anisotropies.

The curves in Figure 2-8 illustrate the differences between temperature and polarization anisotropies. The large angular scale polarization is greatly suppressed. Correlations over large angles can only be created by the long wavelength perturbations, but these cannot produce a large polarization signal because of the tight coupling between photons and electron prior to recombination. Multiple scatterings make the plasma very homogeneous; only wavelengths that are small enough to produce anisotropies over the mean free path of the photons will give rise to a significant quadrupole in the temperature distribution, and thus to polarization.

On subdegree angular scales temperature anisotropy, polarization and their cross correlation show acoustic oscillations (Figure 2-8), but in the polarization and cross correlation spectra the peaks are much sharper. The polarization is produced by velocity gradients of the photon-baryon fluid at the last scattering surface (equation 2.44). The temperature receives contributions from density and velocity perturbations
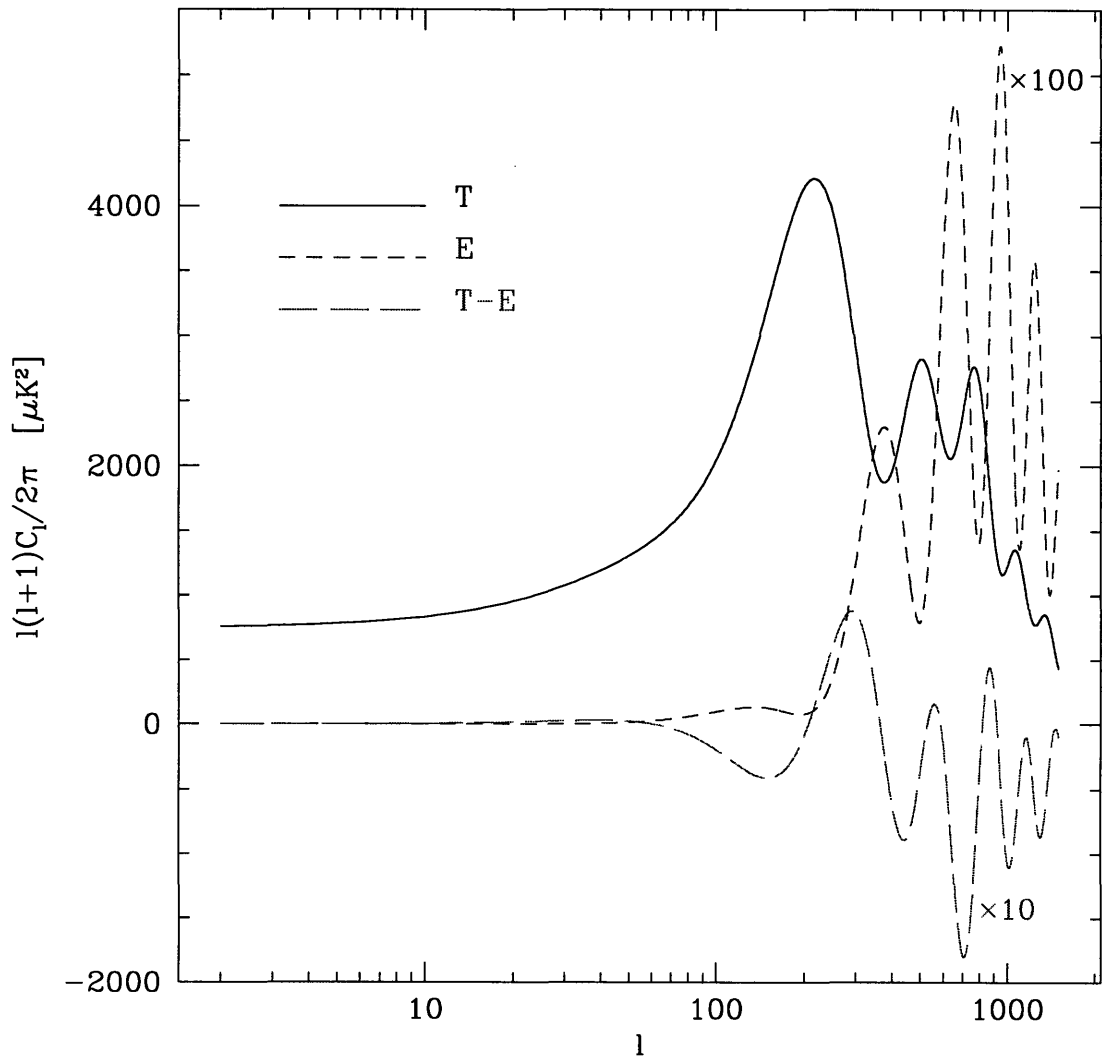
Figure 2-8: Power spectra for COBE normalized SCDM. The E and the $T-E$ spectra have been rescaled for convenience.

and these partially cancel each other making the features in the temperature spectrum less sharp. The dominant contribution to the temperature comes from the oscillations in the density, which are out of phase with the velocity. This explains the difference in location between temperature and polarization peaks. The extra gradient in the polarization signal, equation (2.44), explains why its overall amplitude peaks at a smaller angular scale. The fact that the polarization field has relatively more small scale power is evident when we compare the the T and E fields in Figures 2-1 and 2-2.

Figure 2-9 show the correlation functions in real space. The spectrum has been smoothed with a $\theta_{fwhm} = 0.2^{\circ}$ gaussian, similar to the MAP beam. An interesting point is that both polarization auto-correlation functions are negative for some range of angles, which does not happen for the temperature. To interpret the cross correlation we can consider the polarization pattern around a hot spot ($T > 0$). The cross correlation starts positive, implying a radial pattern of polarization. Not all the polarization is correlated with the temperature so it is hard to see this trend in Figure 2-1. In Figure 2-10 we only plot the correlated part of the polarization, here it is clear that the vectors are preferentially radial around hot spots.

As we move out to larger angles the cross correlation changes sign. When it is negative the pattern becomes tangential. For large separations the polarization around a hot (cold) spot is tangential (radial). A point worth noting is that the cross correlation goes to zero as θ goes to zero, in contrast to what happens for the other correlation functions. Symmetry arguments dictate that the Q Stokes parameter at a given point cannot be correlated with the temperature at that same point. What sign would this correlation have? Equivalently, in what direction would the polarization be? Only when we consider two points separated by some distance is the symmetry broken. The vector joining the two points becomes the privileged direction and the polarization can be preferentially parallel or perpendicular to this direction.
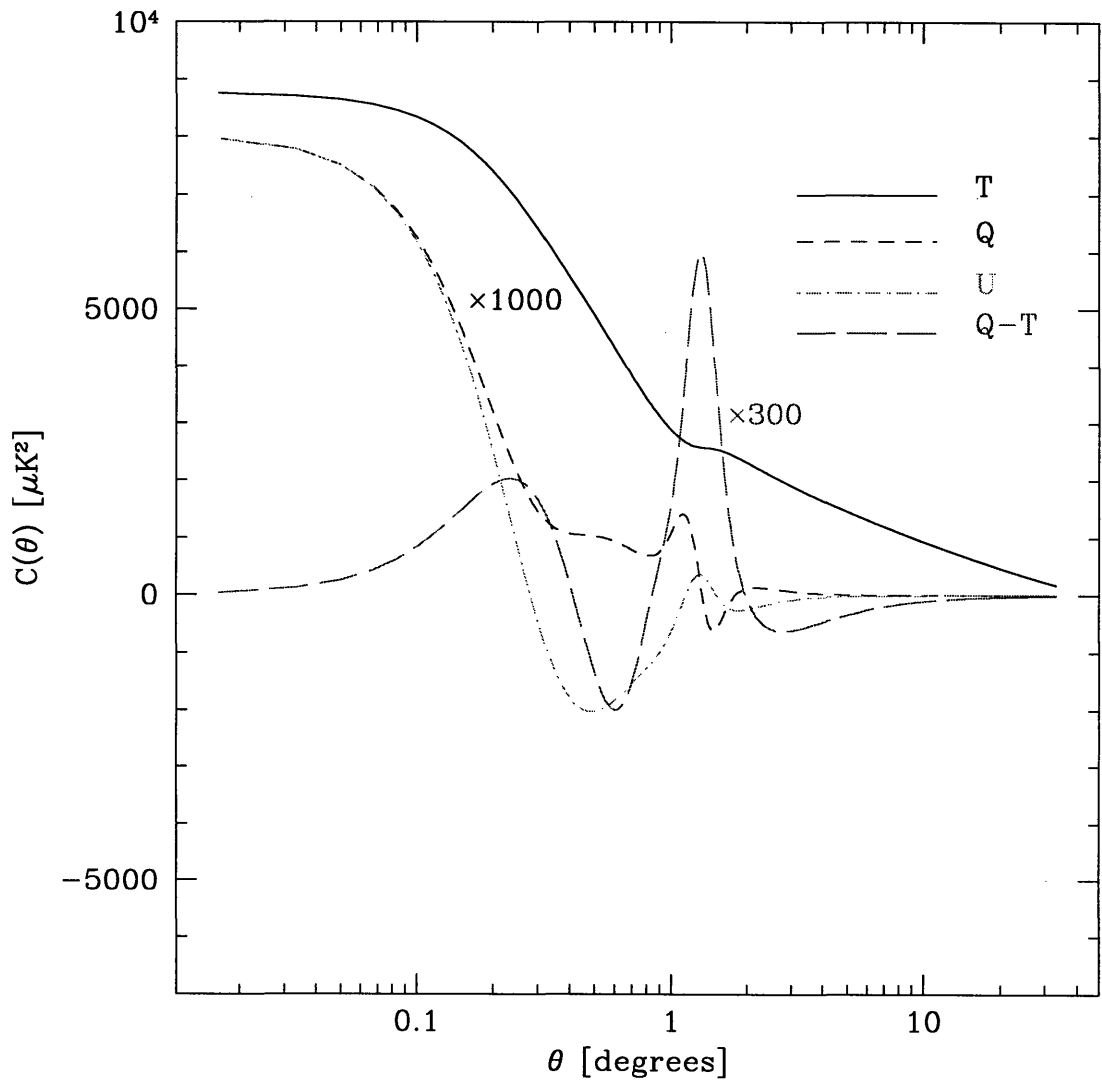
Figure 2-9: Correlation functions in real space for COBE normalized SCDM model. The spectra have been smoothed with a $\theta_{fwhm} = 0.2°$ corresponding to the beam size of MAP.

Bibliography

[1] R. Crittenden, R. L. Davis & P. J. Steinhardt, Astrophys. J. Lett. **417**, L13 (1993).

[2] R. A. Frewin, A. G. Polnarev & P. Coles, Mon. Not. R. Astron. Soc. **266**, L21 (1994).

[3] D. Coulson, R. G. Crittenden & N. Turok, Phys. Rev. Lett. **73**, 2390 (1994).

[4] D. Coulson & N. G. Turok, Phys. Rev. D **52**, 5402 (1995).

[5] U. Seljak, Astrophys. J., **482**, 6 (1996).

[6] A. Kosowsky, Ann. Phys. **246**, 49 (1996).

[7] E. Newman & R. Penrose, J. Math. Phys. **7**,863 (1966).

[8] M. Kamionkowski, A. Kosowsky & A. Stebbins, Phys. Rev. D **55** 7368 (1997).

[9] See the MAP homepage at http://map.gsfc.nasa.gov.

[10] Visit http://astro.estec.esa.nl/SA-general/Projects/Planck/ for information on Planck.

[11] L. Knox, Phys. Rev. D. **52**, 4307 (1995).

[12] G. Jungman, M. Kamionkowski, A. Kosowsky, & D. N. Spergel, Phys. Rev. Lett. **76**, 1007 (1996); Phys. Rev. D **54** 1332 (1996).

[13] M. Zaldarriaga, D. N. Spergel & U. Seljak, Asptrophys. J. **488**, 1, (1997).

[14] U. Seljak, preprint astro-ph/9711124 (1997).

[15] M. Zaldarriaga & D. Harari, Phys. Rev D **52**, 3276 (1995).

[16] M. Zaldarriaga & U. Seljak, Phys. Rev. D **55**, 1830 (1997).

[17] U. Seljak, Astrophys. J. **435**, L87 (1994).

[18] W. Hu & N. Sugiyama, Phys. Rev D **51**, 2599 (1995).

[19] N. Kaiser & G. Squires, Astophys. J. **404**, 441 (1993).
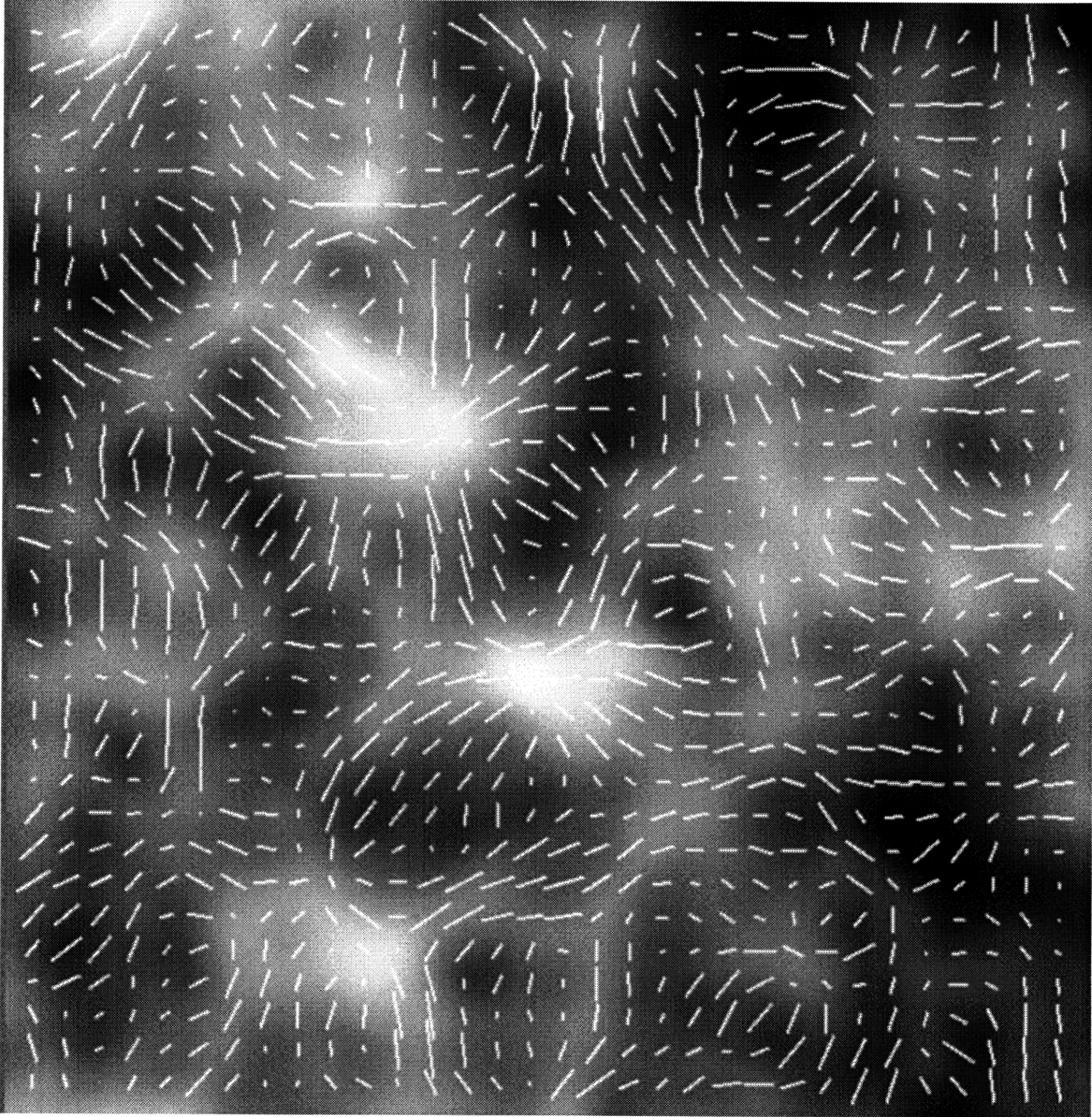
Figure 2-10: Simulated temperature and polarization map for SCDM ($2.5° \times 2.5°$ field). Only the correlated part of the polarization vectors are shown together with the map of the temperature. The temperature ranges from $-1690\mu K < T < 1810\mu K$ while the maximum amplitude of the polarization vectors is $P = 45\mu K$.

Chapter 3

The Line of Sight Integration[1]

The field of cosmic microwave background (CMB) anisotropies has seen a rapid development since its first detection by the COBE satellite only a few years ago. There are now several reported experimental results that are detecting anisotropies on degree angular scales (see [1] and [2] for a recent review), which together with a few upper limits on smaller angular scales already give interesting limits on cosmological models. With the development of the new generation of experiments now being proposed one hopes to accurately map the CMB sky from arcminute scales to several degree scales. The amount of data thus provided would allow for an unprecedented accuracy in the determination of cosmological parameters. Theoretical modeling shows that CMB anisotropies are sensitive to most of the cosmological parameters and have a distinctive advantage over other cosmological observations in that they probe the universe in the linear regime. This avoids the complications caused by physical processes in the nonlinear regime and allows to use powerful statistical techniques to search over the parameter space for the best cosmological model (see e.g. [3, 4, 5]).

A large stumbling block in this program has been the speed of theoretical model calculations, which are still too slow to allow for a rapid search over the parameter space. The development of a fast and accurate algorithm to calculate the anisotropies becomes essential to analyze the high quality data that the future promises to deliver.

---

[1]Based on U. Seljak & M. Zaldarriaga, Astrophys. J. **469**, 437 (1996) and M. Zaldarriaga, U. Seljak & E. Bertschinger, Astrophys. J. **494**, 491(1998).

The parameter space describing the possible models is so large that a search over parameter space would be impossible without a fast algorithm. Very fast approximate methods have been developed but can only provide a 10% accuracy. In this chapter we present an algorithm that is both very fast (more than two orders of magnitude faster that the usual Boltzmann approach) and exact within linear perturbation theory.

3.1 Einstein and Fluid Equations

In this section we present the Einstein and fluid differential equations for the metric, cold dark matter (CDM) and baryons that must be solved to calculate the CMB anisotropy spectra produced by density perturbations in our Universe. We will also present the Einstein equations for gravity waves. These equations are the basis of the traditional methods and are also used in the integral method, discussed this chapter. The derivation of the Einstein and fluid equations can be found in the literature (e.g. [6]), so we only present the final results. We restrict the treatment to spatially flat universes. The interested reader can find the generalization to arbitrary Robertson-Walker background in [7, 8].

The metric is written as

$$
\begin{aligned}
ds^2 &= -dt^2 + a^2(\delta_{ij} + h_{ij})dx^i dx^j \\
&= a^2[-d\tau^2 + (\delta_{ij} + h_{ij})dx^i dx^j],
\end{aligned}
\tag{3.1}
$$

where a is the expansion factor, x_i the comoving coordinates and $\tau = \int dt/a$ the conformal time. We are using units in which $c = 1$. The space part of the unperturbed metric is a Kronecker delta, δ_{ij} and h_{ij} is the metric perturbation in synchronous gauge [9]. The metric perturbations have contributions from scalar (density) and tensor (gravity waves) modes, $h_{ij} = h_{ij}^S + h_{ij}^T$. Although all observable quantities are identical in different gauges the computational efficiency to obtain them within a given accuracy is not. This criterion lead us to work in synchronous gauge. In comparison to the longitudinal gauge [10] it is about 20% more efficient with isentropic initial

conditions and even more so with isocurvature initial conditions, which are difficult to set up in the longitudinal gauge.

We start by considering perturbations produced by density modes. When working with linear theory in a flat universe it is convenient to use Fourier modes because they evolve independently. These modes are the eigenfunctions of the Laplacian operator that we shall call $G(\boldsymbol{k}, \boldsymbol{x})$,

$$\nabla^2 G(\boldsymbol{k}, \boldsymbol{x}) = -k^2 G(\boldsymbol{k}, \boldsymbol{x}). \tag{3.2}$$

We expand all the perturbations in terms of G and its spatial covariant derivatives. For example, the metric perturbations for a single mode are given by

$$h_{ij}^S = \frac{h}{3} \delta_{ij} G - (h + 6\eta)(k^{-2} G_{|ij} + \frac{1}{3} \delta_{ij} G), \tag{3.3}$$

where h and $(h + 6\eta)$ are the trace and traceless part of the metric perturbation. The perturbed Einstein's equations result in the following equations for h and η (Bertschinger 1996),

$$\begin{aligned}
k^2 \eta - \frac{1}{2} \frac{\dot{a}}{a} \dot{h} &= -8\pi G a^2 \delta\rho \\
k^2 \dot{\eta} &= 4\pi G a^2 (\bar{\rho} + \bar{p}) k v.
\end{aligned} \tag{3.4}$$

(G here stands for the gravitational constant and should not be confused with the mode functions $G(\boldsymbol{k}, \boldsymbol{x})$); $\delta\rho$ and v characterize the density and velocity perturbations ($v = i\hat{\boldsymbol{k}} \cdot \boldsymbol{v}$), $\delta\rho = \sum_j \bar{\rho}_j \delta_j$, $(\bar{\rho} + \bar{p})v = \sum_j (\bar{\rho}_j + \bar{p}_j)v_j$, where $\bar{\rho}_j$ and $\bar{p}_j$ are the mean density and pressure of the j-th species and the sum is carried out over all the different species in the universe.

The equation for the cold dark matter density perturbation δ_c is,

$$\dot{\delta_c} = -\frac{\dot{h}}{2}, \tag{3.5}$$

where by definition in this gauge the cold dark matter particles have zero peculiar ve-

locities. The Euler equation for the baryons has additional terms caused by Thomson scattering and pressure. Baryons have velocities relative to the dark matter,

$$
\begin{aligned}
\dot{\delta}_b &= -kv_b - \frac{\dot{h}}{2}, \\
\dot{v}_b &= -\frac{\dot{a}}{a}v_b + c_s^2 k\delta_b + \frac{4\bar{\rho}_\gamma}{3\bar{\rho}_b}an_e x_e \sigma_T(v_\gamma - v_b).
\end{aligned}
\tag{3.6}
$$

Here c_s is the baryon sound speed, v_b is the baryon velocity, v_γ is given by the temperature dipole $v_\gamma = 3\Delta_{T1}$ and $\bar{\rho}_\gamma$, $\bar{\rho}_b$ are the mean photon and baryon densities respectively. The Thomson scattering cross section is σ_T, n_e is the electron density and x_e is the ionization fraction.

There are two independent degrees of freedom or polarizations for gravity waves. The purturbed metric for each is,

$$
h_{ij}^{T(\pm)} = (\hat{e}_1 \pm i\hat{e}_2)_i \, (\hat{e}_1 \pm i\hat{e}_2)_j \, h_t(\tau) \, G(\boldsymbol{k},\boldsymbol{x}),
\tag{3.7}
$$

the $\pm$ labels the polarization mode of the gravity wave and $(\hat{e}_1, \hat{e}_2, \hat{k})$ form an orthogonal basis. The Einstein equations lead to

$$
\ddot{h}_t + 2\frac{\dot{a}}{a}\dot{h}_t + k^2 h_t = 0.
\tag{3.8}
$$

We have neglected the source terms on the right hand side produced by the neutrino and photon anisotropic stress. It is straightforward to add this source, but it has a negligible effect in practice because for modes outside the horizon free streaming cannot create a shear while for modes inside the horizon the $k^2 h_t$ term in (3.8) becomes dominant over the source terms.

3.2   Boltzmann equation

The photons are described using their distribution function which depends on time, spatial position and direction of propagation of the photons ($\hat{n}$). In fact polarization depends also on the two axes perpendicular to $\hat{n}$ used to define the Stokes parameters.

The evolution of the distribution function is described using the Boltzmann equation which states that when one follows a light ray the temperature or polarization of the radiation can change for two independent reasons: gravitational redshifts or blueshifts and Thomson scatterings. We can then write,

$$\frac{dX}{d\tau} = \frac{\partial X}{\partial \tau} + \hat{n}^i \frac{\partial X}{\partial x_i} = \dot{X}_{gravity} + \dot{X}_{thomson},$$ (3.9)

$X = T or (Q \pm iU)$ which we introduced in Chapter 2 to characterize the fractional fluctuations in the CMB field (ie. $T = \frac{\delta T}{T_0} = \frac{\delta I}{4I}$). The temperature of the CMB blackbody can be used instead of the intensity at a particular wavelength because both the gravitational redshift and Thomson scattering preserve the blackbody nature of the spectrum. The gravity source only acts on the temperature equation and not on the polarization,

$$\dot{T}_{gravity} = -\frac{1}{2} \, \hat{n}^i \hat{n}^j \dot{h}_{ij}.$$ (3.10)

This equation is valid for both density modes and gravity waves. We will derive the Thomson scattering source in 3.2.1.

3.2.1   Thomson scattering

The Thomson scattering cross section is,

$$\frac{d\sigma}{d\Omega} = \frac{3\sigma_T}{8\pi} |\tilde{\epsilon} \cdot \tilde{\epsilon}'|^2,$$ (3.11)

where σ_T is the Thomson scattering cross section and $\tilde{\epsilon}$ and $\tilde{\epsilon}'$ are the unit vectors that describe the polarization of the electric field of the scattered and incoming radiation respectively. The scattering terms in equations (3.9) are most easily computed in the coordinate system where the incident photons travel along the $\hat{z}$ axes and the electrons are at rest. If $\hat{n}'$ is the direction of the incident photon and $\hat{n}$ that of the scattered one then $\hat{n}' = \hat{z} = (\theta = 0, \phi = 0)$ and (θ, ϕ) describe $\hat{n}$. For a given scattering event, the Thomson scattering matrix is the simplest when expressed in terms of the intensities of radiation parallel ($\tilde{T}_{\parallel}$) and perpendicular ($\tilde{T}_{\perp}$) to the plane

containing both $\hat{n}$ and $\hat{n}'$. Equation (3.11) leads to the following relation between incoming and scattered radiation,

$$
\begin{aligned}
\tilde{T}_\| &= \frac{3}{16\pi}\cos^2\theta\ \tilde{T}_\|' \\
\tilde{T}_\perp &= \frac{3}{16\pi}\ \tilde{T}_\perp' \\
\tilde{U} &= \frac{3}{16\pi}\cos\theta\ \tilde{U}'.
\end{aligned}
\tag{3.12}
$$

We have normalized the equation (3.12) so that the number of photons is conserved by the scattering. In this way we only need to introduce the scattering rate to obtain the terms needed in the Boltzmann eqaution. The total intensity is the sum of the two components, $\tilde{T} = \tilde{T}_\| + \tilde{T}_\perp$, while the difference gives polarization $\tilde{Q} = \tilde{T}_\| - \tilde{T}_\perp$. Because the components are measured using this coordinate system, defined by the plane that contains both $\hat{n}$ and $\hat{n}'$, the Stokes parameters of the incoming radiation $\tilde{Q}'$ and $\tilde{U}'$ depend on the angle ϕ of the scattered photon, while $\tilde{Q}$ and $\tilde{U}$ are already measured relative to the correct frame. It is more useful to refer the Stokes parameters of the incoming radiation relative to a fixed frame. To achieve this we construct the scattering matrix in terms of T', $Q' + iU' = \exp(2i\phi)(\tilde{Q}' + i\tilde{U}')$ and $Q' - iU' = \exp(-2i\phi)(\tilde{Q}' - i\tilde{U}')$, where we have used the transformation law (equation 2.1) to relate the two sets of Stokes parameters.

Equation (3.12) implies that the scattered radiation in direction $\hat{n}$ which initially came in direction $\hat{n}'$ is

$$
\begin{aligned}
\delta T(\hat{n}',\hat{n}) &= \frac{1}{4\pi}\left[\frac{3}{4}(1+\cos^2\theta)T' + \frac{3}{8}(\cos^2\theta-1)e^{-2i\phi}(Q'+iU')+\right. \\
&\quad \left. \frac{3}{8}(\cos^2\theta-1)e^{2i\phi}(Q'-iU')\right] \\
\delta(Q\pm iU)(\hat{n}',\hat{n}) &= \frac{1}{4\pi}\left[\frac{3}{4}(\cos^2\theta-1)T' + \frac{3}{8}(1\pm\cos\theta)^2 e^{-2i\phi}(Q'+iU')+\right. \\
&\quad \left. \frac{3}{8}(1\mp\cos\theta)^2 e^{2i\phi}(Q'-iU')\right].
\end{aligned}
\tag{3.13}
$$

We introduced a δ to indicate that the final expression for the scattered field is an

70

integral over all directions $\hat{n}'$,

$$\dot{X}(\hat{n})|_{Thomson} = -a\sigma_T n_e \, x_e \left[X(\hat{n}) + \int d\Omega' \delta X(\hat{n}', \hat{n}) \right], \qquad (3.14)$$

X stands for T and $(Q \pm iU)$. We introduced the scattering rate $a\sigma_T n_e \, x_e$ where $n_e \, x_e$ is the density of ionized electrons. The first term accounts for the photons that are scattered away from the line of sight and the expansion factor a is introduced because we are calculating the derivative with respect to conformal time.

Equation (3.13) for the scattering matrix is written in the frame where $\hat{n}' = (\theta' = 0, \phi' = 0)$. The first spherical harmonics are explicitly $_{\pm 2}Y_2^2(\hat{n}) = \sqrt{\frac{1}{16\pi}}(1\mp\cos\theta)^2 e^{2i\phi}$, $_{\pm 2}Y_2^{-2}(\hat{n}) = \sqrt{\frac{1}{16\pi}}(1\pm\cos\theta)^2 e^{-2i\phi}$ and $_{\pm 2}Y_2^0(\hat{n}) = \sqrt{\frac{15}{64\pi}}(1-\cos^2\theta)$. These together with $_0Y_0^m(\hat{n}') = \sqrt{\frac{1}{4\pi}}\delta_{m0}$, $_0Y_2^m(\hat{n}') = \sqrt{\frac{5}{4\pi}}\delta_{m0}$, and $_{\pm 2}Y_2^m(\hat{n}') = \sqrt{\frac{5}{4\pi}}\delta_{m\mp2}$ enable us to rewrite (3.13) in a more useful form (δ_{ij} is the Kronecker delta),

$$\begin{aligned}
\delta T(\hat{n}', \hat{n}) &= \sigma_T \sum_m \Big[\Big(\frac{1}{10} \, _0Y_2^m(\hat{n}) \, _0\bar{Y}_2^m(\hat{n}') + \, _0Y_0^m(\hat{n}) \, _0\bar{Y}_0^m(\hat{n}') \Big) T' \\
&\quad - \frac{3}{20}\sqrt{\frac{2}{3}} \, _0Y_2^m(\hat{n}) \, _2\bar{Y}_2^m(\hat{n}') \, (Q' + iU') \\
&\quad - \frac{3}{20}\sqrt{\frac{2}{3}} \, _0Y_2^m(\hat{n}) \, _{-2}\bar{Y}_2^m(\hat{n}')(Q' - iU') \Big] \\
\delta(Q \pm iU)(\hat{n}', \hat{n}) &= \sigma_T \sum_m \Big[-\frac{6}{20}\sqrt{\frac{2}{3}} \, _{\pm 2}Y_2^m(\hat{n}) \, _0\bar{Y}_2^m(\hat{n}')T' \\
&\quad + \frac{6}{20} \, _{\pm 2}Y_2^m(\hat{n}) \, _2\bar{Y}_2^m(\hat{n}')(Q' + iU') + \\
&\quad \frac{6}{20} \, _{\pm 2}Y_2^m(\hat{n}) \, _{-2}\bar{Y}_2^m(\hat{n}')(Q' - iU') \Big].
\end{aligned} \qquad (3.15)$$

This form has the advantage of being independent of the coordinate system. We will use the scattering matrix in the frame where $\mathbf{k} \parallel \hat{z}$ and not $\hat{n}' = \hat{z}$. Here $\mathbf{k}$ is the wavevector of the Fourier mode under consideration. The addition theorem for the spin harmonics (2.15) can be used to show that the sum $\sum_m \, _sY_l^m(\hat{n}) \, _{s'}\bar{Y}_l^m(\hat{n}')$ acquires a phase change under rotation of the coordinate system that exactly cancels the phase change in the transformation of $(Q \pm iU)$ in equation (3.15). We may therefore use this equation in any coordinate system.

71

3.2.2 Density fluctuations

As we are dealing with a linear problem with a spatially constant background we may consider only one eigenmode of the Laplacian at a time. We may choose without loss of generality that $\boldsymbol{k} \parallel \hat{\boldsymbol{z}}$. To define the Stokes parameters we use the spherical coordinate unit vectors $(\hat{\boldsymbol{e}}_\theta, \hat{\boldsymbol{e}}_\phi)$.

The density field produced by a single mode has two important symmetries. It is invariant under rotations around $\boldsymbol{k}$ and parity operations where the x or y axes change sign ($\boldsymbol{k} \parallel \hat{\boldsymbol{z}}$). By invariant we mean that the transformed density field $\rho'(\boldsymbol{x}) = \rho(\boldsymbol{x})$, there is no prime in the argument of ρ'. What is directly relevant to the calculation of the anisotropies is that the gravity source term $\hat{n}^i \hat{n}^j h_{ij}^S / 2$ satisfies these symmetries. The rotational symmetry implies that the neither the temperature nor the Stokes parameters (in the spherical basis) can depend on ϕ. The parity symmetry has interesting consequences on the allowed polarization patterns as well. For simplicity we focus on the Stokes parameters at the origin. Symmetry implies that $(Q \pm iU)'(\hat{\boldsymbol{n}}) = (Q \pm iU)(\hat{\boldsymbol{n}})$ for both rotation and parity operations. We consider a parity operation that changes the sign of the y axes. If we consider the direction $\hat{\boldsymbol{n}} = (\theta, 0)$ when we apply the transformation its location remains unchanged, $\hat{\boldsymbol{n}}' = \hat{\boldsymbol{n}}$. On the other hand $\hat{\boldsymbol{e}}_\phi$, used to define the Stokes parameters changes sign. As a consequence U changes sign, $U'(\hat{\boldsymbol{n}}') = -U(\hat{\boldsymbol{n}})$. This is inconsistent with the symmetry statement unless U is zero. If U is zero in this particular direction it has to be zero in all directions because of the rotational symmetry. In this particular coordinate system only Q is different from zero and we denote it by Δ_P^S, so that $\Delta_P^S = Q = Q \pm iU$ ($U = 0$). The temperature anisotropy for the single eigenmode is denoted by Δ_T^S. We introduced a Δ in the notation to enphasize that these are the contributions of one mode. The total field T, Q and U are obtained by adding the contribution of all modes.

For a plane wave, rotational symmetry implies that both Δ_T^S and Δ_P^S depend only on the angle between $\hat{\boldsymbol{n}}$ and $\hat{\boldsymbol{z}}$ ($\boldsymbol{k} \parallel \hat{\boldsymbol{z}}$), so only harmonics with $m = 0$ (which do not depend on ϕ), are needed in the expansion. To calculate the evolution of these two

quantities we expand them as,

$$
\begin{aligned}
\Delta_T^S(\boldsymbol{k}, \hat{\boldsymbol{n}}) &= G(\boldsymbol{k}, \boldsymbol{x}) \sum_l (-i)^l \sqrt{4\pi(2l+1)} \Delta_{Tl}^S \, Y_l^0(\hat{\boldsymbol{n}}) \\
&= G(\boldsymbol{k}, \boldsymbol{x}) \sum_l (-i)^l (2l+1) \Delta_{Tl}^S P_l(\mu) \\
\Delta_P^S(\boldsymbol{k}, \hat{\boldsymbol{n}}) &= G(\boldsymbol{k}, \boldsymbol{x}) \sum_l (-i)^l \sqrt{4\pi(2l+1)(l+2)!/(l-2)!} \,_2\Delta_{Pl}^S \,_2Y_l^0(\hat{\boldsymbol{n}}) \\
&= G(\boldsymbol{k}, \boldsymbol{x}) \sum_l (-i)^l \sqrt{4\pi(2l+1)(l+2)!/(l-2)!} \,_{-2}\Delta_{Pl}^S \,_{-2}Y_l^0(\hat{\boldsymbol{n}}) \\
&= G(\boldsymbol{k}, \boldsymbol{x}) \sum_l (-i)^l (2l+1) \,_{\pm 2}\Delta_{Pl}^S P_l^2(\mu) \qquad (3.16)
\end{aligned}
$$

where $G(\boldsymbol{k}, \boldsymbol{x}) = \exp(i\boldsymbol{k} \cdot \boldsymbol{x})$ and $\mu = \hat{\boldsymbol{k}} \cdot \hat{\boldsymbol{n}}$. We added a subindex ± 2 to $_{\pm 2}\Delta_{Pl}^S$ to denote that they are the expansion coefficients in spin ± 2 harmonics [2] and we used the explicit expression for spin s harmonics with $m = 0$ to write them in terms of associated Legendre polynomials [11],

$$
\begin{aligned}
Y_l^0(\theta, \phi) &= \sqrt{\frac{(2l+1)}{4\pi}} P_l(\cos\theta) \\
_{\pm 2}Y_l^0(\theta, \phi) &= \sqrt{\frac{(2l+1)}{4\pi}\frac{(l-2)!}{(l+2)!}} P_l^2(\cos\theta). \qquad (3.17)
\end{aligned}
$$

As stated above, scalar modes in this reference frame have $U = 0$, so Δ_P^S describes both spin ± 2 quantities. For $m = 0$ one has $_2Y_l^0 = {}_{-2}Y_l^0$ and so $_2\Delta_{Pl}^S = {}_{-2}\Delta_{Pl}^S$. This is a very important result, because the fact that both coefficients are equal implies that this single Fourier mode does not produce any B mode polarization (equation 2.6). The observed polarization field is the superposition of that produced by each Fourier mode, and thus we have shown that the pattern of polarization produced by density perturbations has no B component. Note that B is invariant under rotations so the fact that we have proved this result in a particular reference frame that depends on $\boldsymbol{k}$ is not important. This conclusion does not apply to U: although it is zero in this particular frame it is not in others. When we superimpose the perturbations of

---

[2]The relation between these coefficient and those used in Zaldarriaga & Seljak (1997) is $_{\pm 2}\Delta_{Pl}^S = -\sqrt{(l-2)!/(l+2)!}\Delta_{El}^S$.

all modes B remains zero while U does not.

We can replace equation (3.16) into (3.9) and use the expresion for the gravitational redshift, equations (3.3) and (3.10), to obtain the Boltzmann equation for the CMB photons;

$$
\begin{aligned}
\dot{\Delta}^S_T + ik\mu\Delta^S_T &= -\frac{1}{6}\dot{h} - \frac{1}{3}(\dot{h} + 6\dot{\eta})P_2(\mu) + \dot{\Delta}^S_{T|Thomson} \\
\dot{\Delta}^S_P + ik\mu\Delta^S_P &= \dot{\Delta}^S_{P|Thomson}.
\end{aligned}
\tag{3.18}
$$

The first term in the temperature equation represents the effect of gravitational redshift, while $\dot{\Delta}^S_{T|Thomson}$ and $\dot{\Delta}^S_{P|Thomson}$ are the changes in the photon distribution function produced by Thomson scattering. After inserting equation (3.16) into equation (3.18) one obtains a system of two coupled hierarchies, one for the temperature and the other for polarization,

$$
\begin{aligned}
\dot{\Delta}^S_{T0} &= -k\Delta^S_{T1} - \frac{\dot{h}}{6} + \dot{\Delta}^S_{T0|Thomson} \\
\dot{\Delta}^S_{T1} &= \frac{k}{3}\left[\Delta^S_{T0} - 2\Delta^S_{T2}\right] + \dot{\Delta}^S_{T1|Thomson} \\
\dot{\Delta}^S_{T2} &= \frac{k}{5}\left[2\Delta^S_{T1} - 3\Delta^S_{T3}\right] + \frac{2}{15}k^2\alpha + \dot{\Delta}^S_{T2|Thomson} \\
\dot{\Delta}^S_{Tl} &= \frac{k}{2l+1}\left[l\Delta^S_{T(l-1)} - (l+1)\Delta^S_{T(l+1)}\right] + \dot{\Delta}^S_{Tl|Thomson}, \, l > 2 \\
{}_2\dot{\Delta}^S_{Pl} &= \frac{k}{2l+1}\left[(l-2)\,{}_2\Delta^S_{Pl-1} - (l+3)\,{}_2\Delta^S_{Pl+1}\right] + {}_2\dot{\Delta}^S_{Pl|Thomson},
\end{aligned}
\tag{3.19}
$$

where $\alpha = (\dot{h}+6\dot{\eta})/2k^2$, and we wrote sepatarely the first 3 equations of the temperature hierarchy that contain the gravity sources. We also used the recurrence relations for the Legendre functions,

$$
\begin{aligned}
\mu P_l(\mu) &= \frac{1}{2l+1}\left[l\, P_{l-1} + (l+1)P_{l+1}\right] \\
\mu P_l^2(\mu) &= \frac{1}{2l+1}\left[(l+2)P_{l-1}^2 + (l-1)P_{l+1}^2\right].
\end{aligned}
\tag{3.20}
$$

Substituting the expansion for the Stokes parameters from equation (3.16) into

equation (3.15) and using equation (3.14) we find

$$\dot{\Delta}^S_{Tl}|_{Thomson} \equiv -a\sigma_T n_e x_e \left[\Delta^S_{Tl} + \int d\Omega \, _0Y^m_l(\hat{n})\delta T(\hat{n}) \right]$$

$$= \dot{\kappa}(-\Delta^S_{Tl} + \Delta^S_{T0}\delta_{l0} + \frac{\Pi}{10}\delta_{l2})$$

$$_{\pm 2}\dot{\Delta}^S_{Pl}|_{Thomson} \equiv -a\sigma_T x_e n_e \left[_{\pm 2}\Delta^S_{Pl} + \int d\Omega \, _2Y^m_l(\hat{n}) \, \delta(Q \pm iU)(\hat{n}) \right]$$

$$= \dot{\kappa}(- \, _{\pm 2}\Delta^S_{Pl} - \frac{\Pi}{20}\delta_{l2}) \qquad (3.21)$$

with

$$\Pi = \Delta^S_{T2} - 6(\, _2\Delta^S_{P2} + \, _{-2}\Delta^S_{P2}). \qquad (3.22)$$

The differential optical depth for Thomson scattering is denoted $\dot{\kappa} = an_e x_e \sigma_T$. Note that the polarization has sources only at $l = 2$. Equation (3.21) is valid in the rest frame of the electrons, so in the reference frame where the baryon velocity is v_b the distribution of scattered radiation has an additional dipole. The final expression for the Boltzmann hierarchy is

$$\dot{\Delta}^S_{T0} = -k\Delta^S_{T1} - \frac{\dot{h}}{6}$$

$$\dot{\Delta}^S_{T1} = \frac{k}{3}\left[\Delta^S_{T0} - 2\Delta^S_{T2} \right] + \dot{\kappa}\left(\frac{v_b}{3} - \Delta^S_{T1} \right)$$

$$\dot{\Delta}^S_{T2} = \frac{k}{5}\left[2\Delta^S_{T1} - 3\Delta^S_{T3} \right] + \frac{2}{15}k^2\alpha + \dot{\kappa}\left[\frac{\Pi}{10} - \Delta^S_{T2} \right]$$

$$\dot{\Delta}^S_{Tl} = \frac{k}{2l+1}\left[l\Delta^S_{T(l-1)} - (l+1)\Delta^S_{T(l+1)} \right] - \dot{\kappa}\Delta^S_{Tl}, l > 2$$

$$_2\dot{\Delta}^S_{Pl} = \frac{k}{2l+1}\left[(l-2)\, _2\Delta^S_{Pl-1} - (l+3)\, _2\Delta^S_{Pl+1} \right] - \dot{\kappa}\, _2\Delta^S_{Pl} - \frac{1}{20}\dot{\kappa}\Pi\delta_{l2}. \quad (3.23)$$

The last important ingredient is the relation between $\Delta^S_{(T,P)}$ for each Fourier mode and the observed CMB power spectra. For a single mode we can combine equations (2.5) and (3.16) to show

$$a_{T,lm} = (-i)^l \sqrt{4\pi(2l+1)} \, \Delta^S_{Tl} \, G(\boldsymbol{k}, \boldsymbol{x}) \, \delta_{m,0}$$

$$a_{E,lm} = (-i)^l \sqrt{4\pi(2l+1)} \, \Delta^S_{El} \, G(\boldsymbol{k}, \boldsymbol{x}) \, \delta_{m,0}$$

$$a_{B,lm} = 0 \qquad (3.24)$$

with $\Delta_{E,l}^S = -\sqrt{(l+2)!/(l-2)!}\ {}_{\pm 2}\Delta_{Pl}^S$.

The different Fourier modes are statistically independent so the observed total power in the integral of the powers produced by all modes,

$$
\begin{aligned}
C_{(T,E)l} &= (4\pi)^2 \int k^2 dk P(k) |\Delta_{(T,E)l}^S(k, \tau = \tau_0)|^2 \\
C_{Cl} &= (4\pi)^2 \int k^2 dk P(k) \Delta_{Tl}^S(k, \tau = \tau_0) \Delta_{El}^S(k, \tau = \tau_0)
\end{aligned}
\tag{3.25}
$$

with $P(k)$ the primordial power spectrum. The primordial power spectrum gives the power in each mode at the initial time. For example if we choose to normalize the initial conditions so that $\delta_c = 1$ then $P(k)$ gives the initial power in the cold dark matter component.

3.2.3 Gravity waves

For the gravity wave modes the source term in the temperature equation is $\frac{1}{2}\hat{n}^i\hat{n}^j h_{ij}^{T(\pm)} = \frac{1}{2}(1 - \cos^2\theta)e^{\pm i2\phi}\ h_t\ G(\boldsymbol{k}, \boldsymbol{x})$. There is an explicit ϕ dependence of the source so the symmetries of rotation and parity satisfied by the density modes discussed in the previous section no longer apply. This implies that U is no longer zero and that gravity waves will produce a non-zero B. This is a crucial point and may allow in the future to detect the stochastic background of gravity waves if it is present in our universe. We will discuss this further in section 4.3.

For gravity waves we can expand,

$$
\begin{aligned}
\Delta_T^{T(\pm)}(\boldsymbol{k}, \hat{\boldsymbol{n}}) &= G(\boldsymbol{k}, \boldsymbol{x}) \sum_l (-i)^l \sqrt{4\pi(2l+1)\,(l+2)!/(l-2)!} \\
&\quad \times \Delta_{Tl}^{T(\pm)}\ Y_l^{\pm 2}(\hat{\boldsymbol{n}}) \\
(\Delta_Q^{T(\pm)} + i\Delta_U^{T(\pm)})(\boldsymbol{k}, \hat{\boldsymbol{n}}) &= G(\boldsymbol{k}, \boldsymbol{x}) \sum_l (-i)^l \sqrt{4\pi(2l+1)}(l+2)!/(l-2)! \\
&\quad \times {}_{+2}\Delta_{Pl}^{T(\pm)}\ {}_2Y_l^{\pm 2}(\hat{\boldsymbol{n}}) \\
(\Delta_Q^{T(\pm)} - i\Delta_U^{T(\pm)})(\boldsymbol{k}, \hat{\boldsymbol{n}}) &= G(\boldsymbol{k}, \boldsymbol{x}) \sum_l (-i)^l \sqrt{4\pi(2l+1)}(l+2)!/(l-2)! \\
&\quad \times {}_{-2}\Delta_{Pl}^{T(\pm)}\ {}_{-2}Y_l^{\pm 2}(\hat{\boldsymbol{n}}).
\end{aligned}
\tag{3.26}
$$

Because of the ϕ dependence of the source term we had to use harmonics with $m = \pm 2$ for the two different gravity wave polarizations.

Now that $_{+2}\Delta_{Pl}^{T(\pm)} \neq _{-2}\Delta_{Pl}^{T(\pm)}$, we need two different hierarchies to solve for both of them separately. The derivation of the hierarchies is analogous to that for the density modes yielding,

$$
\dot{\Delta}_{Tl}^{T(\pm)} = \frac{k}{2l+1}\left[(l-2)\Delta_{Tl-1}^{T(\pm)} - (l+3)\Delta_{Tl+1}^{T(\pm)}\right] + \frac{\dot{h}_t}{30}\delta_{l2} + \dot{\Delta}^{T(\pm)}{}_{Tl|Thomson}
$$

$$
\begin{aligned}
_{\pm 2}\dot{\Delta}_{Pl}^{T(\pm)} = & \frac{k}{2l+1}\left[\frac{(l-2)^2}{l}\,_{\pm 2}\Delta_{Pl-1}^{T(\pm)} \pm \frac{20i}{l(l+1)}\,_{\pm 2}\Delta_{Pl}^{T(\pm)}\right. \\
& \left. - \frac{(l+3)^2}{l+1}\,_{\pm 2}\Delta_{Pl+1}^{T(\pm)}\right] + \dot{\Delta}_{Pl|Thomson}^{T(\pm)},
\end{aligned}
\tag{3.27}
$$

with

$$
\begin{aligned}
\dot{\Delta}_{Tl|Thomson}^{T(\pm)} &= -\dot{\kappa}(\Delta^{T(\pm)}{}_{Tl} - \frac{1}{10}\Pi\,\delta_{l2}) \\
\dot{\Delta}_{Pl|Thomson}^{T(\pm)} &= -\dot{\kappa}(\Delta^{T(\pm)}{}_{Pl} + \frac{1}{20}\Pi\,\delta_{l2}) \\
\Pi &= \Delta_{T2}^{T(\pm)} - 6\left[_{+2}\Delta_{P2}^{T(\pm)} + _{-2}\Delta_{P2}^{T(\pm)}\right].
\end{aligned}
\tag{3.28}
$$

We can change variables to obtain hierarchies for E and B directly,

$$
\begin{aligned}
\dot{\Delta}_{\tilde{E}l}^{T(\pm)} = & \frac{k}{2l+1}\left[\frac{(l-2)(l+2)}{l}\,\Delta_{\tilde{E}l-1}^{T(\pm)} - \frac{20}{l(l+1)}\,\Delta_{\tilde{B}l}^{T(\pm)}\right. \\
& \left. + \frac{(l+3)(l-1)}{l+1}\,\Delta_{\tilde{E}l+1}^{T(\pm)}\right] - \dot{\kappa}\Delta_{\tilde{E}l}^{T(\pm)} + \dot{\kappa}/20\Pi\,\delta_{l2}
\end{aligned}
\tag{3.29}
$$

$$
\begin{aligned}
\dot{\Delta}_{\tilde{B}l}^{T(\pm)} = & \frac{k}{2l+1}\left[\frac{(l-2)(l+2)}{l}\,\Delta_{\tilde{B}l-1}^{T(\pm)} + \frac{20}{l(l+1)}\,\Delta_{\tilde{E}l}^{T(\pm)}\right. \\
& \left. + \frac{(l+3)(l-1)}{l+1}\,\Delta_{\tilde{E}l+1}^{T(\pm)}\right] - \dot{\kappa}\Delta_{\tilde{B}l}^{T(\pm)}
\end{aligned}
\tag{3.30}
$$

$$
\Delta_{\tilde{T},l}^{T(\pm)} = \sqrt{\frac{(l+2)!}{(l-2)!}}\,\Delta_{Tl}^{T(\pm)}
$$

$$
\Delta_{\tilde{E},l}^{T(\pm)} = -\frac{(l+2)!}{(l-2)!}\left(_{+2}\Delta_{Pl}^{T(\pm)} + _{-2}\Delta_{Pl}^{T(\pm)}\right)/2
$$

$$\Delta_{\tilde{B},l}^{T(\pm)} = -\frac{(l+2)!}{(l-2)!}\left({}_{+2}\Delta_{Pl}^{T(\pm)} - {}_{-2}\Delta_{Pl}^{T(\pm)} \right)/2i, \tag{3.31}$$

with $\Pi = \Delta_{T2}^{T(\pm)} - 6({}_{+2}\Delta_{P2}^{T(\pm)} + {}_{-2}\Delta_{P2}^{T(\pm)}) = (\Delta_{\tilde{T}2}^{T(\pm)} + \sqrt{6}\Delta_{\tilde{E}2}^{T(\pm)})/\sqrt{4!}$. We introduced tildes in the notation to remind the reader that we introduced extra l dependent factors for later convenience. Free streaming couples E and B modes, but the Thomson scattering only creates E (the $\dot{\kappa}\Pi/20$ term is only present in the E hierarchy). It is through freestreaming and not scattering that B is created.

Finally the relation between the observed CMB power spectra and the perturbations for each mode is,

$$C_{(T,E,B)l} = (4\pi)^2 \int k^2 dk P_t(k) |\Delta_{(\tilde{T},\tilde{E},\tilde{B})l}^{T(\pm)}(k,\tau=\tau_0)|^2$$

$$C_{Cl} = (4\pi)^2 \int k^2 dk P_t(k) \Delta_{\tilde{T}l}^{S}(k,\tau=\tau_0)\Delta_{\tilde{E}l}^{T(\pm)}(k,\tau=\tau_0), \tag{3.32}$$

where $P_h(k)$ denotes the initial power spectrum for the gravity waves and we normalized the initial conditions to $h_t = 1$

The results for scalars ($m = 0$) and tensors ($m = 2$) can all be combined (the following formulas also applies to vector modes with $m = 1$). We expand all variables as,

$$X = G(k,x)\sum_l(-i)^l \sqrt{4\pi(2l+1)\frac{(l+|s|)!}{(l-|s|)!}\frac{(l+|m|)!}{(l-|m|)!}} \, _s\Delta_{Xl} \, _sY_l^m. \tag{3.33}$$

The expansion coefficients will satisfy the hierarchy,

$$\dot{\Delta}_{Xl} = \frac{k}{(2l+1)}\left[\frac{(l-|m|)(l-|s|)}{l}\Delta_{Xl-1} - \frac{(l+|m|+1)(l+|s|+1)}{(l+1)}\right.$$

$$\times \left. \Delta_{Xl+1} + \frac{sm(2l+1)}{l(l+1)}\Delta_{Xl}\right] - \dot{\kappa}\Delta_{Xl} + \frac{1}{10}P_X\delta_{l2}$$

$$P_T = \Pi$$

$$P_{Q\pm iU} = \Pi/2, \tag{3.34}$$

with $\Pi = \Delta_{T2}^{T(\pm)} - 6({}_{+2}\Delta_{P2}^{T(\pm)} + {}_{-2}\Delta_{P2}^{T(\pm)})$. Similar expressions can be written for the

E and *B* hierarchies. Equation (3.34) does not include the gravitational redshift term or the Doppler shift caused by the the baryon velocity which must be must be added to the temperature equation. In the general case we can define

$$\Delta_{\tilde{T},l} = \sqrt{\frac{(l+|m|)!}{(l-|m|)!}}\,\Delta_{Tl}$$

$$\Delta_{\tilde{E},l} = -\sqrt{\frac{(l+|m|)!\,(l+2)!}{(l-|m|)!\,(l-2)!}}\left(\Delta_{(Q+iU)l} + \Delta_{(Q-iU)l}\right)/2$$

$$\Delta_{\tilde{B},l} = -\sqrt{\frac{(l+|m|)!\,(l+2)!}{(l-|m|)!\,(l-2)!}}\left(\Delta_{(Q+iU)l} - \Delta_{(Q-iU)l}\right)/2i \qquad (3.35)$$

and use equation (3.32) to calculate the observer power spectra.

3.3   The Line of Sight Method

Instead of solving the coupled system of differential equations (3.23) one may formally integrate equations (3.18) along the photon past light cone to obtain (e.g. [14]),

$$\Delta_T^S(k,\tau_0) = \int_0^{\tau_0} d\tau\, e^{ik\mu(\tau-\tau_0)} e^{-\kappa}\{\dot{\kappa}e^{-\kappa}[\Delta_{T0}^S + i\mu v_b + \frac{1}{2}P_2(\mu)\Pi]$$
$$- \frac{1}{6}\dot{h} - \frac{1}{3}(\dot{h}+6\dot{\eta})P_2(\mu)\}$$

$$\Delta_P^S(k,\tau_0) = \frac{1}{4}\int_0^{\tau_0} d\tau\, e^{ik\mu(\tau-\tau_0)} e^{-\kappa}\dot{\kappa}\Pi P_2^2(\mu). \qquad (3.36)$$

These lead to equations for the multipoles,

$$\Delta_{Tl}^S(k,\tau=\tau_0) = \int_0^{\tau_0} S_T^S(k,\tau)j_l(x)d\tau$$

$$_2\Delta_{Pl}^S(k,\tau=\tau_0) = \int_0^{\tau_0} S_P^S(k,\tau)\frac{j_l(x)}{x^2}d\tau$$

$$x = k(\tau_0-\tau) \qquad (3.37)$$

where the source functions are,

$$S_T^S(k,\tau) = g\left(\Delta_{T0}^S + 2\dot{\alpha} + \frac{\dot{v}_b}{k} + \frac{\Pi}{4} + \frac{3\ddot{\Pi}}{4k^2}\right)$$

$$+ \quad e^{-\kappa}(\dot{\eta} + \ddot{\alpha}) + \dot{g}\left(\frac{v_b}{k} + \alpha + \frac{3\dot{\Pi}}{4k^2}\right) + \frac{3\ddot{g}\Pi}{4k^2}$$

$$S_P^S(k,\tau) = -\frac{3}{4}g\Pi. \qquad (3.38)$$

where $\alpha = (\dot{h} + 6\dot{\eta})/2k^2$, $j_l(x)$ are the spherical Bessel functions and g is the visibility function $g = \dot{\kappa}\exp(-\kappa)$. The source function for the temperature looks rather complicated because we have done several integrations by parts to express everything in terms of $j_l(x)$ rather than its derivatives. The polarization solution is straightforward to check. It is enough to substitute equation (3.38) into the hierarchy (3.23) using the limit $\lim_{x\to 0} j_l(x)/x^2 = 1/15$ and the recursion,

$$\frac{d}{dx}\left(\frac{j_l(x)}{x^2}\right) = \frac{1}{(2l+1)}\left[(l-2)\frac{j_{l-1}(x)}{x^2} - (l+3)\frac{j_{l+1}(x)}{x^2}\right]. \qquad (3.39)$$

Some of the terms in the source function $S_T^S(\tau)$ are easily recognizable. It may be simpler to express them in the more familiar conformal Newtonian gauge, $\Delta_{T0}^{synch} + \dot{\alpha} = \Delta_{T0}^{conf} + \psi$, $v_b^{synch} + k\dot{\alpha} = v_b^{conf}$ and $\ddot{\alpha} + \dot{\eta} = \dot{\phi} + \dot{\psi}$. Here ϕ and ψ are the conformal gauge gravitational potentials. All moments higher than $l = 1$ are gauge invariant, so in fact the source terms $S_{(T,P)}$ must be gauge invariant. The first two contributions in the source S_T^S (equation 3.38) $\Delta_{T0} + \dot{\alpha}$ are the intrinsic temperature and gravitational potential contributions from the last-scattering surface, while the third contribution is part of the velocity term, the other part being $k^{-1}\dot{g}v_b + \alpha$ in the next line. These terms make a dominant contribution to the anisotropy in the standard recombination models. The first term in the second line is the so-called integrated Sachs-Wolfe term and is important after recombination. It is especially important if matter-radiation equality occurs close to the recombination or in $\Omega_{\text{matter}} \neq 1$ models. In both cases the gravitational potential decays with time, which leads to an enhancement of anisotropies on large angular scales. Finally we have the terms caused by photon polarization and anisotropic stress, which contribute to Π. These terms affect the anisotropy spectra at the 10% level and are important for accurate model predictions. Moreover, they are the sources for photon polarization.

The main advantage of (3.38) is that it decomposes the anisotropy into a source

term $S_{T,P}^S$, which does not depend on the multipole moment l and a geometrical term j_l, which does not depend on the particular cosmological model. The latter only needs to be computed once and can be stored for subsequent calculations. The source term is the same for all multipole moments and only depends on a small number of contributors in (3.38) (gravitational potentials, baryon velocity and photon moments up to $l = 2$). By specifying the source term as a function of time one can compute the corresponding spectrum of anisotropies. Equation (3.38) is formally an integral system of equations, because the first moments appear on both sides of equations. To solve for these moments it is best to use the equations in their differential form (3.23), instead of the integral form above. Once the moments that enter into the source function are computed, one can solve for the higher moments by performing the integration in (3.38).

The solution for the tensor modes can similarly be written as an integral over the source term,

$$
\begin{aligned}
\Delta_{\tilde{T}l}^T &= \sqrt{\frac{(l+2)!}{(l-2)!}} \int_0^{\tau_0} d\tau \, \frac{1}{2}[h_t + 3\Pi] \, \frac{j_l(x)}{x^2} \\
\Delta_{\tilde{E}l}^T &= \int_0^{\tau_0} d\tau \, \frac{3}{2}\Pi \left[-j_l(x) + j_l''(x) + \frac{2j_l(x)}{x^2} + \frac{4j_l'(x)}{x} \right] \\
\Delta_{\tilde{B}l}^T &= \int_0^{\tau_0} d\tau \, \frac{3}{2}\Pi \left[2j_l'(x) + \frac{4j_l}{x} \right] \\
x &= k(\tau_0 - \tau)
\end{aligned}
\tag{3.40}
$$

Equations (3.38) and (3.40) are the main equations of this chapter and form the basis of the line of sight integration method of computing CMB anisotropies. The treatment can be generalized to arbitrary FRW backgrounds [7]. In the next section we will discuss in more detail the computational advantages of this formulation of the Boltzmann equation and its implementation.

3.4   Calculational Techniques

In the previous section we presented the expressions needed for the implementation of the line of sight integration method. As shown in equations (3.38) and (3.40) one needs to integrate over time the source term at time τ multiplied with the sperical Bessel function evaluated at $x = k(\tau_0 - \tau)$. The latter does not depend on the model and can be precomputed in advance. Fast algorithms exist which can compute spherical Bessel functions on a grid in x and l in short amount of time (e.g. [16]). The grid is then stored on a disk and used for all the subsequent calculations. This leaves us with the task of accurately calculating the source term, which determines the CMB spectrum for a given model. Below we discuss some of the calculational techniques needed for the implementation of the method. We especially highlight the differences between this approach and the standard Boltzmann integration approach. Our goal is to develop a method which is accurate to 1% in C_l up to $l \sim 1000$ over the whole range of cosmological parameters of interest. These include models with varying amount of dark matter, baryonic matter, Hubble constant, vacuum energy, neutrino mass, shape of initial spectrum of perturbations, reionization and tensor modes. The choice of accuracy is based on estimates of observational accuracies that will be achievable in the next generation of experiments and also on the theoretical limitations of model predictions (e.g. cosmic variance, second order effects, etc.). Most of the figures where we discuss the choice of parameters are calculated for the standard CDM model. This model is a reasonable choice in the sense that it is a model which exhibits most of the physical effects in realistic models, including acoustic oscillations, early-time integrated Sachs-Wolfe effect and Silk damping. One has to be careful however not to tune the parameters based on a single model. We compared our results with results from other groups [17, 18] for a number of different models. We find a better than 1% agreement with these calculations over most of the parameter space of models. The computational parameters we recommend below are based on this more detailed comparison and are typically more stringent than what one would find based on the comparison with the standard CDM model only.

3.4.1 Number of coupled differential equations

In the standard Boltzmann method the photon distribution function is expanded to a high $l_{\max}$ (3.23) and typically one has to solve a coupled system of several thousand differential equations. In the integral method one evaluates the source terms $S(k, \tau)$ as a function of time (equations 3.38 and 3.40) and one only requires the knowledge of photon multipole moments up to $l = 2$, plus the metric perturbations and baryon velocity. This greatly reduces the number of coupled differential equations that are needed to be solved. For an accurate evaluation of the lowest multipoles in the integral method one has to extend the hierarchy somewhat beyond $l = 2$, because the lower multipole moments are coupled to the higher multipoles (3.23). Because power is only being transferred from lower to higher l it suffices to keep a few moments to achieve a high numerical accuracy of the first few moments. One has to be careful however to avoid unwanted reflections of the power being transferred from low l to high l, which occur for example if a simple cut-off in the hierarchy is imposed. This can be achieved by modifying the boundary condition for the last term in the hierarchy using the free streaming approximation [12, 19]. In the absence of scattering (the so-called free streaming regime), the recurrence relation among the photon multipoles in equation (3.23) becomes the generator of spherical Bessel functions. One can therefore use a different recurrence relation among the spherical Bessel functions to approximate the last term in the hierarchy without reference to the higher terms. The same approximation can also be used for polarization and neutrino hierarchies. This type of closure scheme works extremely well and only a few multipoles beyond $l = 2$ are needed for an accurate calculation of the source term. This is shown in Figure 3-1, where a relative error in the spectrum is plotted for several choices of maximal number of photon multipoles. We choose to end the photon hierarchy (both anisotropy and polarization) at $l_\gamma = 8$ and massless neutrino at $l_\nu = 7$, which results in an error lower than 0.1% compared to the exact case. Instead of a few thousand coupled differential equations we therefore evolve about 35 equations and the integration time is correspondingly reduced.
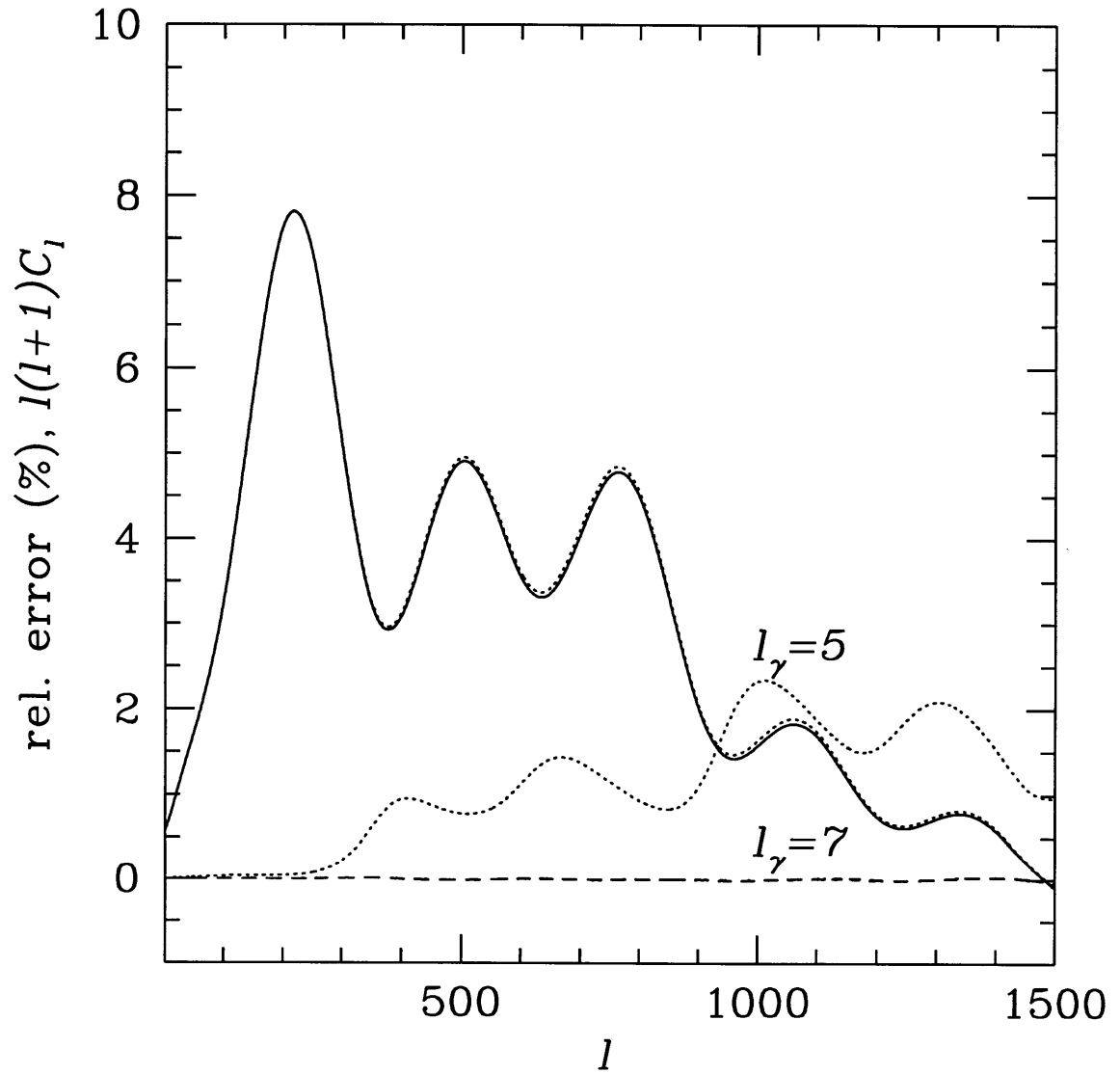
Figure 3-1: CMB spectra produced by varying the number of evolved photon multipole moments, together with the relative error (in %) compared to the exact case. While using $l_\gamma = 5$ produces up to 2% error, using $l_\gamma = 7$ gives results almost identical to the exact case.

3.4.2   Sampling of CMB multipoles

In the standard Boltzmann integration method one solves for the whole photon hierarchy (3.23) and the resultant Δ_l is automatically obtained for each l up to some l_{max}. The CMB spectra are however very smooth (see Figure 3-1), except for the lowest l where the discrete nature of the spectrum becomes important. This means that the spectrum need not be sampled for each l and instead it suffices to sparsely sample the spectrum in a number of points and interpolate between them. Figure 3-2 shows the result of such interpolation with cubic splines (see e.g. [16]) when every 20th, 50th or 70th l is sampled beyond $l = 100$ with an increasingly denser sampling towards small l, so that each l is sampled below $l = 10$. While sampling of every 70th l results in maximal error of 1%, sampling in every 20th or 50th l gives errors below 0.2 and 0.4%, respectively. We choose to compute every 50th C_l beyond $l = 100$ in addition to 15 l modes below $l = 100$, so that a total of 45 l modes are calculated up to $l_{max} = 1500$. This gives a typical (rms) error of 0.1%, with excursions of up to 0.4%. The number of integrals in equation (3.25) is thus reduced by a factor of 50 at high l and the computational time needed for the integrals becomes comparable to or smaller than the time needed to solve for the system of differential equations.

3.4.3   Integration over time

For each Fourier mode k the source term is integrated over time τ (equation 3.38). The sampling in time need not be uniform, because the dominant contribution arises from the epoch of recombination around $z \sim 1100$, the width of which is determined by the visibility function g and is rather narrow in look-back time for standard recombination scenarios. During this epoch the sources acoustically oscillate on a time scale of $c_s k^{-1}$, so that the longest wavelength modes are the slowest to vary. For short wavelengths the rate of sampling should therefore be higher. Even for long wavelengths the source function should still be sampled in several points across the last-scattering surface. This is because the terms in (3.38) depend on the derivatives of the visibility function. If the visibility function g is narrow then its derivative will also be narrow and will
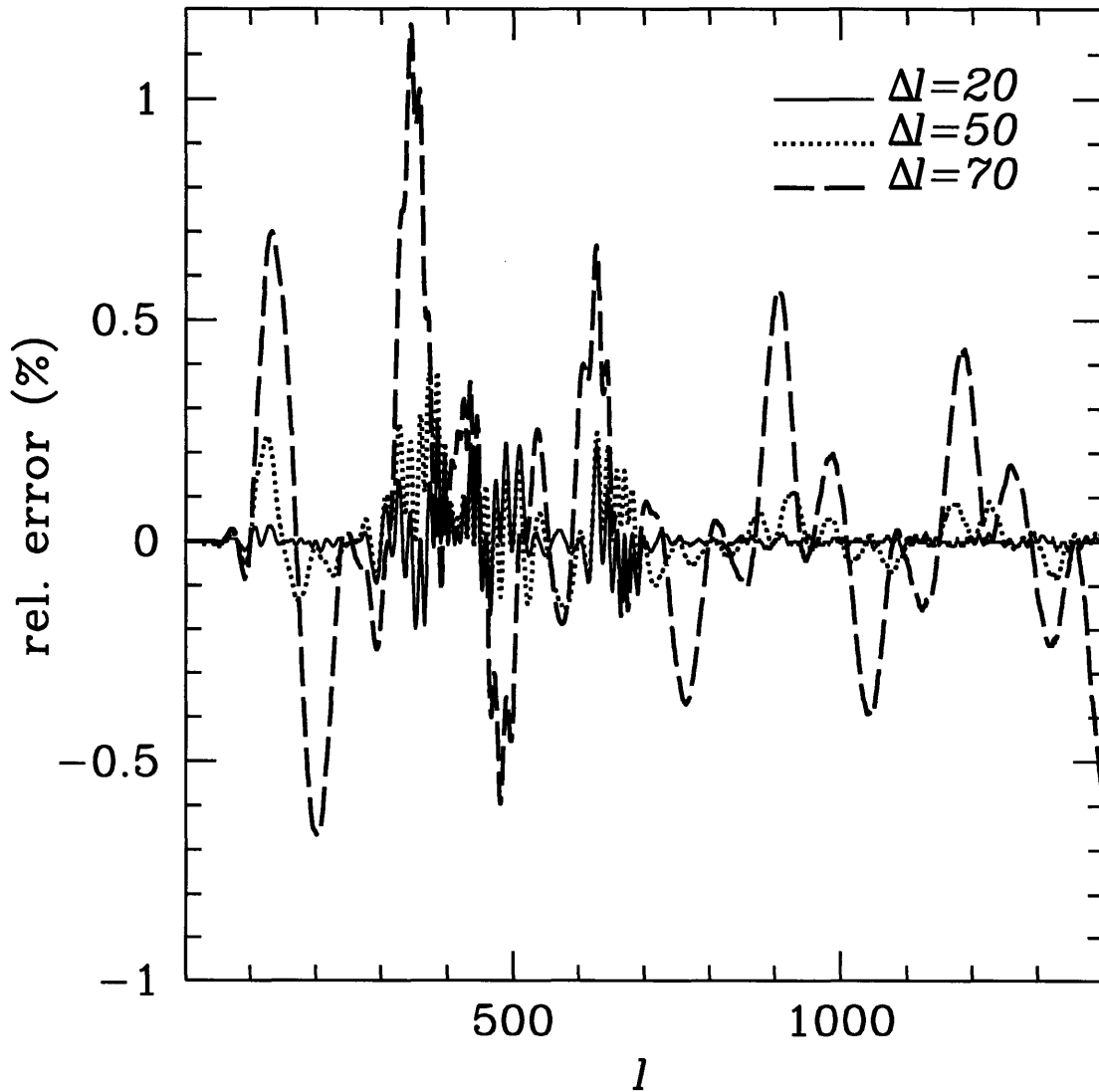
Figure 3-2: Relative error between the exact and interpolated spectrum, where every 20th, 50th or 70th multipole is calculated. The maximal error for the three approximations is less than 0.2, 0.4 and 1.2%, respectively. The rms deviation from the exact spectrum is further improved by finer sampling, because the interpolated spectra are exact in the sampled points. For the sampling in every 50th multipole the rms error is 0.1%.

sharply change sign at the peak of g. Its integration will lead to numerical roundoff errors if not properly sampled, even though positive and negative contributions nearly cancel out when integrated over time and make only a small contribution to the integral. Figure 3-3 shows the error in integration caused by sampling this epoch with 10, 20 or 40 points. Based on comparison with several models we choose to sample the recombination epoch with 40 points, which results in very small ($\sim 0.1\%$) errors. After this epoch the main contribution to the anisotropies arises from the integrated Sachs-Wolfe term. This is typically a slowly changing function and it is sufficient to sample the entire range in time until the present in 40 points. The exceptions here are models with reionization, where the visibility function becomes non-negligible again and a new last-scattering surface is created. In this case a more accurate sampling of the source is also needed at lower redshifts.

3.4.4 Integration over wavenumbers

The main computational cost of standard CMB calculations is solving the coupled system of differential equations. The number of k-modes for which the system is solved is the main factor that determines the speed of the method. For results accurate to $l_{\max}$ one has to sample the wavenumbers up to a maximum value $k_{\max} = l_{\max}/\tau_0$. In the line of sight integration method solving the coupled system of differential equations still dominates the computational time (although for each mode the time is significantly shorter than in the standard Boltzmann method because of a smaller system of equations). It is therefore instructive to compare the number of k evaluations needed in each of the methods to achieve a given accuracy in the final spectrum.

In the standard Boltzmann method one solves for $\Delta^S_{T,l}(k)$ directly, so this quantity must be sampled densely enough for accurate integration. Figure 3-4a shows $\Delta^S_{T,l}(k)$ for $l = 150$ in a standard CDM model. One can see that it is a rapidly oscillating function with a frequency $k \sim \tau_0^{-1}$. Each oscillation needs to be sampled in at least a few points to assure an accurate integration. To obtain a smooth CMB spectrum one typically requires 6 points over one period, implying $2l_{\max}$ k-mode evaluations. This number can be reduced somewhat by filtering out the sampling noise in the spectrum
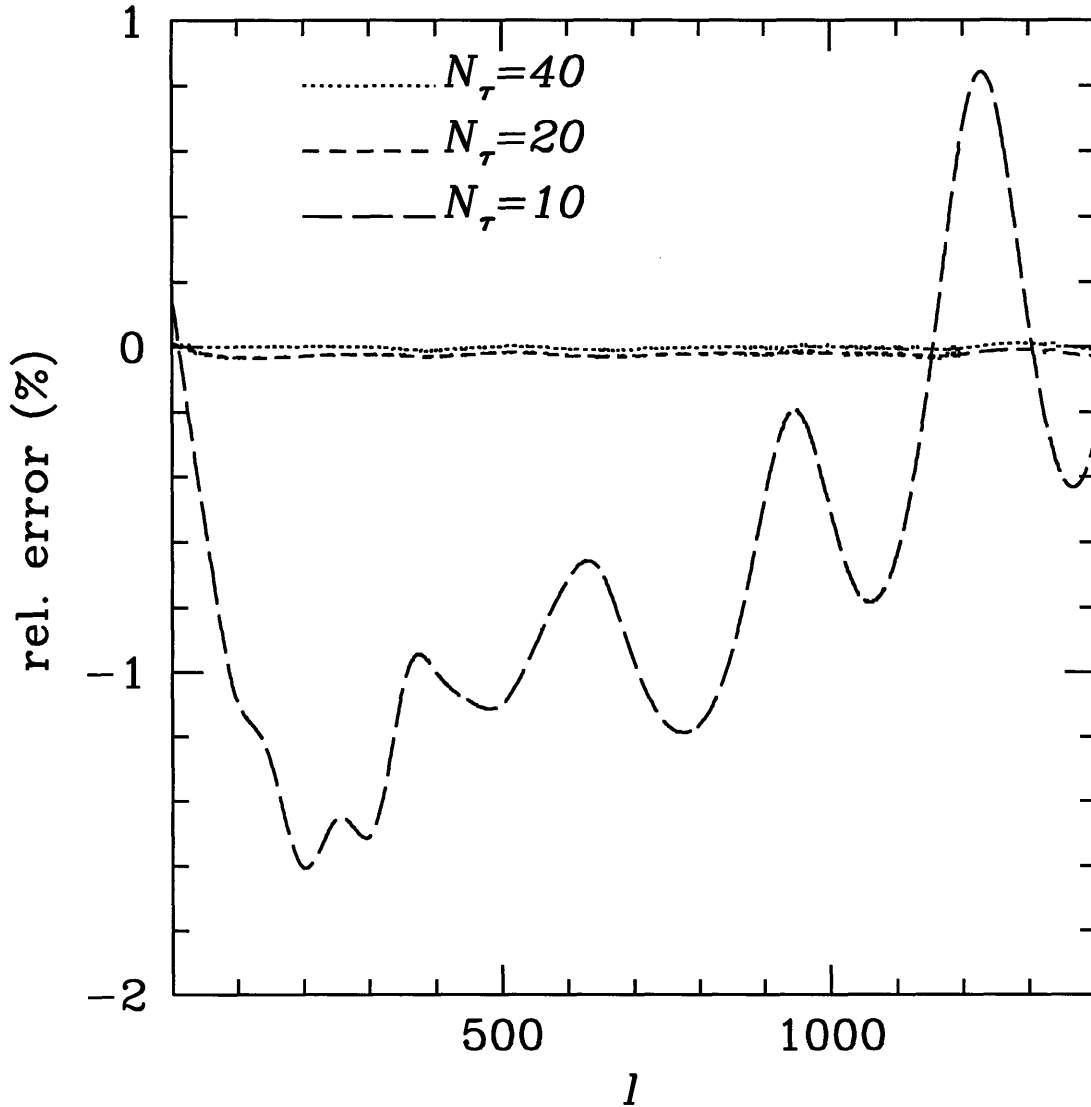
Figure 3-3: Error in the spectrum caused by insufficient temporal sampling of the source term. Inaccurate sampling of the source during recombination leads to numerical errors, which can reach the level of 1% if the source is sampled in only 10 points across the recombination epoch. Finer sampling in time gives much smaller errors for this model. Comparisons with other models indicate that sampling in 40 points is needed for accurate integration.
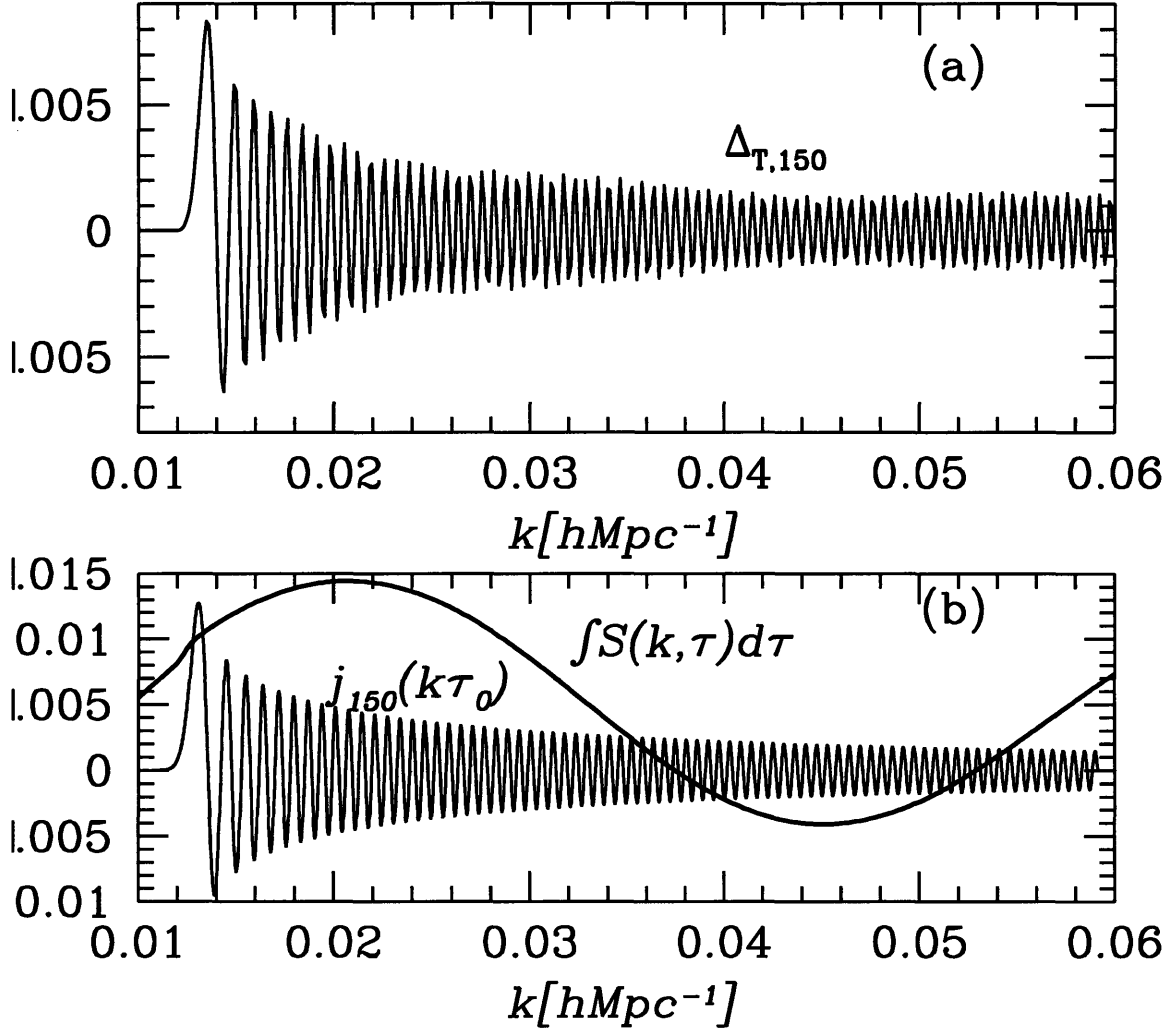
Figure 3-4: In (a) $\Delta^S_{T,150}(k)$ is plotted as a function of wavevector k. In (b) $\Delta^S_{T,150}(k)$ is decomposed into the source term S^S_T integrated over time and the spherical Bessel function $j_{150}(k\tau_0)$. The high frequency oscillations of $\Delta^S_{T,150}(k)$ are caused by oscillations of the spherical Bessel function $j_{150}(k\tau_0)$, whereas the source term varies much more slowly. This allows one to reduce the number of k evaluations in the line of sight integration method, because only the source term needs to be sampled.

[19], but even in this case one requires at least 1-2 points per each period or $l_{max}/2$ k-mode evaluations.

To understand the nature of these rapid oscillations in $\Delta_{T,l}^S(k)$ we will consider wavelengths larger than the width of the last scattering surface. In this case the Bessel function in (3.38) can be pulled out of the integral as $j_l(k\tau_0)$ because the time at which recombination occurs, when the dominant contribution to $\Delta_{T,l}^S(k)$ is created, is much smaller than τ_0 and $k\Delta\tau \ll 1$ ($\Delta\tau$ is the interval of time for which the visibility function differs appreciably from zero). So the final $\Delta_{T,l}^S(k)$ is approximately the product of $j_l(k\tau_0)$ and S_T^S integrated over time, if the finite width of the last scattering surface and contributions after recombination can be ignored.

Figure 3-4b shows the source term S_T^S integrated over time and the Bessel function $j_l(k\tau_0)$. It shows that the high frequency oscillations in $\Delta_{T,l}^S(k)$ seen in Figure 3-4a are caused by the oscillation of the spherical Bessel functions, while the oscillations of the source term have a much longer period in k. The different periods of the two oscillations can be understood using the tight coupling approximation [19, 20]. Prior and during recombination photons are coupled to the baryons and the two oscillate together with a typical acoustic timescale $\tau_s \sim \tau_{rec}/\sqrt{3} \sim \tau_0/\sqrt{3z_{rec}} \sim \tau_0/50$. The frequency of acoustic oscillations $k \sim \tau_{rec}^{-1}$ is therefore 50 times higher than the frequency of oscillations in spherical Bessel functions, which oscillate as τ_0^{-1}.

Because an accurate sampling of the source term requires only a few points over each acoustic oscillation, the total number of k evaluations in the integral method can be significantly reduced compared to the standard methods. Typically a few dozen evaluations are needed over the entire range of k, compared to about 500 evaluations in the standard method when a noise filtering technique is used and 2000 otherwise (for $l_{max} \sim 1000$). Once the source term is evaluated at these points one can interpolate it at points with preevaluated spherical Bessel functions, which can be much more densely sampled at no additional computational cost. The end result is the same accuracy as in the standard method, provided that the source is sampled in sufficient number of points. Figure 3-5 shows the relative error in the CMB spectrum for the cases where the source term is calculated in 40, 60 and 80 points between 0

and $k\tau_0 = 3000$ (for $l_{max} = 1500$). While using 40 points results in up to 1% errors, using 60 points decreases the maximum error to below 0.2% for this model. In general it suffices to use $l_{max}/30$ k modes, which is at least an order of magnitude smaller than in the standard methods. Note that with this method there is no need to filter the spectrum to reduce the sampling noise, because the latter is mainly caused by insufficient sampling of the spherical Bessel functions, which are easy to precompute. The additional operations needed for a higher sampling (summation and source interpolation) do not significantly affect the overall computational time. Moreover, if each C_l is accurately calculated they can be sparsely sampled and interpolated (section 3.2). This would not be possible if they had a significant noise component added to them.

3.5 Summary

In this chapter we presented a new method for accurate calculations of CMB anisotropy and polarization spectra. The method is not based on any approximations and is an alternative to the standard Boltzmann calculations, which are based on solving large numbers of differential equations. The approach proposed here uses a hybrid integro-differential approach in solving the same system of equations. By rewriting the Boltzmann equations in the integral form the solution for the photon anisotropy spectrum can be written as an integral over a source and a geometrical term. The first is determined by a small number of contributors to the photon equations of motion and the second is given by the radial eigenfunctions, which do not depend on the particular cosmological model, but only on the geometry of space.

One advantage of the split between geometrical and dynamical terms is that it clarifies their different contributions to the final spectrum. A good example of this is the temperature anisotropy in the non-flat universe, which can be be written using a similar decomposition, except that spherical Bessel functions have to be replaced with their appropriate generalization [15]. This is discussed in more detail elsewhere [7]. Here we simply remark that replacing radial eigenfunctions in a non-flat space

91
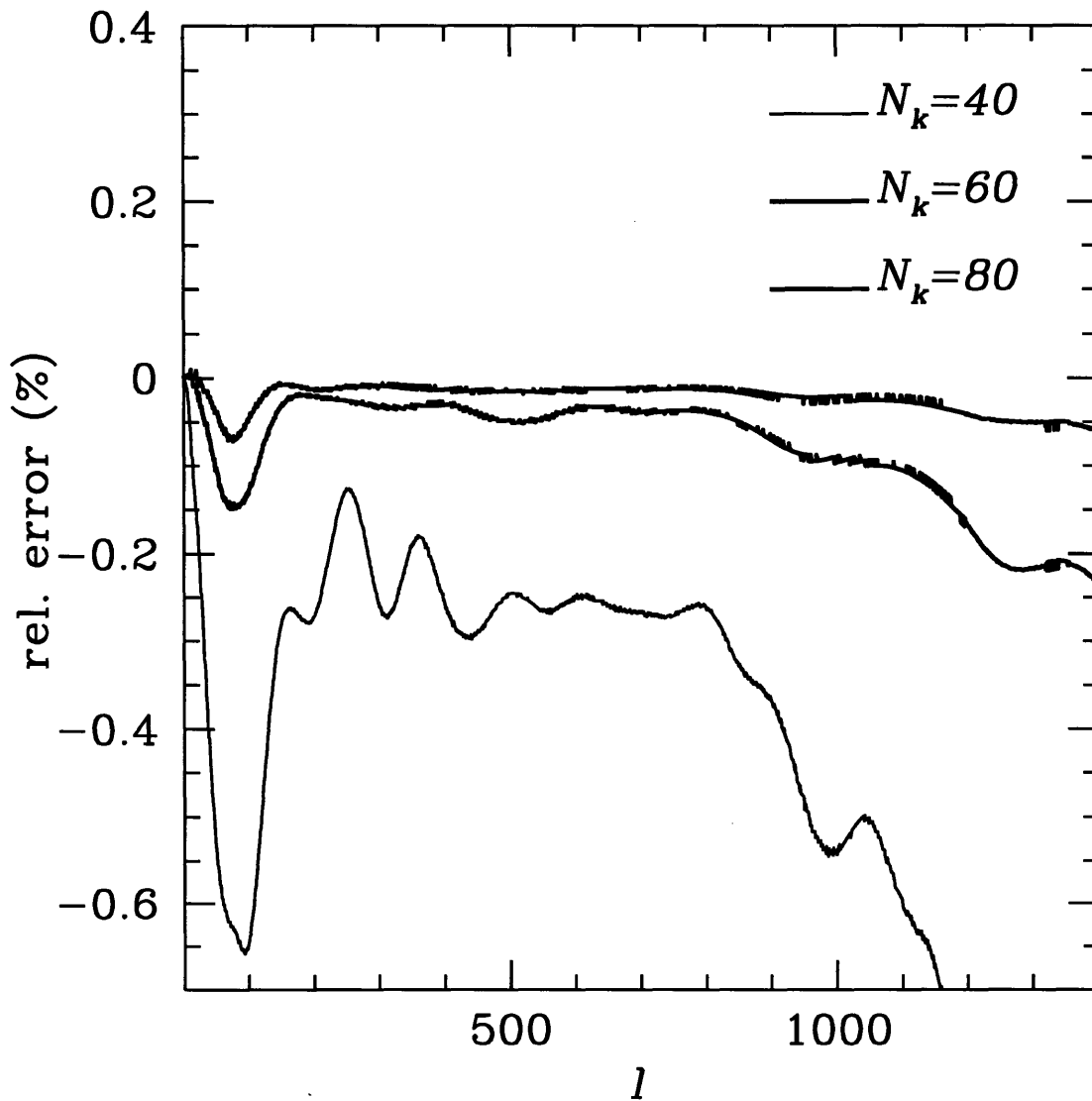
Figure 3-5: Error in the spectrum caused by insufficient k-mode sampling of the source term. Sampling the source with 40 points up to $k = 2l_{max}$ leads to 1% errors, while with 60 or 80 points the maximal error decreases to 0.2%. Comparisons with other models indicate that sampling in 60 points is sufficient for accurate integration.

with their flat space counterpart (keeping comoving angular distance to the LSS unchanged) is only approximate and does not become exact even in the large l (small angle) limit. The geometry of the universe leaves its signature in the CMB spectra in a rather nontrivial way and does not lead only to a simple rescaling of the spectrum by $\Omega_{\text{matter}}^{-1/2}$ [3].

The main advantage of our line of sight integration method is its speed and accuracy. For a given set of parameters it is two orders of magnitude faster than the standard Boltzmann methods, while preserving the same accuracy. We compared our results with the results by Sugiyama [18] and by Bode & Bertschinger [17]. In both cases the agreement was better than 1% up to a very high l for all of the models we compared to.

The method is useful for fast and accurate normalizations of density power spectra from CMB measurements, which for a given model require the CMB anisotropy spectrum and matter transfer function, both of which are provided by the output of the method. Speed and accuracy are even more important for accurate determination of cosmological parameters from CMB measurements. In such applications one wants to perform a search over a large parameter space, which typically requires calculating the spectra of a several thousand models (e.g. [3]). One feasible way to do so is to use approximation methods mentioned in the introduction. These can be made extremely fast, but at a cost of sacrificing the accuracy. While several percent accuracy is sufficient for analyzing the present day experiments, it will not satisfy the requirements for the future all-sky surveys of microwave sky. Provided that foreground contributions can be succesfully filtered out one can hope for accuracies on the spectrum close to the cosmic variance limit, which for a broad band averages can indeed reach below 1% at $l > 100$. It is at this stage that fast and accurate CMB calculations such as the one presented in this chapter will become crucial and might enable one to determine many cosmological parameters with an unprecedented accuracy.

Bibliography

[1] D. Scott, J. Silk & M. White, Science **268**, 829 (1995).

[2] J.R Bond, in "Cosmology and Large Scale Structure", ed. R. Schaeffer et. al., (Elsevier Science, Netherlands) (1996).

[3] G. Jungman, M. Kamionkowski, A. Kosowsky & D. N. Spergel, Phys. Rev. Lett. **76**, 1007 (1996).

[4] J. R. Bond, G. Efstathiou & M. Tegmark, Mon. Not. R. Astron. Soc. **291**, 33 (1997).

[5] M. Zaldarriaga, D. N. Spergel & U. Seljak, Astrophys. J. **488**, 1 (1997).

[6] E. Bertschinger, in "Cosmology and Large Scale Structure", ed. R Schaffer et. al. (Elsevier Science, Netherlands) (1996).

[7] M. Zaldarriaga, U. Seljak & E. Bertschinger, Astrophys. J. **494**, 491 (1998).

[8] W. Hu, U. Seljak, M. White & M. Zaldarriaga, Phys. Rev. D **57**, 3290 (1998).

[9] E. M. Lifshitz, J. Phys. USSR, **10** , 16, (1946).

[10] J. M. Bardeen Phys. Rev. D **22**, 1882 (1980).

[11] J. N. Goldberg et al., J. Math. Phys. **8**, 2155 (1967).

[12] C. P. Ma & E. Bertschinger Astrophys. J. **455**, 7 (1995).

[13] M. Zaldarriaga & U. Seljak, Phys. Rev. D **55**, 1830 (1997).

[14] M. Zaldarriaga & D. Harari, Phys. Rev. D **52**, 3276 (1995).

[15] L. F. Abbott & R. K. Schaefer, Astrophys. J. **308**, 546 (1986).

[16] W. H. Press, S. A. Teukolsky, W. T. Vetterling & B. P. Flannery, Numerical Recipes in Fortran, 2nd ed. (New York: Cambridge University Press) (1992).

[17] P. Bode & E. Bertschinger, Proc. 1995 ACM/IEEE Supercomputing Conference (http://www.supercom.org/SC95/proceedings/) (1995).

[18] N. Sugiyama, Astrophys. J. S. **100**, 281 (1995).

[19] W. Hu, D. Scott, N. Sugiayma & M. White, Phys.Rev.D **52**, 5498 (1995).

[20] U. Seljak, Astrophys. J. **435**, L87 (1994).

Chapter 4

Information in the CMB Polarization[1]

4.1 Introduction

It is now well established that temperature anisotropies in CMB offer one of the best probes of early universe, which could potentially lead to a precise determination of a large number of cosmological parameters [1, 2, 3]. The main advantage of CMB versus more local probes of large-scale structure is that the fluctuations were created at an epoch when the universe was still in a linear regime. While this fact has long been emphasized for temperature anisotropies, the same holds also for polarization in CMB and as such it offers the same advantages as the temperature anisotropies in the determination of cosmological parameters. The main limitation of polarization is that it is predicted to be small: theoretical calculations show that CMB will be polarized at the 5-10% level on small angular scales and much less than that on large angular scales [4]. However, future CMB satellite missions (MAP and Planck) will be so sensitive that even such small signals will be measurable. Even if polarization by itself cannot compete with the temperature anisotropies, a combination of the two could result in a much more accurate determination of certain cosmological parameters,

---

[1]Based on M. Zaldarriaga, Phys. Rev. D **55**, 1822 (1997), U. Seljak & M. Zaldarriaga, Phys. Rev. Lett. **78**, 2054 (1997) and D. N. Spergel & M. Zaldarriaga, Phys. Rev. Lett. **79**, 2180 (1997).

in particular those that are limited by a finite number of multipoles in the sky (i.e. cosmic variance).

4.2 The Imprint of an Early Reionization of the Universe

It has been pointed out that an early reionization of the universe will greatly enhance polarization [5]. The fact that in universes that never recombined the polarization would also be large was noted in many of the above studies. More recently Ng & Ng [6] discussed the polarization generated in reionized universes with instantaneous recombination. The Sachs-Wolfe effect was the only source of anisotropies that they included. They concluded that reionization at a moderate redshift could boost polarization to the level of a few percent of the temperature perturbations. To make detailed predictions for an experiments (such as that being built at Wisconsin University) a realistic recombination history should be used since polarization is very sensitive to the duration of recombination [7, 8]. Baryons should also be included in the calculation as the acoustic oscillation in the photon-baryon plasma are very important to determine polarization.

In this section we discuss in detail the physics behind the polarization generated in models where there was an early reionization after the usual recombination. These models show very distinct features in the polarization power spectrum including a new peak at low l. This peak is not present either in the standard recombination scenarios or in the cases where the universe never recombined and it is the cause for the boost in the polarization.

4.2.1 Standard Ionization History

In this section we review previous results for the CMB polarization for a standard ionization history in a flat space-time. The Boltzmann equations for the perturbations

in the scalar case are given by equations (3.18) and (3.21),

$$\dot{\Delta}_T + ik\mu\Delta_T = -\frac{1}{6}\dot{h} - \frac{1}{3}(\dot{h} + 6\dot{\eta}) + \dot{\kappa}\left[-\Delta_T + \Delta_{T0} + i\mu v_b + \frac{1}{2}P_2(\mu)\Pi\right]$$

$$\dot{\Delta}_P + ik\mu\Delta_P = \dot{\kappa}\left[-\Delta_P + \frac{1}{4}P_2^2(\mu)\Pi\right] \tag{4.1}$$

They can be formally integrated to give (3.36),

$$\Delta_T(k,\tau_0) = \int_0^{\tau_0} d\tau e^{ik\mu(\tau-\tau_0)}e^{-\kappa}\{\dot{\kappa}e^{-\kappa}[\Delta_{T0} + i\mu v_b + \frac{1}{2}P_2(\mu)\Pi]$$

$$- \frac{1}{6}\dot{h} - \frac{1}{3}(\dot{h} + 6\dot{\eta})P_2(\mu)\}$$

$$\Delta_P(k,\tau_0) = \frac{1}{4}\int_0^{\tau_0} d\tau e^{ik\mu(\tau-\tau_0)}e^{-\kappa}\dot{\kappa}\Pi P_2^2(\mu). \tag{4.2}$$

Figure 4-1 shows the temperature and polarization C_l spectra for the standard CDM model ($\Omega_0 = 1$, $H_0 = 50\,\mathrm{km\,sec^{-1}}$ and $\Omega_b = 0.05$), normalizing the result to the COBE measurement. Normalization was carried out using the fits to the shape and amplitude of the 4 year COBE data described in [9], which approximately fixes $C_{T10} \sim 47\mu K^2$. In Sections 2.2.2 and 2.3 we discussed an approximate solution for wavelengths longer than the width of the last scattering surface, $\Delta\tau_D$ (equation 2.44). We showed that the polarization perturbation is [7],

$$\Delta_P = 0.51(1 - \mu^2)e^{ik\mu(\tau_D-\tau_0)}k\Delta\tau_D\Delta_{T1}(\tau_D) \tag{4.3}$$

where τ_D is the conformal time of decoupling. Note that in the tight coupling regime [2] $\Delta_{T1} \propto v_b$. The polarization is proportional to the velocity difference between places separated by a distance $\Delta\tau_D$, the distance photons travel on average during decoupling. For the standard adiabatic initial conditions Δ_{T1} and the baryon velocity vanish as $k\tau \to 0$ which together with the $k\Delta\tau_D$ factor in the previous expression explains the dramatic decrease of polarization with decreasing l. For large wavelengths the quadrupole generated in the photon distribution as photons travel between their last scatterings is extremely small both due to the small distance they can travel

---

[2] This velocity is in the longitudinal gauge, $v_b^{conf} = v_b^{synch} + k\dot{\alpha}$.
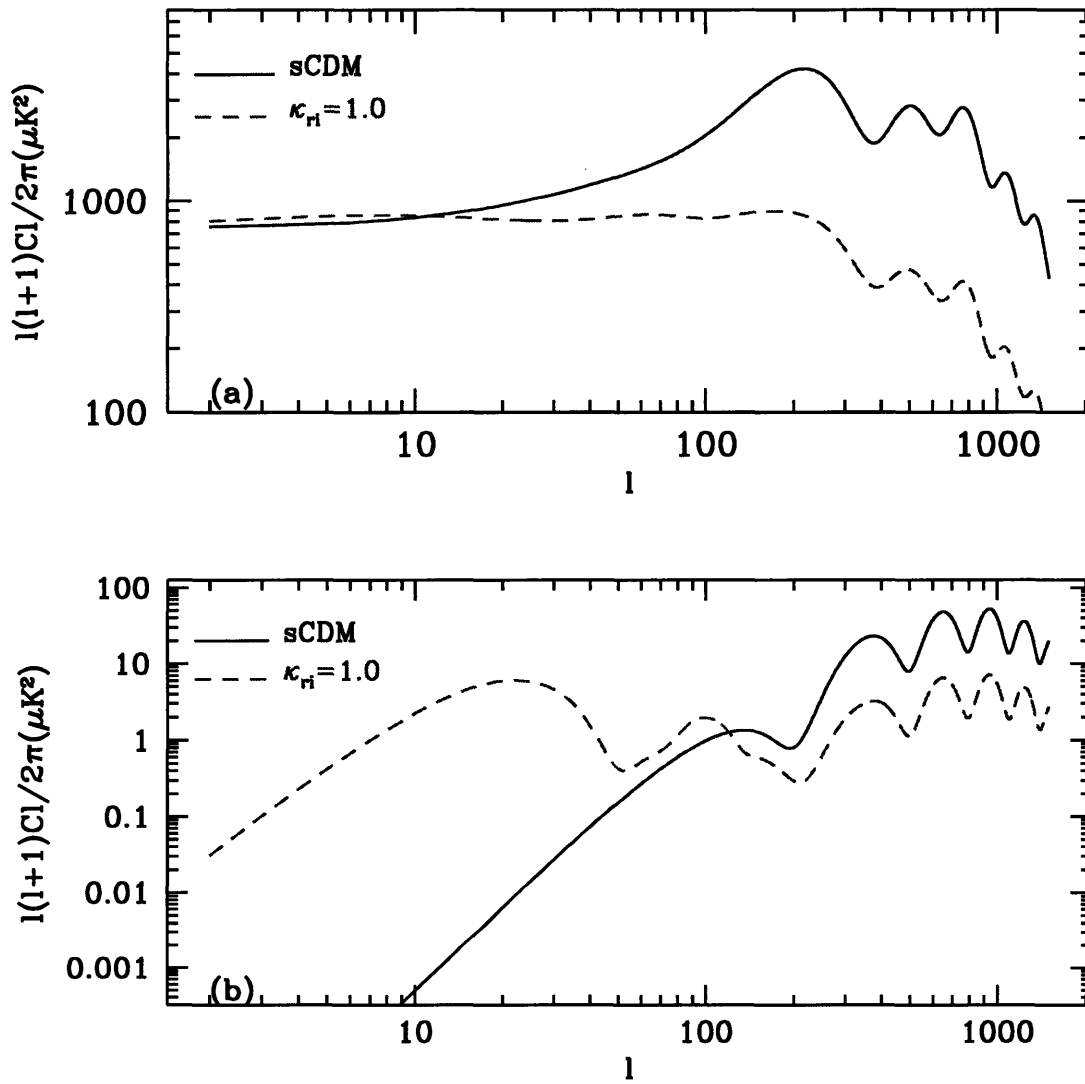
Figure 4-1: $l(l+1)C_l/2\pi$ for both temperature (a) and polarization (b) for standard CDM and a model where the optical depth to recombination is $\kappa_{ri} = 1.0$.

compared to the wavelength as well as to the small velocity differences generated by these small k perturbations.

4.2.2 The Reionized Case

In this section we consider models with early reionization and try to explain the origin of the new features that appear in the polarization power spectrum. For definiteveness we use a standard CDM model with specified optical depth to recombination κ_{ri}. For example if reionization occurred at a redshift of around $z_{ri} \sim 100$ then $\kappa_{ri} = 1.0$, assuming that all hydrogen atoms are ionized up to the present epoch ($x_e = 1.0$). Figure 4.2.2 shows the visibility function, $g(\tau) = \dot{\kappa} \exp(-\kappa)$, for $\kappa_{ri} = 1.0$. The visibility function has a very simple interpretation: the probability that a photon reaching the observer last scattered between τ and $\tau + d\tau$ is $g(\tau)d\tau$. The first peak in Figure 4.2.2, occurring at $\tau \approx 120$ Mpc for sCDM ($h = 0.5$) accounts for the photons that last scattered at recombination. The area under this peak, the probability that a photon came directly to us from this epoch, is $\exp(-\kappa_{ri})$. The area under the second peak gives the probability that a photon scattered after reionization and is equal to $1 - \exp(-\kappa_{ri})$.

Figure 4-1 shows the result of numerically integrating the Boltzmann equations for this reionized case. On small angular scales, the polarization acoustic peaks are suppressed, just like in the temperature case. This is very easy to understand: only a fraction $\exp(-\kappa_{ri})$ of the photons reaching the observer come from recombination, so their contribution to the C_l power spectrum is reduced by a factor $\exp(-2\kappa_{ri})$. On large scales new temperature anisotropies are created that compensate the reduction and leave the spectrum approximately the same. New peaks appear in the polarization power spectrum while the temperature anisotropy shows no new peaks. These new peaks in the polarization are what boost it and may make it detectable.

Let us try to understand the origin of these peaks. Before the decoupling of photons and electrons, for low values of k the largest perturbation in the photon distribution function is the monopole, Δ_{T0} because of the tight coupling between photons and electrons before recombination. Both the dipole and the quadrupole

100
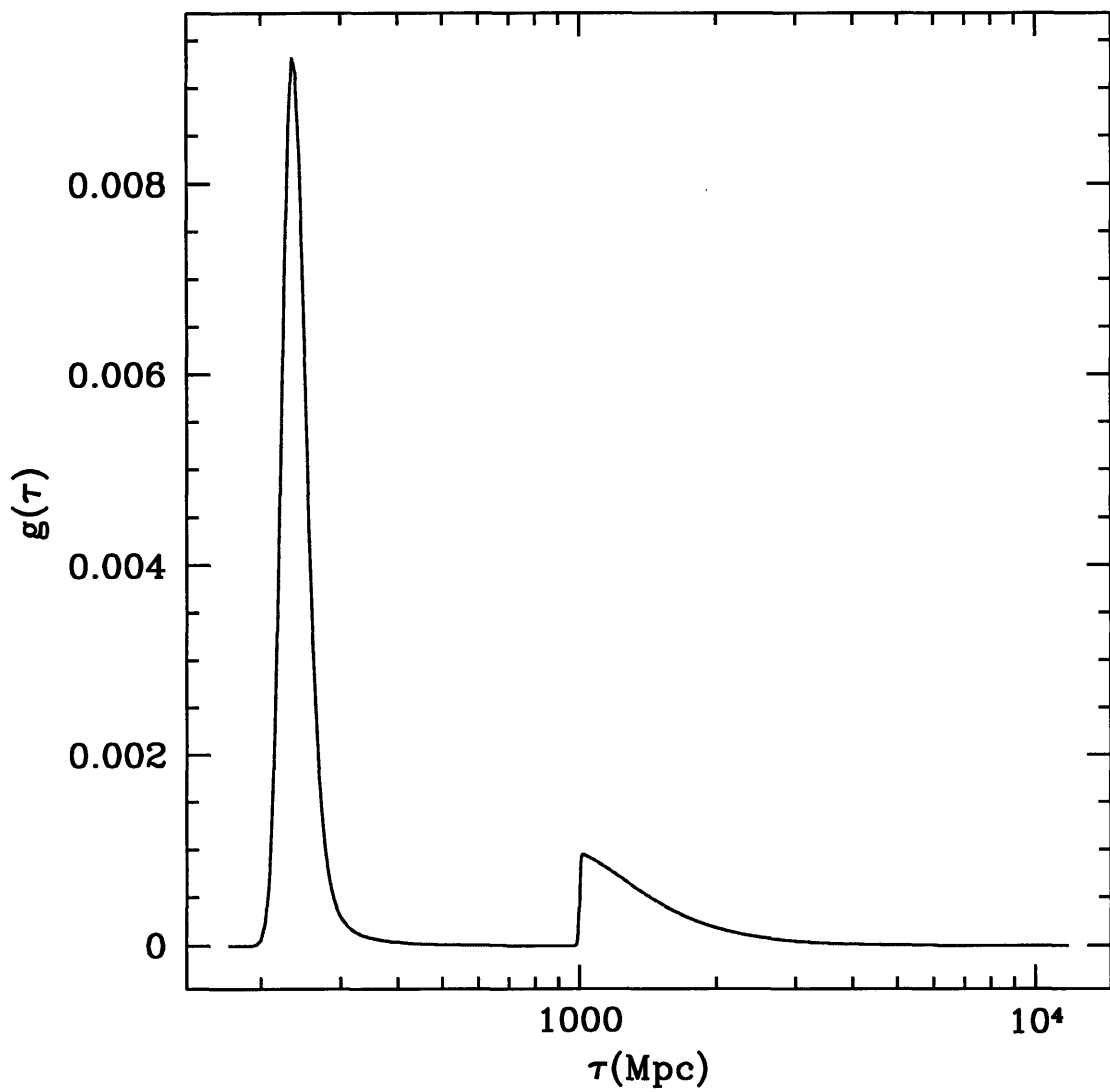
Figure 4-2: Visibility function for standard CDM with reionization such that the optical depth to recombination is $\kappa_{ri} = 1.0$.

as well as the polarization perturbations are much smaller. But after photons and electrons decouple, all the temperature multipoles can grow by free streaming. Power is being carried from the low multipole moments to higher ones. This is a geometrical effect. The temperature quadrupole is growing by free streaming after recombination and by the time the universe reionizes there is an appreciable quadrupole that can generate polarization. The structure of this quadrupole explains the new features in the polarization power spectrum.

The formal line of sight solution for the polarization perturbation is

$$\Delta_P = \frac{1}{4} \int_0^{\tau_0} d\tau\, e^{ik\mu(\tau-\tau_0)} e^{-\kappa} \dot\kappa \Pi P_2^2(\mu). \tag{4.4}$$

The visibility function has two peaks one at recombination and one at reionization. It is convenient to separate the previous integral in two parts,

$$\Delta_P = \frac{1}{4} P_2^2(\mu) \Big(\int_0^{\tau_{ri}} d\tau\, e^{ik\mu(\tau-\tau_0)} \dot\kappa e^{-\kappa} \Pi + \int_{\tau_{ri}}^{\tau_0} d\tau\, e^{ik\mu(\tau-\tau_0)} \dot\kappa e^{-\kappa} \Pi \Big) \tag{4.5}$$

where τ_{ri} is the conformal time of the start of reionization. The first integral represents the polarization generated at recombination and can easily be shown to be

$$\Delta_P^{(1)} \equiv \frac{1}{4} P_2^2(\mu) \int_0^{\tau_{ri}} d\tau\, e^{ik\mu(\tau-\tau_0)} \dot\kappa e^{-\kappa} \Pi = e^{-\kappa_{ri}} \Delta_P^{NR} \tag{4.6}$$

where Δ_P^{NR} is the polarization that would be measured if there was no reionization, as discussed in the previous section. This contribution is damped because only a fraction $\exp(-\kappa_{ri})$ of the photons that arrive to the observer came directly from recombination without scattering again after reionization.

Let us now consider the new contribution arising from reionization. The polarization source is $\Pi = \Delta_{T2} - 6(_{+2}\Delta_{P2} + {}_{-2}\Delta_{P2})$. The temperature quadrupole Δ_{T2} is large and originates in the free streaming of the monopole at recombination, while the polarization terms do not grow after decoupling and are thus negligible to first approximation. Equation (4.5) shows that the new polarization is basically an average of the value of the temperature quadrupole during reionization. This accounts

for all the new features in the polarization power spectrum of Figure 4-1.

To understand the origin of these new peaks let us find the amplitude of the temperature quadrupole at the time reionization starts τ_{ri}. The monopole at recombination is approximately given by [10]

$$(\Delta_{T0} + \dot{\alpha})(\tau_D) = \frac{1}{3}\psi(1 + 3R)\cos(kc_s\tau_D) - R\psi \qquad (4.7)$$

where ψ is a constant (the value of the conformal gauge gravitational potential), $R = 3\rho_b/4\rho_\gamma|_{\tau_D} \approx 30\Omega_b h^2$ and $c_s = 1/\sqrt{3(1 + R)}$ is the photon-baryon sound speed. The quadrupole at τ_{ri} arising from the free streaming of this monopole is simply (equation 3.38),

$$\Delta_{T2}(\tau_{ri}) = (\Delta_{T0} + \dot{\alpha})(\tau_D)j_2[k(\tau_{ri} - \tau_D)] \qquad (4.8)$$

where j_2 is the $l = 2$ spherical Bessel function.

The peaks of $\Delta_{T2}(\tau_{ri})$ as a function of k will show up in the polarization power spectrum. The first peak of equation (4.8) is approximately at the first peak of the Bessel function because $c_s\tau_D \ll (\tau_{ri} - \tau_D)$. The wavenumber for this first peak is approximately given by $k(\tau_{ri} - \tau_D) \sim 2$, translating into an l value as usual according to $l \sim k(\tau_0 - \tau_{ri})$. The physical size of the wavelength is translated to an angular size in the sky using the distance to reionization, $\tau_0 - \tau_{ri}$. In terms of multipoles, the first peak is at $l \sim k(\tau_0 - \tau_{ri}) \sim 2(\tau_0 - \tau_{ri})/(\tau_{ri} - \tau_D) \sim 2\sqrt{z_{ri}}$. For the case under consideration, $z \sim 100$ this means $l \sim 20$ which agrees very well with the the first peak in Figure 4-3. Only the first few peaks appear because the reionization scattering surface is wide and thus for smaller wavelengths the source in equation (4.5) oscillates during its width and cancels out after integration. This cancellation makes the new polarization small and thus hidden under the polarization generated at recombination.

The major factor determining the difference in height of these new peaks for different models is the fraction of photons reaching the observer that last scattered after reionization, $1 - \exp(-\kappa_{ri})$. The ratio of the distances between the observer and reionization to that between the two scattering surfaces determines the positions of
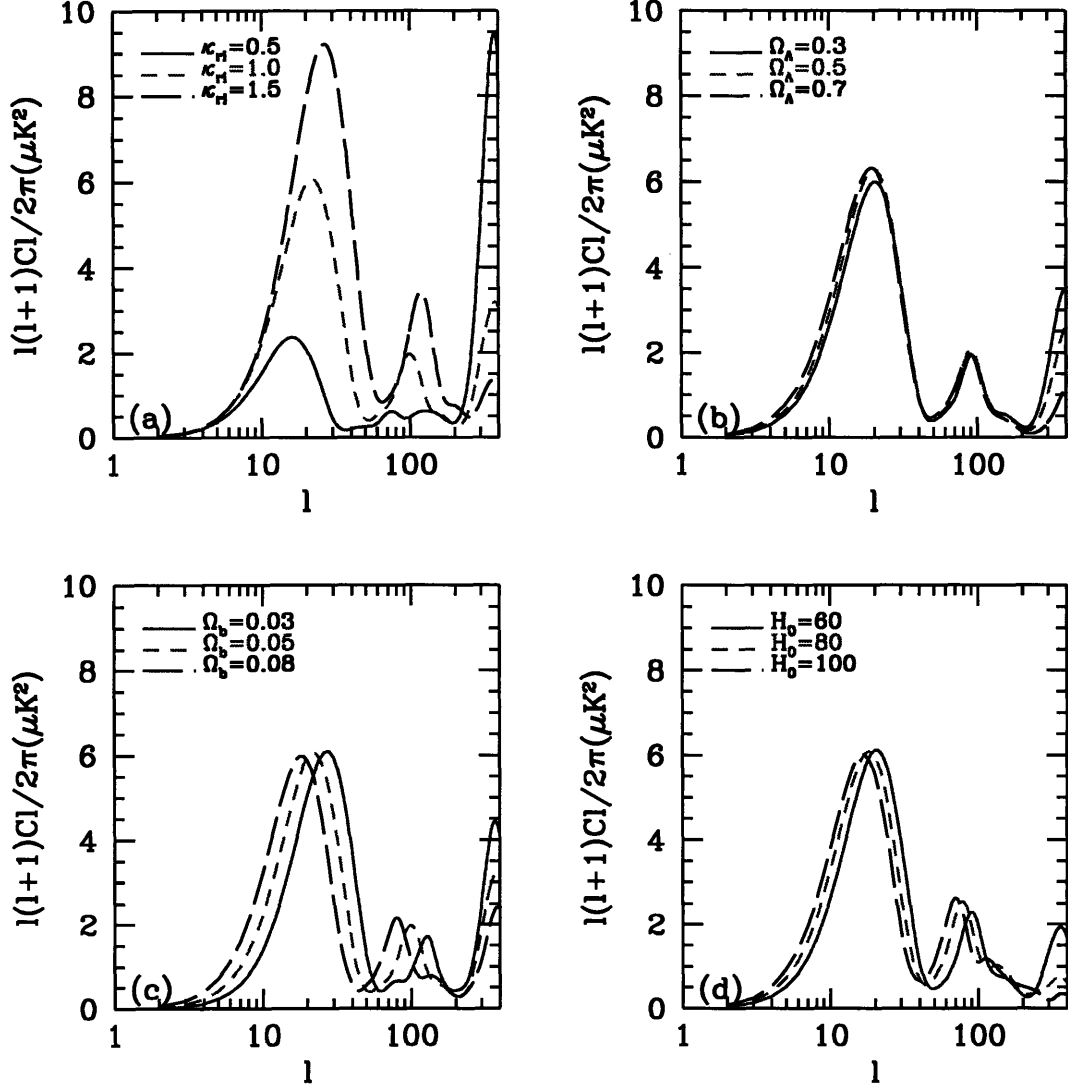
Figure 4-3: $l(l+1)C_{lP}/2\pi$ (a) for CDM models with varying $\kappa_{ri} = 0.5$, 1.0, 1.5 and (b) for models with varying cosmological constant $\Omega_\Lambda = 0.3$, 0.5, 0.7 and a fixed redshift of reionization $z_{ri} = 100$. Reionized ($\kappa_{ri} = 1.0$) CDM models (c) with varying $\Omega_b = 0.3$, 0.5, 0.8 and (d) with different Hubble constants $H_0 = 60$, 80, 100 km sec^{-1}Mpc^{-1}. In all cases reionization was assumed to be complete ($x_e = 1$)

the peaks, and the optical depth determines κ_{ri} their heights.

To further illustrate these points, Figure 4-3a shows the C_{El} spectrum for standard CDM models with varying optical depths κ_{ri}. The peaks not only vary in height but also in position, as the redshift of reionization increases when κ_{ri} does and so the position of the peaks gets moved to smaller scales, $l_{peak} \sim 2\sqrt{z_{ri}}$. Figure 4-3b on the other hand show how these peaks vary with the cosmological constant for a fixed reionization redshift $z_{ri} = 100$. The positions hardly change as both the distance to reionization and the distance between the two scattering surfaces scale approximately in the same way with the matter density (in this calculations the matter density is given by $\Omega_0 = 1 - \Omega_\Lambda$ where Ω_Λ is the energy density due to the cosmological constant). The distance to a fixed redshift increases with the cosmological constant, the optical depth κ_{ri} increases, and consequently the peaks should get higher. The fact that this is not the case is a consequence of the COBE normalization, because models with larger values of the cosmological constant have larger additional contributions to the low l temperature anisotropies from the ISW effect while polarization is not affected by the late time variation of the gravitational potential which does not affect the polarization. Thus the changes in the normalization to keep the value of C_{T10} fixed partially compensate the change in the height of the new polarization peaks produced by the larger optical depth.

Figures 3c and 3d explore the dependence of the polarization power spectrum with the baryon density and the Hubble constant for a fixed optical depth to decoupling, $\kappa_{ri} = 1.0$, keeping the rest of the parameters the same as sCDM. The height of the first peak in the spectrum remains nearly constant as it is determined by κ_{ri} which was kept fixed. The fact that the peaks move is due to the fact that the redshift of reionization is changing, it is given by $(1 + z_{ri}) \approx 100[\kappa_{ri}(0.5/h)(0.05/\Omega_b)(1/x_e)]^{2/3}$ and so l scales approximately as $l \propto (\kappa_{ri}/h\Omega_b x_e)^{1/3}$.

In the sCDM model the reionization must have occurred extremely early ($z_{ri} \approx 100$) in order to produce an optical depth of unity; even an optical depth of $\kappa_{ri} = 0.5$ is only obtained for $z_{ri} \approx 60$. The situation is different for open models or models with a cosmological constant. An approximate scaling for the optical depth valid

for $\Omega_0 z_{ri} \gg 1$ is $\kappa_{ri} \propto (h\Omega_b x_e/\Omega_0^{1/2})(1 + z_{ri})^{3/2}$, so for example reionization starting at $z_{ri} \approx 23$ will produce an optical depth $\kappa_{ri} \approx 0.5$ in a model with $\Omega_0 = 0.2$, $H_0 = 70\text{km sec}^{-1} \text{ Mpc}^{-1}$ and $\Omega_b = 0.1$.

The polarization increase on large scales produced by an early reionization of the universe can have an important impact on the accuracy with which future satellite missions will be able to reconstruct cosmological parameters from CMB. This will be the focus of chapter 5. There will be other polarization experiments from the ground before the satellites fly, for example POLAR at Wisconsin University [11] and POLATRON from CalTech [12]. We illustrate the impact of the reionization signal in the polarization by looking at the Wisconsin experiment. It will try to measure both Q and U parameters with an expected sensitivity of $1\mu K$ per pixel. The instrument will allow measurements with a $7°$ FWHM at an early stage and a $1°$ FWHM afterwards. This corresponds to a gaussian window function, $W_l = \exp[-(l + 0.5)^2\sigma_\theta^2]$, $\sigma_\theta = \theta/2\sqrt{(2\ln 2)}$ where θ is the FWHM of the detector in radians. The predicted values for the Stokes parameters were calculated numerically and the spectra normalized to COBE. The expected *rms* values of Q for standard CDM with no reionization are $P(7°) = 4.8 \times 10^{-2}\mu K$ and $P(1°) = 0.77\mu K$. These values, especially the large angular scale one, are extremely small and thus very difficult to detect. This is the reason why the reionized scenarios are the most promising to detect polarization.

Reionization will not only change the polarization power spectrum but also the temperature one, and could suppress the acoustic peaks completely. There is some degree of degeneracy between the different parameters determining the CMB spectra, for example a reionization with a moderate optical depth will decrease the amplitude of the acoustic peaks but this effect may be compensated by changing the spectral index [13]. In fact only an optical depth in the $0.10-0.20$ range seems detectable from temperature maps alone [1, 2, 3]. Figure 4-4 shows both polarization and temperature power spectra for standard CDM with a spectral index $n = 1$ and a reionized model with $\kappa_{ri} = 0.5$ but a spectral index $n = 1.2$. The differences in the anisotropy power spectra are not large, while the polarization spectra are very different. The *rms P* values in this reionized case are $P(7°) = 1.2\mu K$ and $P(1°) = 1.8\mu K$. For the

106
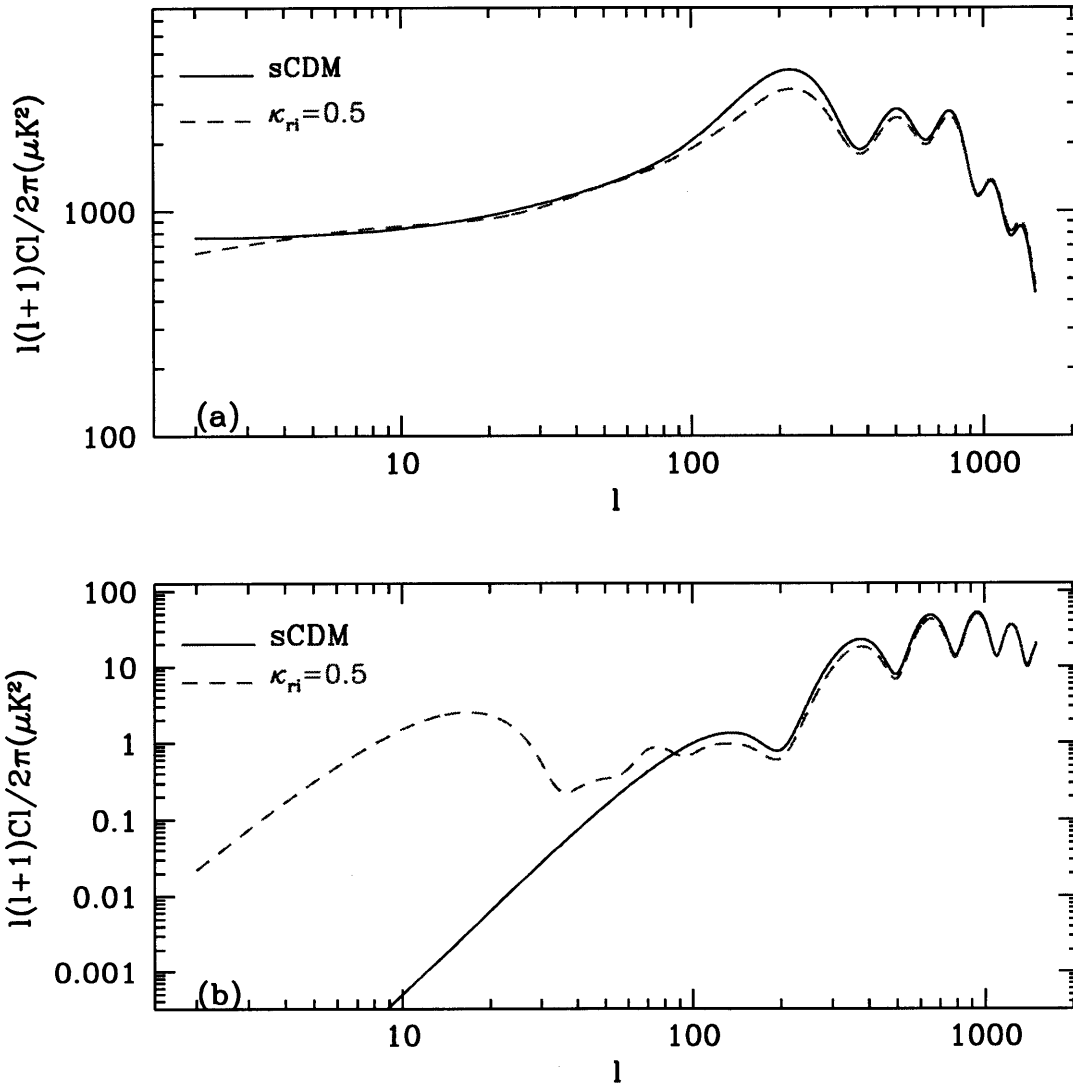
Figure 4-4: $l(l+1)C_l/2\pi$ for both temperature (a) and polarization (b) for standard CDM and a model where the optical depth to recombination is $\kappa_{ri} = 0.5$ and a spectral index $n = 1.2$.

large angular scale experiment the difference with standard CDM is more than two orders of magnitude and in the one degree case is more than a factor of two. Thus a polarization measurement would much more easily distinguish between these two scenarios.

Figure 4-5 shows the *rms* value of P as a function of κ_{ri}, the major parameter determining the amplitude of the polarization perturbation. $P(7^\circ)$ only exceeds $1\mu K$ for $\kappa_{ri} \geq 0.5$ but saturates quickly near $1.8\mu K$. On the other hand $P(1^\circ)$ quickly raises above $1\mu K$ and reaches $3.2\mu K$ for an optical depth of two. This means that even a negative detection at the $1\mu K$ level for the one degree experiment is enough to rule out some models, those with optical depth $\kappa_{ri} \geq 0.3$. Parameters other than κ_{ri} do not make much difference in the height of the peaks. Table 4.1 explores the dependence of $P(7^\circ)$ and $P(1^\circ)$ with different cosmological parameters for a fixed $\kappa_{ri} = 1.0$. Although the height of the peaks remains almost constant in these models, slight shifts in their location change the predicted P. The 7° *rms* linear polarization is more sensitive to the position of the first peak. The 1° experiment has the best chance of putting interesting constraints on a possible reionization, as the expected signal is greater because it is sensitive to all the power in the new peaks of the polarization power spectrum. A correlation analysis between the polarization in the forty pixels that the experiment will measure may further improve the above limits.

In summary, the polarization of the microwave background is very sensitive to the ionization history of the universe and an early reionization can greatly enhance it. We have discussed in detail the physics behind the generation of polarization in reionized scenarios and the appearance of new peaks in the polarization power spectrum. We have identified the major parameters determining the location of these peaks, the ratio of distances between the observer and the reionization scattering surface to that between reionization and recombination. The height of the peaks is mainly function of κ_{ri}, the optical depth to recombination.
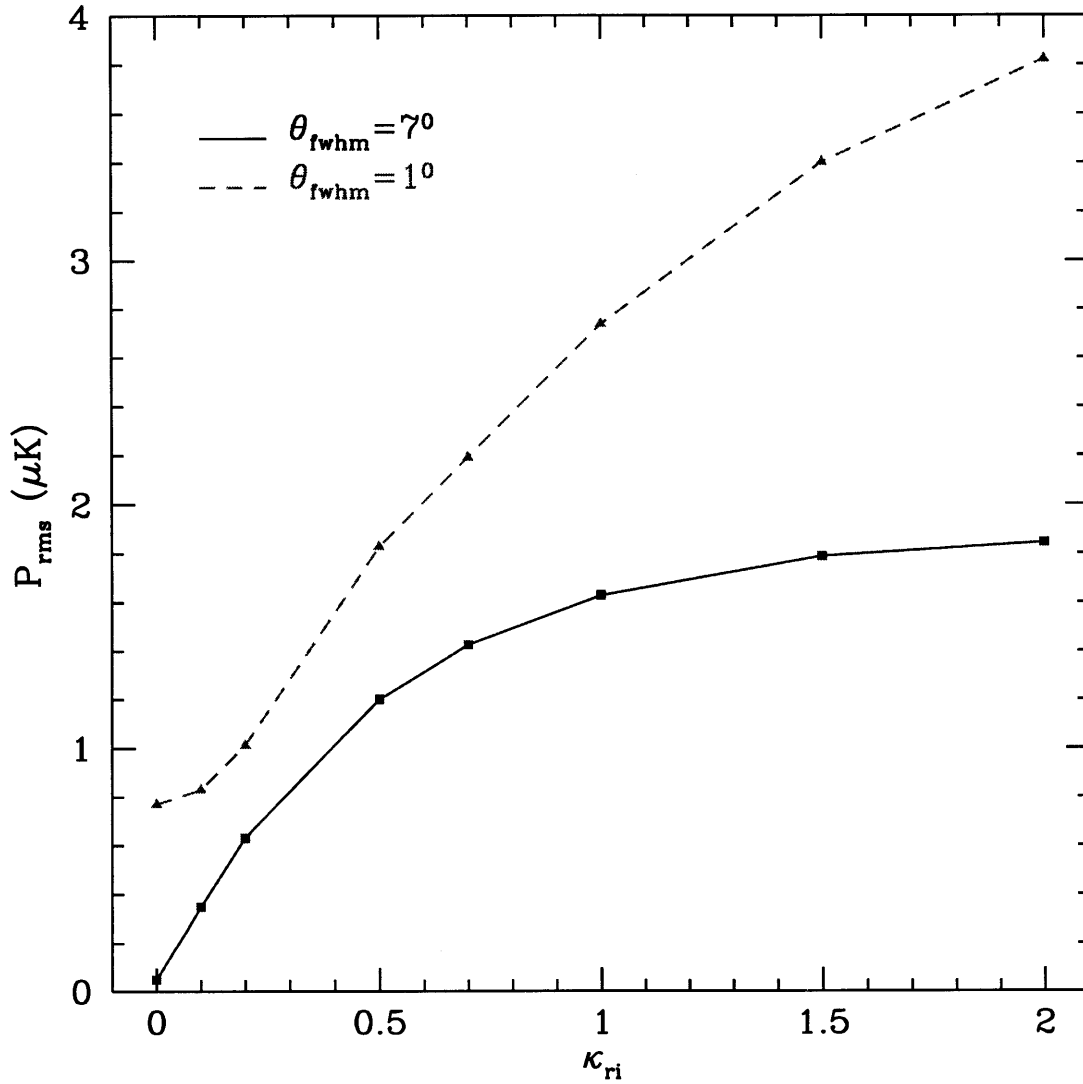
Figure 4-5: Polarization *rms* fluctuations (μK) as a function of the optical depth, κ_{ri} for a 7° and 1° FWHM experiments.

Table 4.1: Degree of linear polarization in μK SCDM (first row) and several cosmological models all with $\kappa_{ri} = 1.0$. The value of the cosmological constant is such that all the above models are flat, $\Omega_{total} = 1.0$. H_0 is the Hubble constant in km sec^{-1}Mpc^{-1}.

Ω_0	Ω_b	H_0	$P(7°)$	$P(1°)$
1.0	0.05	50	$4.81\,10^{-2}$	0.642
0.7	0.05	50	1.62	2.25
0.5	0.05	50	1.67	2.50
0.3	0.05	50	1.62	2.25
1.0	0.03	50	1.40	2.67
1.0	0.08	50	1.83	2.79
1.0	0.10	50	1.91	2.80
1.0	0.05	60	1.72	2.79
1.0	0.05	80	1.84	2.85
1.0	0.05	100	1.92	2.88

4.3 The Detection of Non-Scalar Perturbations

Primordial gravity waves produce fluctuations in the tensor component of the metric, which could result in a significant contribution to the CMB anisotropies on large angular scales. Unfortunately, the presence of scalar modes prevents one from clearly separating one contribution from another. If there are only a finite number of multipoles where the tensor contribution is significant then there is a limit in amplitude beyond which tensors cannot be distinguished from random fluctuations. In a noise free experiment the tensor to scalar ratio T/S needs to be larger than 0.15 to be measurable in temperature maps [16]. Independent determination of the tensor spectral slope n_T is even less accurate and a rejection of the consistency relation in inflationary models $T/S = -7n_T$ is only possible if $|n_T| \gg (T/S)/7$ [16, 17]. Polarization produced by tensor modes has also been studied [18], but only in the small scale limit. In previous work correlations between the Stokes parameters Q and U have been used. These two variables are not the most suitable for the analysis as they depend on the orientation of coordinate system. In Chapter 2 we presented a full spherical analysis of polarization using Newman-Penrose spin-s spherical harmonic decomposition. We have shown that there is a particular combination of Stokes pa-

rameters that vanishes in the case of scalar modes, which can thus be used as a probe of gravity waves. Here we discuss the sensitivity needed to detect this signal and compare it to the expected sensitivities of future CMB satellites We use the expressions in Chapters 2 and 3 to evaluate the power spectra in various theoretical models. We use T/S as the parameter determining the amplitude of tensor polarization. Figure 4-6 shows the predictions for scalar and tensor contribution in standard CDM model with no reionization (a) and in reionized universe with optical depth of $\kappa_{ri} = 0.2$ (b). The latter value is typical in standard cosmological models [19]. We assumed $T/S = 1$ and $n_T = (n_s - 1) = -0.15$. In the no-reionization case both tensor spectra peak around $l \sim 100$ and give comparable contributions, although the B channel is somewhat smaller. Comparing the scalar and tensor E channels one can see that scalar polarization dominates for $T/S \lesssim 1$. Even though tensor contribution is larger than scalar at low l, the overall power there is too small to be measurable. Tensor reconstruction in the E channel suffers from similar drawbacks as in the case of temperature anisotropies: because of large scalar contribution, cosmic variance prevents one from isolating very small tensor contributions [16]. The situation improves if the epoch of reionization occurred sufficiently early that a moderate optical depth to Thomson scattering is accumulated (Fig. 4-6b). In this case there is an additional peak at low l [20] and the relative contribution of tensor to scalar polarization in E channel around $l = 10$ is higher than around $l = 100$. Still, if $T/S \ll 1$ cosmic variance again limits out ability to extract unambiguously the tensor contribution. It is in this limit that the importance of the B channel becomes crucial. This channel is not contaminated by scalar contributions and is only limited by noise, so in principle with sufficient noise sensitivity one can detect even very small tensor to scalar ratios. Moreover, a detection of signal in this channel would be a model independent detection of non-scalar perturbations. In the following we will discuss sensitivity to gravity waves using both only B channel information alone and all available information.

We can obtain an estimate of how well can tensor parameters be reconstructed by using only the B channel and assuming that the rest of cosmological parameters will be accurately determined from the temperature and E polarization measurements.

111

While this test might not be the most powerful it is the least model dependent: any detection in B channel would imply a presence of non-scalar fluctuations and therefore give a significant constraint on cosmological models. Because the B channel does not cross-correlate with either T or E [21, 22, 23] only its auto-correlation needs to be considered. A useful method to estimate parameter sensitivity for a given experiment is to use the Fisher information matrix introduced in equation (2.36) [1, 21, 22, 23],

$$
\begin{aligned}
\alpha_{ij} &= \sum_{l=2}^{l_{\max}} \frac{(2l+1)f_{\text{sky}}}{2} \\
&\times \left[C_{Bl} + \frac{4\pi\sigma^2}{N} e^{l(l+1)\sigma_b^2} \right]^{-2} \left(\frac{\partial C_{Bl}}{\partial s_i} \right) \left(\frac{\partial C_{Bl}}{\partial s_j} \right),
\end{aligned}
\tag{4.9}
$$

where f_{sky} is the sky coverage. Receiver noise can be parametrized by $4\pi\sigma^2/N$, where σ is the noise per pixel and N is the number of pixels. Typical values are $(0.15\mu\text{K})^2$ for MAP and $(0.025\mu\text{K})^2$ for the most sensitive Planck bolometer channel in one year of observation. In our case the parameters s_i can be T/S and n_T, so that the matrix is only 2x2. The error on each parameter is given by $(\alpha_{ii}^{-1})^{1/2}$ if the other parameter is assumed to be unknown and $(\alpha_{ii})^{-1/2}$ if the other parameter is assumed to be known. Using this expression we may calculate the experiment sensitivity to these parameters. Current inflationary models and limits from large scale structure and COBE predict T/S to be less than unity. Figure 4-6 shows that the expected amplitude in this case is below $0.5\mu\text{K}$. We find that MAP is not sufficiently sensitive in the B channel to detect these low levels. On the other hand, Planck will be much more sensitive and can detect $T/S > 0.2$ if the tensor index n_T is assumed to be known (for example through the consistency relation). For the underlying model with $T/S = 1$ one can determine it with an error $\Delta(T/S) \sim 0.1$. If the tensor index is not known then a combination of the two parameters, which corresponds to the total power under the B curve in Figure 4-6, can still be determined with the same accuracy.

Separate determination of the tensor amplitude and slope from the B channel is only possible in reionized models. In the no-reionization model the contribution to B is very narrow in l space and the leverage on n_T independent of T/S is small,
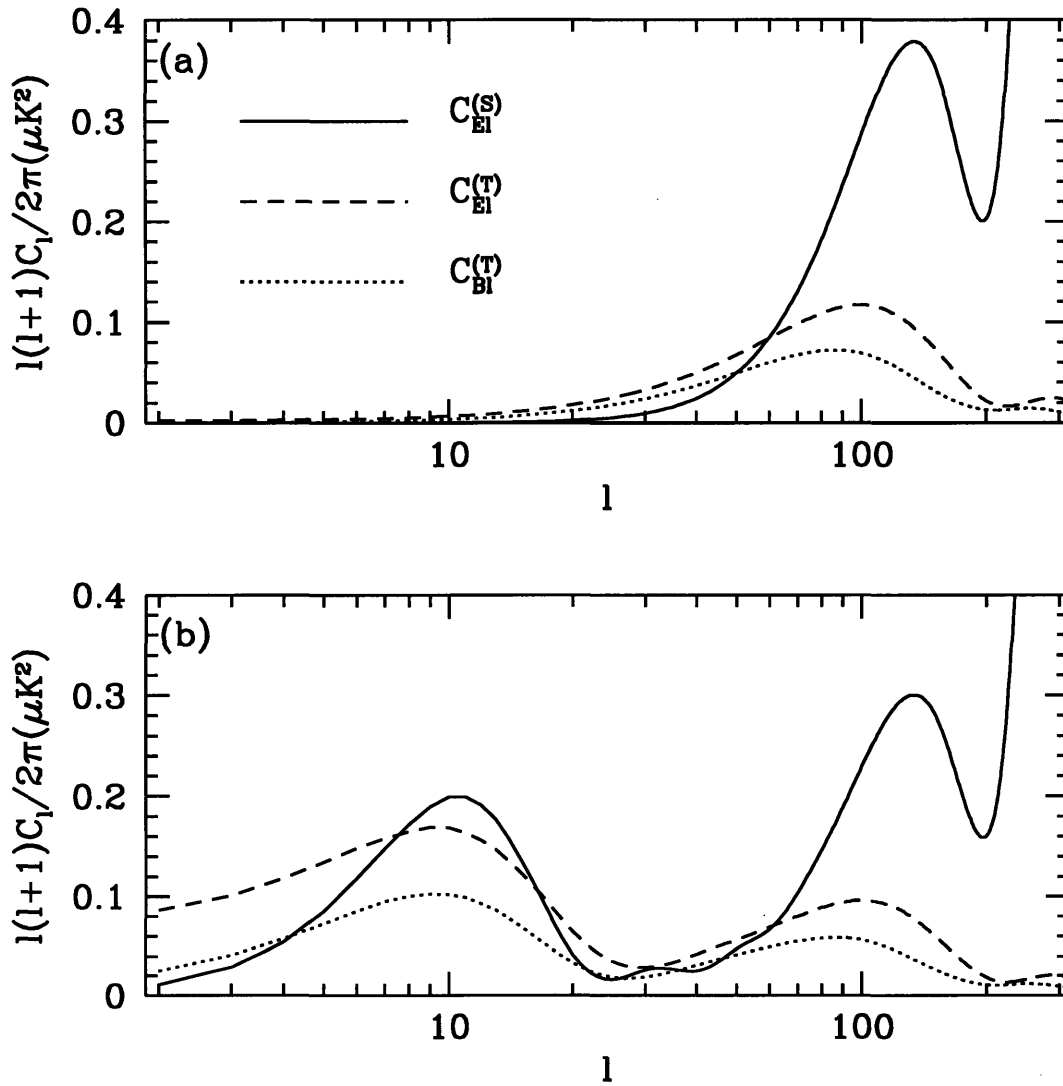
Figure 4-6: Multipole moments for the three polarization spectra for no-reionization case (a) and reionized case with optical depth of 0.2 (b). The underlying model is "standard CDM" with $T/S = 1$.

so that the correlation coefficient $\alpha_{12}/(\alpha_{11}\alpha_{22})^{1/2}$ is almost always close to unity. A modest amount of reionization improves the separation; in the reionized models the power spectrum for B is bimodal (Figure 4-6) and the overall signal is higher, which gives a better leverage on n_T independent of T/S. For $\kappa_{ri} = 0.2$ the Planck errors are $\Delta(T/S) \sim 0.15$ and $\Delta n_T \sim 0.1$ for the underlying model with $T/S = 1$. These results depend on the overall amplitude relative to the noise level. As long as both peaks can be separated from the noise one can determine the tensor slope, which allows to test the inflationary consistency relation.

Combining temperature, E polarization and their cross-correlation further improves these estimates. In this case other parameters that affect scalar modes such as baryon density, Hubble constant or cosmological constant enter as well and the results become more model dependent (Chapter 5). The Fisher information matrix has to be generalized to include all the parameters that can be degenerate with the tensor parameters. The results depend on the class of models and number of parameters one restricts to in the analysis, as opposed to the results based on B channel above, which depend only on the two main parameters that characterize the gravity wave production. As a typical example, for $T/S = 0.1$ and $\kappa_{ri} = 0.1$ one can determine $\Delta(T/S) = 0.05$ and $\Delta n_T = 0.2$ with Planck [3]. These errors improve further if a model with higher T/S or κ_{ri} is assumed. For the same underlying model without using polarization the expected errors are $\Delta T/S \sim 0.26$ and $\Delta n_T \sim 1$, significantly worse than with polarization. Even for MAP the limits on T/S improve by a factor of 2 when polarization information is included.

To summarize the above discussion, future CMB missions are likely to reach the sensitivities needed to measure (or reject) a significant production of primordial gravity waves in the early universe through polarization measurements, which will vastly improve the limits possible from temperature measurements alone and will allow a test of consistency relation. The more challenging question is wether the foreground can be subtracted to at the required level. At low frequencies radio point sources and synchrotron emission from our galaxy dominate the foregrounds and both are polarized at a 10% level. Their contribution decreases at higher frequencies and with

several frequency measurements one can subtract these foregrounds at frequencies around 100 GHz at the required microkelvin level. At even higher frequencies dust is the dominant foreground, but is measured to be only a few percent polarized [24].

While we discussed only scalar and tensor modes, vector modes, if present before recombination, will also contribute to both polarization channels and so could contaminate the signature of gravity waves. At present there are no viable cosmological models that would produce a significant contribution of vector modes without a comparable amount of tensor modes. In inflationary models vector modes, even if produced during inflation, decay away and are not significant during recombination. In topological defect models nonlinear sources continuously create both vector and tensor modes and so some of the signal in B channel could be caused by vector modes. Even in these models however a significant fraction of signal in B will still be generated by tensor modes and in any case, absence of signal in B channel would rule out such models. Polarization thus offers a unique way to probe cosmological models that is within reach of the next generation of CMB experiments.

4.4 A Test of the Causal Structure of the Universe

There are two competing families of models to explain the origin of the structure we observe in our universe: defect models, where a symmetry breaking phase transition generates seeds that form sub-horizon scale density fluctuations, and inflationary models, where a period of superluminal expansion turns quantum fluctuations into super-horizon density perturbations. A fundamental difference between these two mechanisms of structure formation is that only inflation alters the causal structure of the very early universe and is able to create correlations on super-horizon scales, while defects are causal and all correlations vanish for events where both light cones do not overlap.

The COBE satellite observed correlations on angles much larger than that sub-

tended by the horizon at decoupling ($\theta_h \sim 1.1°$) in the CMB temperature. This does not however, imply that there were correlations on super horizon scales at decoupling because a time dependent gravitational potential can produce temperature fluctuations at late-times through the integrated Sachs Wolfe effect (ISW). For example, cosmic string or texture models can reproduce the COBE results despite being causal models by generating the fluctuations at low redshift.

Measurements of temperature fluctuations at small scales have been suggested as a potential test of inflation: inflationary models and most non-inflationary ones predict different locations and relative heights for the acoustic peaks [25]. Unfortunately, causality alone is insufficient to distinguish inflationary and non-inflationary temperature power spectra: causal sources that mimic exactly the inflationary pattern of peaks can be constructed [26]. While the predicted CMB fluctuations of the current family of defect models differ significantly from inflationary predictions [27], it is useful to have model independent tests of the causal structure of the early universe.

Polarization fluctuations are produced by Thomson scattering during the decoupling of matter and radiation. Thus, unlike temperature fluctuations, they are unaffected by the ISW effect. Measurements of the polarization fluctuations are certain to probe the surface of last scattering. Hence, the detection of correlated polarization fluctuations on super-horizon scales at last scattering provides a clear signature of the existence of super-horizon scale fluctuations, one of the distinctive predictions of inflation.[3]

We will work in the initially unperturbed synchronous gauge, where the metric is given by $ds^2 = a^2(\tau)[-d\tau^2 + (\delta_{ij} + h_{ij})dx^i dx^j]$. We will consider only perturbations produced by scalar modes and will solve the Einstein equations in the presence of sources (e.g., defects) using the stiff approximation [28]. The sources are characterized by their covariantly conserved stress energy tensor $\Theta_{\mu\nu}$. Before recombination, matter and radiation act as a very tightly coupled fluid, so the evolution of fluctuations can

---

[3]In this section we will consider the correlation function in real space (ie. as a function of the separation angle) rather than the usual power spectrum. By doing so we can easily express the causality constraint, while it would become a set of integral constraints that the power spectra have to satisfy in the now more usual treatment in term of C_ls.

be described by

$$\ddot{\delta}_C + \frac{\dot{a}}{a}\dot{\delta}_C = 4\pi G(\sum_N(1 + 3c_N^2)\rho_N\delta_N + \Theta_{00} + \Theta)$$

$$\dot{\delta}_R = \frac{4}{3}\dot{\delta}_C - \frac{4}{3}\nabla\cdot\mathbf{v_R}$$

$$\dot{\mathbf{v_R}} = -(1 - 3c_S^2)\frac{\dot{a}}{a}\mathbf{v_R} - \frac{3}{4}c_S^2\nabla\delta_R, \qquad (4.10)$$

where Θ is the trace of the spatial part of $\Theta_{\mu\nu}$, $\Theta/3$ is the source pressure, δ_R and $\mathbf{v_R}$ describe the energy density and velocity of the photon-baryon fluid and δ_C is the energy density of cold dark matter. In synchronous gauge, the cold dark matter has zero velocity. The sum over N is carried out over all species and c_S is the sound speed. Temperature and polarization anisotropies seen on the sky today depend on δ_R and $\mathbf{v_R}$ at decoupling.

Equations (4.10) imply that the photon-baryon fluid propagates information at the speed of sound and thus cannot generate correlations on scales larger than the sound horizon. Causality on the other hand implies that the unequal time correlators of the sources $\langle\Theta_{\mu\nu}(r,\tau)\Theta_{\mu\nu}(0,\tau')\rangle$ vanishes if $r > \tau + \tau'$. In the absence of initial correlations, these two conditions together imply that $\langle X|_{\tau_*}(\hat{n}_1)X|_{\tau_*}(\hat{n}_2)\rangle = 0$ if $\theta_{12} > 2\theta_h \sim 2°$, where $X = \delta_R, \mathbf{v_R}, \partial_i\mathbf{v_R}$ and τ_* is the conformal time of decoupling.

In the thin scattering surface approximation, equations (4.10) are solved up to recombination and then the photons free stream to the observer. The final temperature anisotropy in direction $\hat{n}$ on the sky is (equation 2.43),

$$T(\hat{n}) = \frac{\delta_R}{4}|_{\tau_*} - \hat{n}\cdot\mathbf{v_R}|_{\tau_*} - \frac{1}{2}\int_{\tau_*}^{\tau_0} d\tau\,\dot{h}_{ij}\hat{n}^i\hat{n}^j. \qquad (4.11)$$

The first two terms are evaluated at the last scattering surface and the third term is an integral along the line of sight, the ISW effect. In non-inflationary models, the first two terms cannot correlate temperature fluctuations at separations larger than $2\theta_h \sim 2°$ but because anisotropies can be created later through the ISW effect these models can have temperature correlations on larger angular scales.

For the polarization we had (equation 2.44),

$$(Q + iU)(\hat{n}) \approx 0.17 \Delta \tau_* \mathbf{m}^i \mathbf{m}^j \partial_i v_j |_{\tau_*}. \tag{4.12}$$

This equation shows that the observed polarization only depends on the state of the fluid at the last scattering surface. No correlations can be present in the polarization for separations larger than $\sim 2^o$ in non-inflationary models. An early reionization of the universe alters this argument, we will discuss that later.

The correlation functions of Q and U (in their natural coordinate system) are given by (eq. 2.18),

$$C^{(Q,U)}(\theta) = \sum_l \frac{2l+1}{4\pi} [C_l^{(E,B)} F_l^1(\theta) - C_l^{(B,E)} F_l^2(\theta)] \tag{4.13}$$

where $\pm_2 Y_l^2(\theta, \phi) = \sqrt{(2l+1)/4\pi} \ [F_l^1(\theta) \pm F_l^2(\theta)] \ \exp(2i\phi)$. Both correlation functions receive contributions from the E and B channels. The E channel contains all the cosmological signal if there are no tensor or vector modes.

We computed both $C^{(Q,U)}(\theta)$ for the model proposed by Turok [26] which has a clever choice of source stress energy tensor that is able to reproduce the pattern of peaks of inflationary standard CDM (sCDM). The results are shown in Figure 4-7. We see that the inflationary model is able to produce polarization correlations on angular scales larger than $\sim 2^o$, while the other model cannot. On smaller angular scale than shown in Figure 4-7, the two correlation functions coincide. The difference between the two models is a result of the causal constraints and is insensitive to source evolution. It is also worth pointing out that in inflationary models the large scale polarization is suppressed relative to the small scale signal, so we are after a small effect.

Next, we estimate the expected uncertainties in measuring $C^{(Q,U)}(\theta)$. Since receiver noise is the likely to be the dominant source of variance, we can make a simple estimate of the total noise: it is proportional to the number of independent pairs of pixels, N_p, at a given separation, θ. For an experiment with a beam FWHM θ_{fwhm},

$N_p = 1/2 \times (4\pi/\theta_{fwhm}^2) \times (2\pi\theta/\theta_{fwhm})$. If $\sigma_{(Q,U)}^2$ is the noise in the polarization measurement per resolution element, then the noise in the cross correlation is given by $\Delta C^{(Q,U)} = \sqrt{2/N_p}\ \sigma_{(Q,U)}^2 \approx 20\ w_P^{-1}\sqrt{0.2^\circ/\theta_{fwhm}}\sqrt{2^\circ/\theta}$ where $w_P^{-1} = \sigma_{(Q,U)}^2\ \Omega_{pix}/4\pi$.

We can make a more accurate determination of the noise using the covariance matrix of the different power spectra (equation 2.34):

$$\text{Cov}(\hat{C}_{(E,B)l}^2) = \frac{2}{2l+1}(\hat{C}_{(E,B)l} + w_P^{-1}e^{l^2\sigma_b^2})^2 \tag{4.14}$$

which give the following variances for the correlation functions,

$$(\Delta C^{(Q,U)})^2 = \sum_l (\frac{2l+1}{4\pi})^2\{\text{Cov}(C_{(E,B)l}^2)\ [F_l^1(\theta)]^2$$
$$+ \text{Cov}(C_{(B,E)l}^2)\ [F_l^2(\theta)]^2\}. \tag{4.15}$$

Figure 4-7 shows the noise in each correlation, in the limit where the variances are dominated by receiver noise $(\Delta C^Q)^2 = (\Delta C^U)^2$ and agree perfectly with our previous estimates. If either the cosmic variance is important or the power spectra of E and B differ, then the approximate estimate of the previous paragraph is not accurate and the full calculation should be used to estimate the noise.

The noise in the correlation functions can be reduced by focusing on the E-like piece of the polarization. The noise in the both $C^{(Q,U)}(\theta)$ receives contributions from the variances in both E and B spectra (equation 4.15), but by computing both contributions separately we can show that the variance in $E(B)$ makes the dominant contribution to $\Delta C^Q(\Delta C^U)$. If we filter the maps to pull out only the E component, then we remove not only the B signal but also some of the noise and ΔC^U is reduced almost by a factor of ~ 4. The assumption that most of the signal is in the E channel can be checked within the data as both E and B contributions can be measured separately from the maps.

For the MAP satellite, without filtering the noise, $\Delta C^{(Q,U)} \approx 0.36/\sqrt{\theta}\ \mu K^2$, so it will not be sensitive enough to detect this signal, even if we combine all of the three highest frequencies. However, if we filter the map to extract the E channel

signal, then the noise in the MAP experiment drops to $\Delta C^U \sim 0.1/\sqrt{\theta} \; \mu K^2$, and the C^U signal should be detectable. The PLANCK satellite, with its very sensitive bolometers, should be able to achieve $\Delta C^{(Q,U)} \approx 0.003/\sqrt{\theta} \; \mu K^2$ and should easily be able to detect both C^U and C^Q. As cosmic variance is not the dominant contribution to the noise, an experiment observing a small patch of the sky could also potentially detect this signal.

The temperature-polarization cross-correlation [29] is another potential test of the origin of fluctuations: although ISW effects produce temperature fluctuations after decoupling, we still do not expect correlations between temperature and polarization on large angular scales for defect models. The correlations between temperature and polarization fluctuations directions $\hat{n}_1$ and $\hat{n}_2$ are,

$$\langle Q(\hat{n}_1)T(\hat{n}_2)\rangle = \langle Q_1^* T_2^*\rangle - \frac{1}{2}\int_{\tau_*}^{\tau_0} d\tau \hat{n}_1^i \hat{n}_1^j \langle h_{ij}(\tau)Q_1^*\rangle, \qquad (4.16)$$

T^* stands for the first two terms in equation (4.11) and Q^* is given by equation (4.12).

In the polarization temperature cross correlation, only the term involving the line of sight integration could produce correlations on large angular scales. This would require correlations between the late time variations of the metric and the velocity at last scattering. For this to occur in defect models, they must be moving very fast and remain coherent as they evolve from recombination to very late times. As Figure 1(c) shows, even Turok's causal seed model, which mimics inflation remarkable well in the temperature correlation does not predict any temperature-polarization correlation.

If gravity waves, rather than scalar modes, were the dominant source of the anisotropies, then they could, in principle, create a cross correlations on large angular scales. However, if gravity waves were significant enough to create a large signal, then they would be directly detectable in the B channel.

Figure 4-7(c) shows the calculated values of the cross correlation together with the expected noise. The signal is well above the noise for MAP and Planck. The detection of a large angular scale cross correlation with no appreciable signal in the polarization B channel would put very stringent limits on the physics of models trying

to mimic inflation.

There is one caveat to our argument: reionization. If the universe reionized very early, a significant fraction of the observed polarization will come from the rescattering of photons at late times. In most scenarios, the fraction of rescattered photons is thought to be less than $\sim 20\%$ [19]. Reionization has two effects on our argument. First, it reduces the amplitude of the correlation function by a factor $\exp\left(-2\kappa_{ri}\right)$, where κ_{ri} is the optical depth to decoupling ($\kappa_{ri} \leq 0.2$). Second, it creates further structure in the correlation function on large angular scales. Fortunately, the effect of reionization can be separated from that of the primordial anisotropies: it leaves a very specific signature in the power spectrum, a peak at very low l that is easily distinguish from the l^6 dependence expected from causality constraints alone [20, 30, 31]. Because of the form of $F_l^1(\theta)$ and $F_l^2(\theta)$, this peak produces an almost constant positive offset in C^Q and C^U for angles $\theta \sim 2^o$. Because the offset in C^U is positive ($F_l^2(\theta) < 0$ for $\theta \sim 2^o$ and $l < 70$) reionization at a relatively recent epoch can never create the negative peak at $\theta \sim 2^o$ predicted by inflationary models.

There is a precise signature in $C^{(Q,U)}(\theta)$ on $\sim 2^o$ scales that would allow an unambiguous test of inflation. The signal is small, but within reach for the new generation of experiments. The cross correlation between temperature and polarization is also expected to provide strong constraints that could distinguish inflation from non-inflationary models: this signal is much larger and will be well above the noise for MAP. The next generation of satellites or even polarization measurements from the ground could provide a definitive test of the inflationary paradigm in the relatively near future.
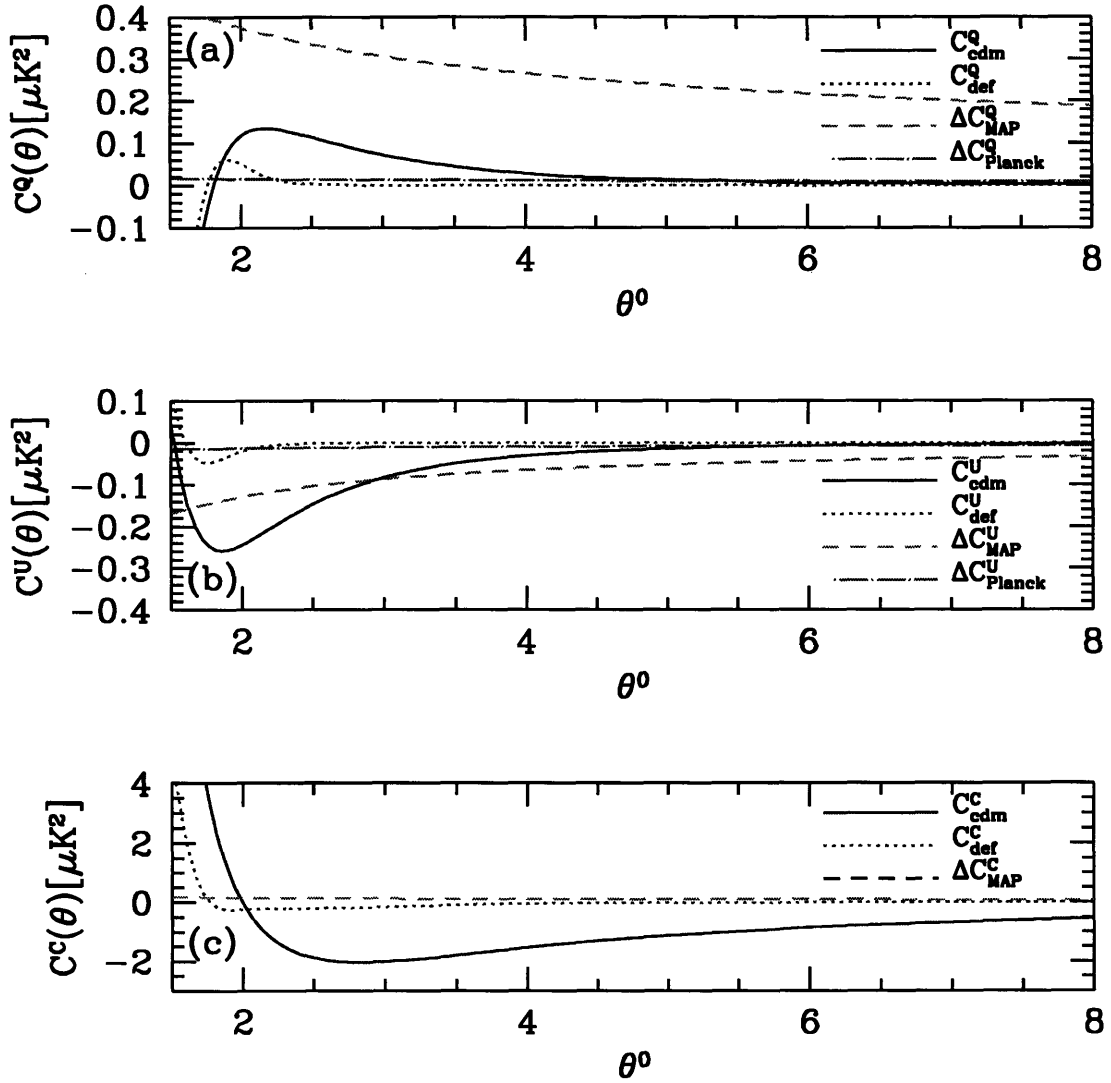
Figure 4-7: Correlation functions for Q (a) and U (b) Stokes parameters for sCDM and the causal seed model discussed in the text. The noise in their determination is shown for both MAP and Planck. Panel (b) shows the expected noise for MAP if the CMB maps are filtered to include only the E channel signal. Panel (c) shows the cross correlation between temperature and polarization and the noise for MAP, the expected variance for Planck is even smaller. Each resolution element in the correlation function should be considered independent.

Bibliography

[1] G. Jungman, M. Kamionkowski, A. Kosowsky & D. N. Spergel, Phys. Rev. Lett. **76**, 1007 (1996); *ibid* Phys. Rev. D **54** 1332 (1996).

[2] J. R. Bond, G. Efstathiou & M. Tegmark, Mon. Not. R. Astron. Soc. **291**, 33 (1997).

[3] M. Zaldarriaga, D. N. Spergel & U. Seljak, Astrophys. J. **488**, 1 (1997).

[4] M. Rees, Astrophys. J. **153**, L1 (1968); J. R. Bond & G. Efstathiou, Astrophys. J. **285**, L47 (1984); *ibid* Mon. Not. R. Astr. Soc. **226**, 655 (1987); M. Zaldarriaga & D. Harari, Phys. Rev. D **52**, 3276 (1995).

[5] J. R. Bond & G. Efstathiou, Astrophys. J., **285**, L45 (1984).

[6] K. L. Ng & K. W. Ng, Astrophys. J. **456**, 413 (1995).

[7] M. Zaldarriaga & D. Harari, Phys. Rev. D **52**, 3276 (1995).

[8] R. A. Frewin, A. G. Polnarev & P. Coles, Mon. Not. R. Astron. Soc., **266**, L 21 (1994).

[9] E. F. Bunn & M. White, Astrophys. J. **480**, 6 (1997).

[10] W. Hu, N. Sugiyama & J. Silk, Nature **386**, 37 (1997).

[11] B. Keating et al., Astrophys. J. **495**, 580 (1998).

[12] Visit http://astro.caltech.edu/ lgg/polatron/psci.html for information on polatron.

[13] J. R. Bond et al., Phys. Rev. Lett., **72**, 13 (1994).

[14] Visit the MAP home page at http://map.gsfc.nasa.gov.

[15] Visit http://astro.estec.esa.nl/SA-general/Projects/Planck for information on Planck.

[16] L. Knox & M. S. Turner, Phys. Rev. Lett. **73**, 3347 (1996).

[17] S. Dodelson, L. Knox & E. W. Kolb, Phys. Rev. Lett. **72**, 3443 (1994).

[18] A. G. Polnarev, Sov. Astron. **29**, 607 (1985); R. Crittenden, R. L. Davis & P. J. Steinhardt, Astrophys. J. Lett. **417**, L13 (1993); R. A. Frewin, A. G. Polnarev & P. Coles, Mon. Not. R. Astron. Soc. **266**, L21 (1994); R. G. Crittenden, D. Coulson & N. G. Turok, Phys. Rev. D **52**, 5402 (1995); A. Kosowsky, Ann. Phys. **246**, 49 (1996).

[19] Z. Haiman & A. Loeb, Astrophys. J., **483**, 21 (1997).

[20] M. Zaldarriaga, Phys. Rev. D **55** 1822 (1997).

[21] U. Seljak, Astrophys. J., **482** 6 (1996).

[22] M. Kamionkowski, A. Kosowsky & A. Stebbins, Phys. Rev. D **55** 7368 (1997).

[23] M. Zaldarriaga & U. Seljak, Phys. Rev. D **55**, 1830 (1997).

[24] R. G. Hildebrand & M. Dragovan, Astrophys. J. **450**, 663 (1995).

[25] W. Hu & M. White, Astrophys. J. **471** 30 (1996); W. Hu, D. Spergel & M. White, Phys. Rev D **55**, 3288 (1997).

[26] N. Turok, Phys. Rev. Lett. **77**, 4138 (1996); *ibid* Phys. Rev. D **54** 3686 (1996).

[27] U. Pen, U. Seljak & N. Turok, Phys. Rev. Lett. **79**. 1611 (1997)

[28] S. Veeraraghavan & A. Stebbins, Astrophys. J. **365** 37 (1990).

[29] D. Coulson, R. Crittenden & N. Turok, Phys. Rev. Lett. **73**. 2390 (1994)

[30] W. Hu & M. White, Phys. Rev. D, **56**, 596 (1997).

[31] R. Battye, private communication.

Chapter 5

Predictions for Future Experiments[1]

It has long been recognized that the microwave sky is sensitive to many cosmological parameters, so that a high resolution map may lead to their accurate determination [1, 2, 3, 4]. The properties of the microwave background fluctuations are sensitive to the geometry of the universe, the baryon-to-photon ratio, the matter density, the Hubble constant, the cosmological constant, and the optical depth due to reionization in the universe. A stochastic background of gravitational waves also leaves an imprint on the CMB and their amplitude and slope may be extracted from the observations. In addition, massive neutrinos and a change in the slope of the primordial spectrum also lead to potentially observable features.

Previous calculations trying to determine how well the various parameters could be constrained were based on approximate methods for computing the CMB spectra [3]. These approximations have an accuracy of several percent, which suffices for the analysis of the present-day data. However, the precision of the future missions will be so high that the use of such approximations will not be sufficient for an accurate determination of the parameters. Although high accuracy calculations are not needed at present to analyze the observations, they are needed to determine how accurately cos-

---

mological parameters can be extracted from a given experiment. This is important not only for illustrative purposes but may also help to guide the experimentalists in the design of the detectors. One may for example address the question of how much improvement one can expect by increasing the angular resolution of an experiment (and by doing so increasing the risk of systematic errors) to decide whether this improvement is worth the additional risk. Another question of current interest is whether it is worth sacrificing some sensitivity in the temperature maps to gain additional information from the polarization of the microwave background. When addressing these questions, the shortcomings of approximations become particularly problematic. The sensitivity to a certain parameter depends on the shape of the likelihood function around the maximum, which in the simplest approach used so far is calculated by differentiating the spectrum with respect to the relevant parameter. This differentiation strongly amplifies any numerical inaccuracies and almost always leads to an unphysical breaking of degeneracies among parameters and misleadingly optimistic results.

Previous analysis of CMB sensitivity to cosmological parameters used only temperature information. However, CMB experiments can measure not just the temperature fluctuations, but also even weaker variations in the polarization of the microwave sky. Instead of one power spectrum, one can measure up to four and so increase the amount of information in the two-point correlators [5, 6, 9]. Polarization can provide particularly useful information regarding the ionization history of the universe [7] and the presence of a tensor contribution [8, 9]. Because these parameters are partially degenerate with others, any improvement in their determination leads to a better reconstruction of other parameters as well. The two proposed satellite missions are currently investigating the possibility of adding or improving their ability to measure polarization, so it is particularly interesting to address the question of improvement in the parameter estimation that results from polarization.

The purpose of this Chapter is to re-examine the determination of cosmological parameters by CMB experiments in light of the issues raised above. It is particularly timely to perform such an analysis now, when the satellite mission parameters are

roughly defined. We use the best current mission parameters in the calculations and hope that our study provides a useful guide for mission optimization. As in previous work [3], we use the Fisher information matrix to answer the question of how accurately parameters can be extracted from the CMB data. This approach requires a fast and accurate method for calculating the spectra and we use the CMBFAST code developed in Chapter 3 [10] with an accuracy of about 1%. We test the Fisher information method by performing a more general exploration of the shape of the likelihood function around its maximum and find that this method is sufficiently accurate for the present purpose.

The outline of this chapter is the following: in Section 5.1, we present the methods used, reviewing the calculation of theoretical spectra and the statistical methods to address the question of sensitivity to cosmological parameters. In Section 5.2, we investigate the parameter sensitivity that could be obtained using temperature information only and in Section 5.3, we repeat this analysis using both temperature and polarization information. In Section 5.4, we explore the accuracy of the Fisher method by performing a more general type of analysis and investigate the effects of prior information in the accuracy of the reconstruction. We present our conclusions in Section 5.5.

5.1 Methods

In this section, we review the methods used to calculate the constraints on different cosmological parameters that could be obtained by the future CMB satellite experiments. We discuss the Fisher information matrix approach, as well as the more general method of exploring the shape of the likelihood function around the minimum.

5.1.1 The Fisher information matrix

The Fisher information matrix is a measure of the width and shape of the likelihood function around its maximum. Its elements are defined as expectation values of the second derivative of a logarithm of the likelihood function with respect to the

128

corresponding pair of parameters. It can be used to estimate the accuracy with which the parameters in the cosmological model could be reconstructed using the CMB data [3, 11]. If only temperature information is given then for each l a derivative of the temperature spectrum C_{Tl} with respect to the parameter under consideration is computed and this information is then summed over all l weighted by $\text{Cov}^{-1}(\hat{C}_{Tl}^2)$. In the more general case implemented here, we have a vector of four derivatives and the weighting is given by the inverse of the covariance matrix,

$$\alpha_{ij} = \sum_l \sum_{X,Y} \frac{\partial C_{Xl}}{\partial s_i} \text{Cov}^{-1}(\hat{C}_{Xl}, \hat{C}_{Yl}) \frac{\partial C_{Yl}}{\partial s_j}. \tag{5.1}$$

Here α_{ij} is the Fisher information matrix, Cov^{-1} is the inverse of the covariance matrix, s_i are the cosmological parameters one would like to estimate and X, Y stands for T, E, B, C. For each l, one has to invert the covariance matrix and sum over X and Y. The derivatives were calculated by finite differences and the step was usually taken to be about 5% of the value of each parameter. We explored the dependence of our results on this choice and found that the dependence is less than 10%. This indicates that the likelihood surface is approximately Gaussian, an assumption of the Fisher matrix method that only consideres the curvature around the maximum of the likelihood. Further tests of this assumption are discussed in Section 5.4.

The full covariance matrix between the power spectrum estimators was presented in [5, 6, 9]. The diagonal terms are given by

$$
\begin{aligned}
\text{Cov}(\hat{C}_{Tl}^2) &= \frac{2}{(2l+1)f_{sky}}(C_{Tl} + w_T^{-1}B_l^{-2})^2 \\
\text{Cov}(\hat{C}_{El}^2) &= \frac{2}{(2l+1)f_{sky}}(C_{El} + w_P^{-1}B_l^{-2})^2 \\
\text{Cov}(\hat{C}_{Bl}^2) &= \frac{2}{(2l+1)f_{sky}}(C_{Bl} + w_P^{-1}B_l^{-2})^2 \\
\text{Cov}(\hat{C}_{Cl}^2) &= \frac{1}{(2l+1)f_{sky}}\left[C_{Cl}^2 + (C_{Tl} + w_T^{-1}B_l^{-2})(C_{El} + w_P^{-1}B_l^{-2})\right],
\end{aligned} \tag{5.2}
$$

while the non-zero off diagonal terms are

$$
\begin{aligned}
\text{Cov}(\hat{C}_{Tl}\hat{C}_{El}) &= \frac{2}{(2l+1)f_{sky}}C_{Cl}^2 \\
\text{Cov}(\hat{C}_{Tl}\hat{C}_{Cl}) &= \frac{2}{(2l+1)f_{sky}}C_{Cl}(C_{Tl} + w_T^{-1}B_l^{-2}) \\
\text{Cov}(\hat{C}_{El}\hat{C}_{Cl}) &= \frac{2}{(2l+1)f_{sky}}C_{Cl}(C_{El} + w_P^{-1}B_l^{-2}).
\end{aligned}
\tag{5.3}
$$

We have defined $w_{(T,P)}^{-1} = 4\pi\sigma_{(T,P)}^2/N_{pix}$ where σ_T and σ_P are noise per pixel in the temperature and either Q or U polarization measurements (they are assumed equal) and N_{pix} is the number of pixels. We will also assume that noise is uncorrelated between different pixels and between different polarization components Q and U. This is only the simplest possible choice and more complicated noise correlations arise if all the components are obtained from a single set of observations. If both temperature and polarization are obtained from the same experiment by adding and differentiating the two polarization states, then $\sigma_T^2 = \sigma_P^2/2$ and noise in the temperature is uncorrelated with the noise in polarization components. The window function B_l^{-2} accounts for the beam smearing and in the Gaussian approximation is given by $B_l^{-2} = \exp l^2\sigma_b^2$, with σ_b measuring the width of the beam. We introduced f_{sky} as the fraction of the sky that can be used in the analysis. In this chapter we assume $f_{sky} = 0.8$. It should be noted that equations (5.2) and (5.3) are valid only in the limit of uniform sky coverage.

Both satellite missions will measure in several frequency channels with different angular resolutions: we combine them using $w_{(T,P)} = \sum w_{(T,P)}^c$, where subscript c refers to each channel component. For the MAP mission we adopt a noise level $w_T^{-1} = (0.11\mu K)^2$ and $w_P^{-1} = (0.15\mu K)^2$ for the combined noise of the three highest frequency channels, with conservatively updated MAP beam sizes: $0.53°$, $0.35°$ and $0.25°$. These beam sizes are smaller than those in the MAP proposal and represent improved estimates of MAP's resolution. The most recent estimates of MAP's beam sizes are even smaller[2]: $0.47°$, $0.35°$ and $0.21°$. For Planck, we assume $w_T^{-1} = (0.011\mu K)^2$

---

[2]See the MAP homepage at http://map.gsfc.nasa.gov.

and $w_P^{-1} = (0.025\mu K)^2$, and combining 140 GHz and 210 GHz bolometer channels. For Planck's polarization sensitivity, we assume a proposed design in which eight out of twelve receivers in each channel have polarizers. The angular resolution at these frequencies is $0.16°$ and $0.12°$ FWHM. We also explore the possible science return from an enhanced bolometer system that achieves polarization sensitivity of $w_P^{-1} = (0.015\mu K)^2$.

In our analysis, we are assuming that foregrounds can be subtracted from the data to the required accuracy. Previous studies of temperature anisotropies have shown that this is not an overly optimistic assumption at least on large angular scales (e.g. [12]). On smaller scales, point source removal as well as secondary processes may make extracting the signal more problematic. This would mostly affect our results on Planck, which has enough angular resolution to measure features in the spectrum to $l \sim 3000$. For this reason, we compared the results by changing the maximum l from 3000 to 1500. We find that they change by less than 30%, so that the conclusions we find should be quite robust. Foregrounds for polarization have not been studied in detail yet. Given that there are fewer foreground sources of polarization and that polarization fractions in CMB and foregrounds are comparable, we will make the optimistic assumption that the foregrounds can be subtracted from the polarization data with sufficient accuracy as well. However, as we will show, most of the additional information from polarization comes from very large angular scales, where the predicted signal is very small. Thus, one should take our results on polarization as preliminary, until a careful analysis of foreground subtraction in polarization shows at what level can polarization signal be extracted.

The inverse of the Fisher matrix, α^{-1}, is an estimate of the covariance matrix between parameters and $\sqrt{(\alpha^{-1})_{ii}}$ approximates the standard error in the estimate of the parameter s_i. This is the lower limit because Cramér-Rao inequality guarantees that for an unbiased estimator the variance on the i-th parameter has to be equal to or larger than $\sqrt{(\alpha^{-1})_{ii}}$. In addition to the diagonal elements of α^{-1}, we will also use 2×2 submatrices of α^{-1} to analyze the covariance between various pairs of parameters. *The Fisher matrix depends not only on the experiment under consideration, but also*

on the assumed family of models and on the number of parameters that are being extracted from the data. To highlight this dependence and to assess how the errors on the parameters depend on these choices we will vary their number and consider several different underlying models.

5.1.2   Minimization

The Fisher information matrix approach assumes that the shape of the likelihood function around the maximum can be approximated by a Gaussian. In this section, we drop this assumption and explore directly the shape of the likelihood function. We use the PORT optimization routines [13] to explore one direction in parameter space at a time by fixing one parameter to a given value and allowing the minimization routine to explore the rest of parameter space to find the minimum of $\chi^2 = \sum_l \sum_{X,Y} (C_{Xl} - C_{Xl}^*) \text{Cov}^{-1}(\hat{C}_{Xl}\hat{C}_{Yl})(C_{Yl} - C_{Yl}^*)$, where C_{Xl}^* denotes the underlying spectrum. The value of χ^2 as a function of this parameter can be compared directly with the Fisher matrix prediction, $\Delta\chi^2 = (s_i - s_i^*)^2/(\alpha^{-1})_{ii}$, where s_i^* is the value of the parameter in the underlying model. This comparison tests not only the shape of the likelihood function around the maximum but also the numerical inaccuracies resulting from differentiating the spectrum with respect to the relevant parameter. The minimization method is also useful for finding explicit examples of degenerate models, models with different underlying parameters but almost indistinguishable spectra.

The additional advantage of the minimization approach is that one can easily impose various prior information on the data in the form of constraints or inequalities. Some of these priors may reflect theoretical prejudice on the part of the person performing the analysis, while others are likely to be less controversial, such as the requirement that matter density, baryon density and optical depth are all positive. One might also be interested in incorporating priors into the estimation to take other astrophysical information into account, e.g. the limits on the Hubble constant or Ω_m from the local measurements. Such additional information can help to break some of the degeneracies present in the CMB data, as discussed in Section 3. Note that prior information on the parameters can also be incorporated into the Fisher matrix

analysis, but in its simplest formulation only in the form of gaussian constraints and not in the form of inequalities.

The main disadvantage of this more general analysis is the computational cost. At each step the minimization routine has to compute derivatives with respect to all the parameters to find the direction in parameter space towards the minimum. If the initial model is sufficiently close to the minimum, then the code typically requires 5-10 steps to find it and to sample the likelihood shape this has to be repeated for several values of the parameter in question (and also for several parameters). This computational cost is significantly higher than in the Fisher matrix approach, where the derivatives with respect to each parameter need to be computed only once.

5.2   Constraints from temperature data

In this section, we investigate how measurements of the CMB temperature anisotropies alone can constrain different cosmological parameters. The models studied here are approximately normalized to COBE, which sets the level of signal to noise for a given experiment. We will start with models in a six-dimensional parameter space $s_6 = (C_2^{(S)}, h, \Omega_\Lambda, \Omega_b, \kappa_{ri}, n_s)$, where the parameters are respectively, the amplitude of the power spectrum for scalar perturbations at $l = 2$ in units of μK^2, the Hubble constant in units of 100 km/s/Mpc, the cosmological constant and baryon density in units of critical density, the reionization optical depth and the slope of primordial density spectrum. In models with a non-zero optical depth, we assume that the universe is instantaneously and fully reionized, so that the ionization fraction is 0 before the redshift of reionization z_{ri} and 1 afterwards. We limit to this simple case because only the total optical depth κ_{ri} can be usefully constrained without polarization information. We discuss the more general case when we discuss polarization below.

The underlying model is standard CDM with $s_6 = (796, 0.5, 0, 0.05, 0.05, 1.0)$. Our base model has an optical depth of 0.05, corresponding to the epoch of reionization at $z_{ri} \approx 13$. Models include gravity waves, fixing the tensor amplitude using the con-

sistency relation predicted by inflation $T/S = -7n_T$ and assuming a relation between the scalar and tensor spectral slopes $n_T = n_s - 1$ for $n_s < 1$ and $n_T = 0$ otherwise, which is predicted by the simplest models of inflation. The results for MAP are summarized in Table 5.1. It is important to keep in mind that the parameters are highly correlated. By investigating confidence contour plots in planes across the parameter space, one can identify combinations of parameters that can be more accurately determined. Previous analytical work [14, 15] showed that the physics of the acoustic oscillations is mainly determined by two parameters, $\Omega_b h^2$ and $\Omega_m h^2$, where Ω_m is the density of matter in units of critical density. There is an approximately flat direction in the three-dimensional space of h, Ω_b and Ω_m: for example, one can change Ω_m and adjust h and Ω_b to keep $\Omega_b h^2$ and $\Omega_m h^2$ constant, which will not change the pattern of acoustic oscillations. This degeneracy can be broken in two ways. On large scales, the decay of the gravitational potential at late times in $\Omega_m \neq 1$ models (the so called late time integrated Sachs-Wolfe or ISW term) produces an additional component in the microwave anisotropy power spectrum, which depends only on Ω_Λ [16]. Because the cosmic variance (finite number of independent multipole moments) is large for small l, this effect cannot completely break the degeneracy. The second way is through the change in the angular size of the acoustic horizon at recombination, which shifts all the features in the spectrum by a multiplicative factor. Around $\Omega_m = 1$, this shift is a rather weak function of Ω_m and scales approximately as $\Omega_m^{-0.1}$, leading to almost no effect at low l, but is increasingly more important towards higher l. MAP is sensitive to multipole moments up to $l \sim 800$, where this effect is small. Consequently MAP's ability to determine the cosmological constant will mostly come from large scales and thus will be limited by the large cosmic variance. Planck has a higher angular resolution and significantly lower noise, so it is sensitive to the change in the angular size of the horizon. Because of this Planck can break the parameter degeneracy and determine the cosmological constant to a high precision, as shown in Table 5.2.

Figure 5-1a shows the confidence contours in the $\Omega_m - h$ and $\Omega_b - h$ planes. The error ellipses are significantly elongated along the lines $\Delta\Omega_b/\Omega_b + 2.1\Delta h/h = 0$ and $\Delta\Omega_m/\Omega_m + 3.0\Delta h/h = 0$. The combinations $\Omega_b h^{2.1}$ and $\Omega_m h^3$ are thus better
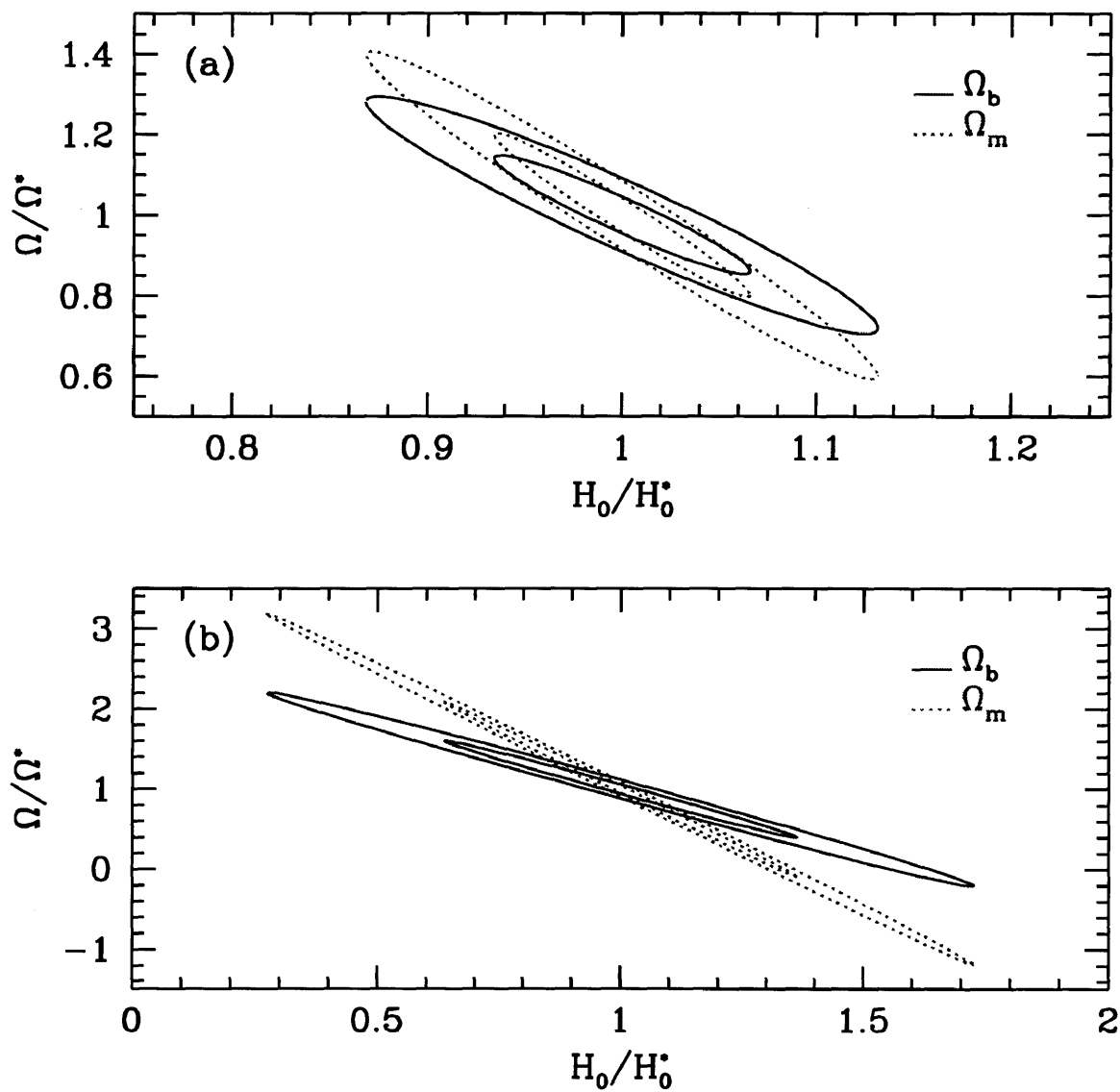
Figure 5-1: MAP confidence contours (68% and 95%) for models in the six parameter space (a) and seven parameter space with T/S added as a free parameter (b). Parameters are normalized to their value in the underlying model denoted with an asterisk.

determined than the parameters Ω_m, Ω_b and h themselves, both to about 3% for MAP. It is interesting to note that it is $\Omega_m h^3$ rather than $\Omega_m h^2$ that is most accurately determined, which reflects the fact that ISW tends to break the degeneracy discussed above. However, because the ISW effect itself can be mimicked by a tilt in the spectral index the degeneracy remains, but is shifted to a different combination of parameters. One sigma standard errors on the two physically motivated parameters are $\Delta(\Omega_b h^2)/\Omega_b h^2 \approx 3\%$ and $\Delta(\Omega_m h^2)/\Omega_m h^2 \approx 5\%$. The fact that there is a certain degree of degeneracy between the parameters has already been noted in previous work (e.g. [1]).

Another approximate degeneracy present in the temperature spectra is between the reionization optical depth κ_{ri} and amplitude $C_2^{(S)}$. Reionization uniformly suppresses the anisotropies from recombination by $e^{-\kappa_{ri}}$. On large angular scales, new anisotropies are generated during reionization by the modes that have not yet entered the horizon. The new anisotropies compensate the $e^{-\kappa_{ri}}$ suppression, so that there is no suppression of anisotropies on COBE scales. On small scales, the modes that have entered the horizon have wavelengths small compared to the width of the new visibility function and so are suppressed because of cancellations between positive and negative contributions along the line of sight and become negligible. The net result is that on small scales the spectrum is suppressed by $e^{-2\kappa_{ri}}$ compared to the large scales. To break the degeneracy between $C_2^{(S)}$ and κ_{ri} one has to be able to measure the amplitude of the anisotropies on both large and small scales and this is again limited on large scales by cosmic variance. Hence one cannot accurately determine the two parameters separately, while their combination $C_2 e^{-2\kappa_{ri}}$ is much better constrained. Figure 5-2 shows that indeed the error ellipsoid is very elongated in the direction $\Delta C_2/C_2 - 0.1\Delta\kappa_{ri}/\kappa_{ri} = 0$, which corresponds to the above combination for $\kappa_{ri} = 0.05$.

We now allow for one more free parameter, the ratio of the tensor to scalar quadrupole anisotropy T/S, fixing the tensor spectral index n_T using the consistency relation predicted by inflation $T/S = -7n_T$ but not assuming a relation between n_T and n_s. The variances for MAP are again summarized in Table 5.1. A comparison
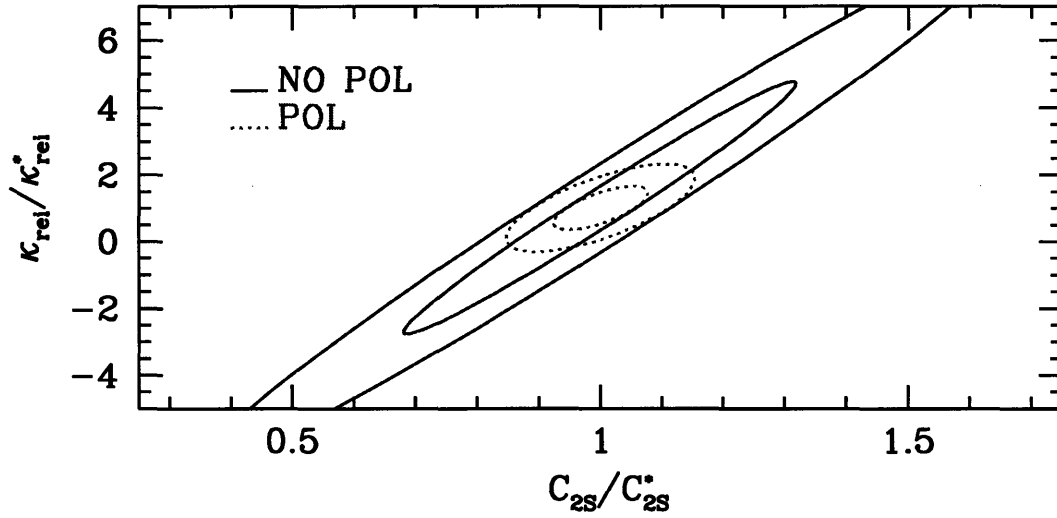
Figure 5-2: Confidence contours (68% & 95%) in the $C_2^{(S)} - \kappa_{ri}$ plane for models in the six parameter space described in the text with (dotted lines) or without (solid lines) polarization information.

with the previous case shows that most variances have increased. The error bars for h and Ω_Λ are approximately five times larger than before while that for n_s has increased by a factor of six and that for $\Omega_b h^2$ by almost four. On the other hand, the error bar for κ_{ri} remains unchanged. It is instructive to look again at the contour plots in the $\Omega_m - h$ and $\Omega_b - h$ planes shown in Figure 5-1b. The degeneracy on individual parameters is significantly worse because the large angular scale amplitude can now be adjusted freely with the new extra degree of freedom, the tensor to scalar ratio T/S. This can therefore compensate any large scale ISW term and so the degeneracy between h, Ω_Λ and Ω_b cannot be broken as easily. However, a combination of the two parameters is still well constrained as shown in Figure 5-1. The degenerate lines are now given by $\Delta\Omega_b/\Omega_b + 1.66\Delta h/h = 0$ and $\Delta\Omega_m/\Omega_m + 3.0\Delta h/h = 0$, with relative errors $\Delta(\Omega_b h^{1.66})/\Omega_b h^{1.66} \approx 4\%$ and $\Delta(\Omega_m h^3)/\Omega_m h^3 \approx 4\%$, almost unchanged from the 6-parameter case. On the other hand for the physically relevant parameters $\Omega_b h^2$ and $\Omega_m h^2$ we now have $\Delta(\Omega_b h^2)/\Omega_b h^2 \approx 10\%$ and $\Delta(\Omega_m h^2)/\Omega_m h^2 \approx 25\%$, which is worse than before. This example indicates how the errors on individual parameters can change dramatically as we add more parameters while certain combinations of them remain almost unaffected.

The output of a minimization run trying to fit sCDM temperature power spectra with models constrained to have $\Omega_\Lambda = 0.6$ shows how different parameters can be adjusted in order to keep the power spectrum nearly the same. The minimization program found the model $s_7 = (610, 0.67, 0.6, 0.03, 0.09, 1.1, 0.68)$ where the last number now corresponds to the T/S ratio, as a model almost indistinguishable from the underlying one. The two models differ by $\Delta\chi^2 = 1.8$ and are shown in Figure 5-3.

It is interesting to analyze how different parameters are adjusted to reproduce the underlying model. By adding gravity waves and increasing both the spectral index and the optical depth, the ISW effect from the cosmological constant can be compensated so that it is only noticeable for the first couple of C_l's. The relatively high amount of tensors ($T/S \sim 0.7$) lowers the scalar normalization and thus the height of the acoustic peaks, which is compensated by the increase in the spectral index to $n_s = 1.1$ and the decrease of $\Omega_m h^2$ from 0.25 to 0.18. The latter moves
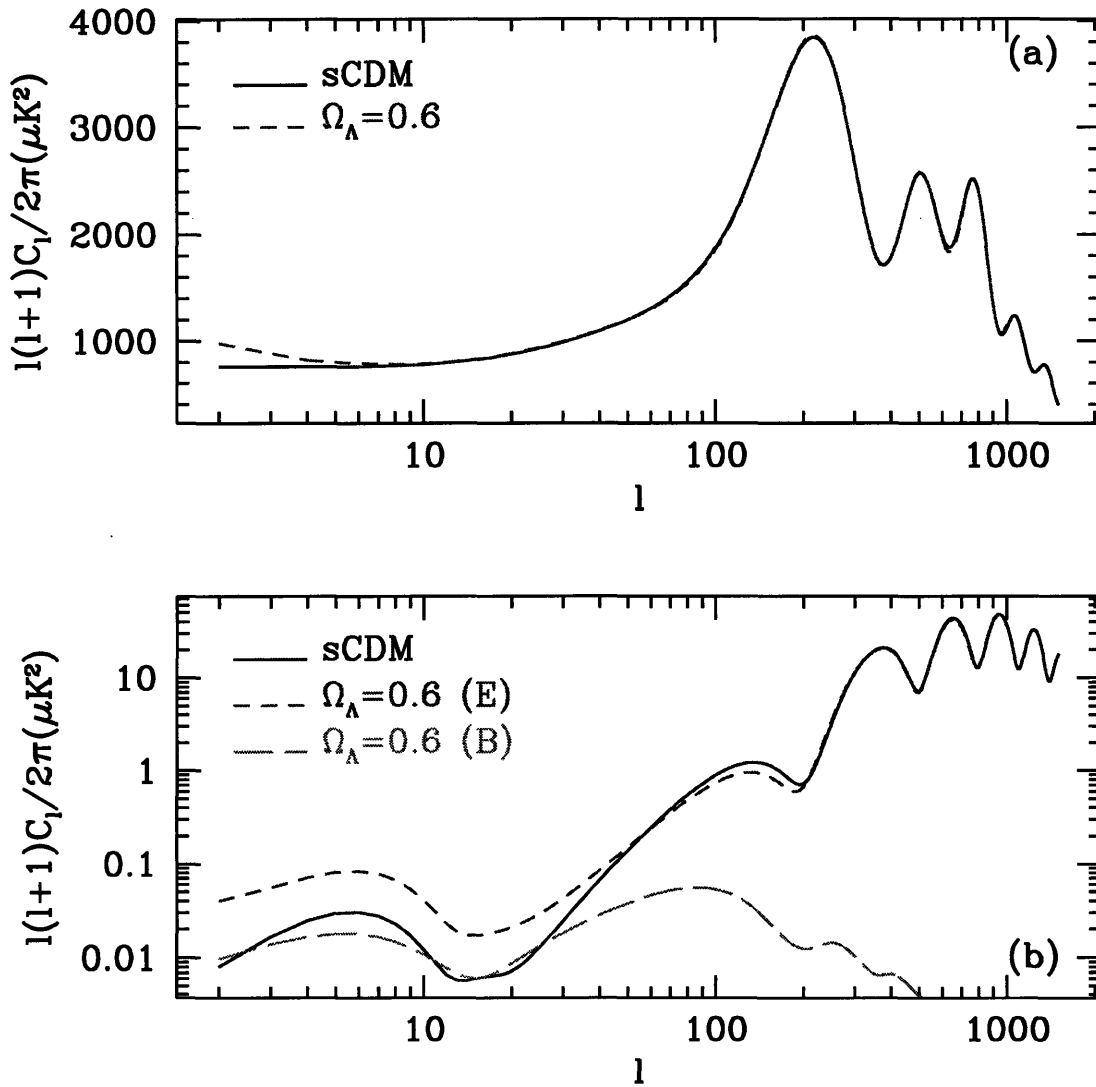
Figure 5-3: Power spectra of (a) temperature and (b) polarization for two models that will be degenerate for MAP if only temperature information is used. The model with $\Omega_\Lambda = 0.6$ is the result of the minimization relative to the sCDM for models constrained to have $\Omega_\Lambda = 0.6$. Polarization helps to break this degeneracy.

the matter radiation equality closer to recombination increasing the height of the peaks. This is the reason why the degeneracy line is not that of constant $\Omega_m h^2$ as Figure 5-1 shows. Changes in $\Omega_m h^2$ change the structure of the peaks and this can be compensated by changing other parameters like the optical depth or the slope of the primordial spectrum. This cannot be achieved across all the spectrum so one can expect that the degeneracy will be lifted as one increases the angular resolution, which is what happens if Planck specifications are used (Table 5.1).

Note that the amount of gravity waves introduced to find the best fit does not follow the relation between n_T and n_s predicted by the simplest inflationary models discussed previously: for $n_s = 1.1$ no gravity waves are predicted. This explains why the addition of T/S as a free parameter increases the sizes of most error bars compared to the 6-parameter case.

While the two models shown in Figure 5-3 have very similar temperature anisotropy spectra, they make very different astronomical predictions. Figure 5-4 shows the matter power spectra of the two models. An interesting effect is that the two models are nearly identical on the scale of $k = 0.1h$ Mpc^{-1}, which corresponds to $l \sim k\tau_0 \sim 600$, the l range where MAP is very sensitive and gravity waves are unimportant. However, the two models differ significantly on the $0.01h$ Mpc^{-1} scale and the power spectrum shape is very different. The current observational situation is still controversial (e.g. [17]), but measurements of the spectrum by the Sloan Digital Sky Survey (SDSS) should significantly improve the power spectrum determination. The models also make different predictions for cluster abundances: the matter dominated model has $\sigma_8 \Omega_m^{0.6} = 1.2$, while the vacuum dominated model has $\sigma_8 \Omega_m^{0.6} = 0.8$. Analysis of cluster X-ray temperature and luminosity functions suggests $\sigma_8 \Omega_m^{0.6} = 0.5 \pm 0.1$ [18], inconsistent with both of the models in the figure. These kind of measurements can break some of the degeneracies in the CMB data.

Observations of Type Ia supernovae at redshifts $z \sim 0.3 - 0.6$ is another very promising way of measuring cosmological parameters. This test complements the CMB constraints because the combination of Ω_m and Ω_Λ that leaves the luminosity distance to a redshift $z \sim 0.3 - 0.6$ unchanged differs from the one that leaves the
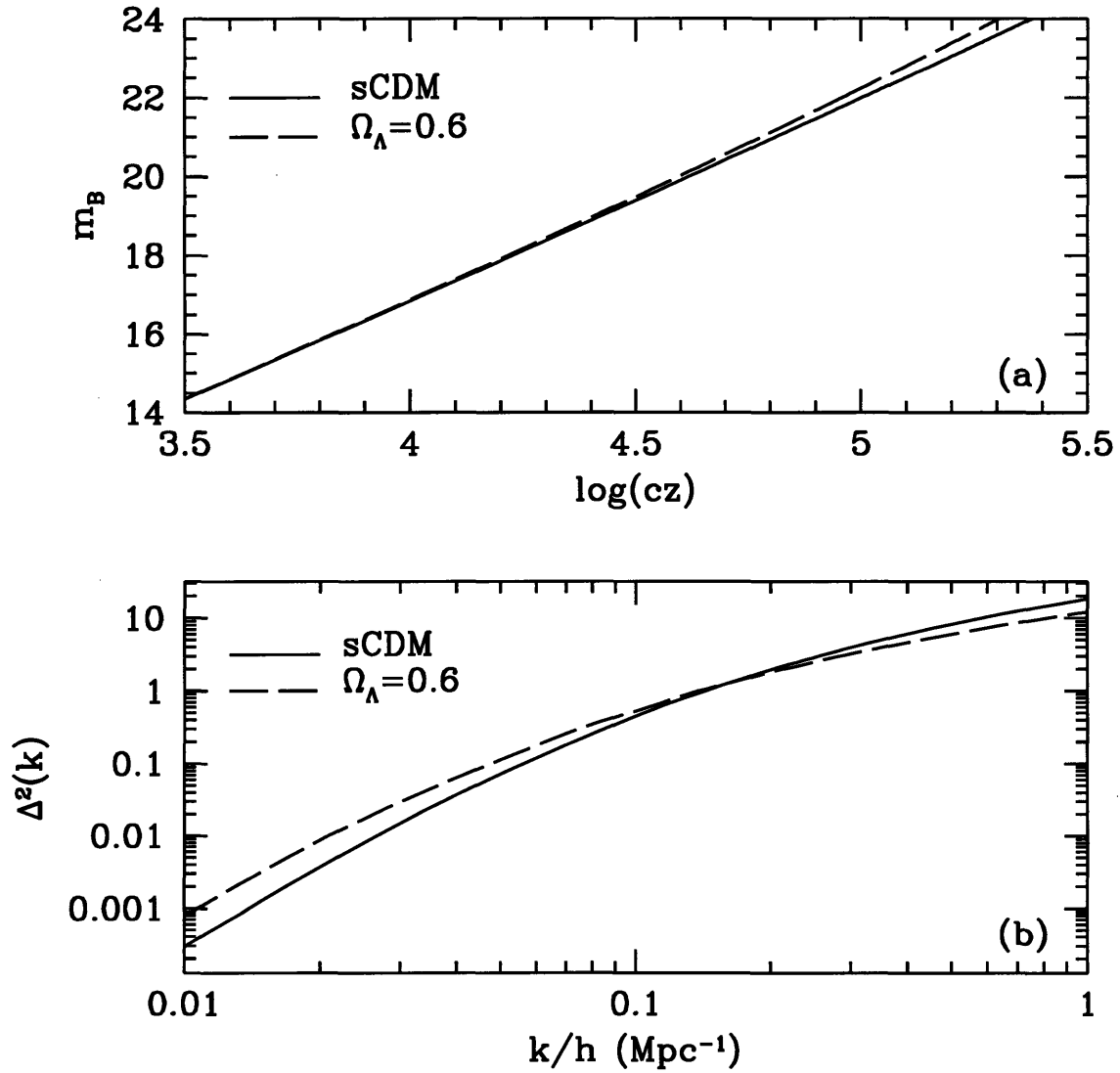
140

Figure 5-4: Hubble diagram for Type Ia supernovae (a) and CDM linear power spectra (b) for sCDM and the $\Omega_\Lambda = 0.6$ model described in the text.

position of the acoustic peaks unchanged. Roughly speaking, the SNe observations are sensitive to $q_0 \simeq \Omega_m/2 - \Omega_\Lambda$, while the CMB observations are sensitive to the luminosity distance which depends on a roughly orthogonal combination, $\Omega_m + \Omega_\Lambda$. Figure 5-4a shows the apparent magnitude vs. redshift plot for supernovae in the two models of Figure 5-2. The analysis in [19] of the first seven supernovae already excludes the $\Omega_\Lambda = 0.6$ model with a high confidence. However, it remains to be seen however whether this test will be free of systematics such as evolutionary effects that have plagued other classical cosmological tests based on the luminosity-redshift relation.

Finally, we may also relax the relation between tensor spectral index and its amplitude, thereby testing the consistency relation of inflation. For MAP, we studied two sCDM models, one with $T/S = 0.28$ and one with $T/S = 0.1$, but with $\kappa_{ri} = 0.1$, for Planck we only used the latter model. Table 5.1 summarizes the obtained one sigma limits. A comparison between the $T/S = 0.28$ model and previous results for sCDM with seven parameters shows that the addition of n_T as a new parameter does not significantly change the expected sensitivities to most parameters. The largest change, as expected, is for the tensor to scalar ratio. We now find $\Delta T/S \sim 0.7$ which means that the consistency relation will only be poorly tested from the temperature measurements. If $T/S = 0.1 and \kappa_{ri} = 0.1$ most error bars are smaller than if $T/S = 0.28 and \kappa_{ri} = 0.05$ case. The reason for this is that the higher value of the optical depth in the underlying model makes its detection easier and this translates to smaller error bars on the other parameters. The only exception is n_T, which has a significantly higher error if $T/S = 0.1$ than if $T/S = 0.28$ as expected on the basis of the smaller contribution of tensor modes to the total anisotropies. A comparison between the expected MAP and Planck performances for the $T/S = 0.1$ model shows that Planck error bars are significantly smaller. For h, $\Omega_b h^2$ and Ω_Λ the improvement is by a factor of $10-20$, while for T/S and $C_2^{(S)}$ by a factor of $2-3$. The limits on κ_{ri} and n_T remain nearly unchanged, reflecting the fact that these parameters are mostly constrained on large angular scales which are cosmic variance and not noise/resolution limited. It is for these parameters that polarization information helps significantly, as discussed in

142

the next section.

The accuracy with which certain parameters can be determined depends not only on the number of parameters but also on their "true" value. We tested the sensitivity of the results by repeating the analysis around a cosmological constant model $s_8 = (922, 0.65, 0.7, 0.06, 0.1, 1.0, 0.1, 0.0)$, where the last number corresponds to the tensor spectral index n_T. Results for MAP specifications are given in Table 5.1. The most dramatic change is for the cosmological constant, which is a factor of ten better constrained in this case. This is because the underlying model has a large ISW effect which increases the anisotropies at small l. This cannot be mimicked by adjusting the tensors, optical depth and scalar slope as can be done if the slope of the underlying model is flat, such as for sCDM model in Figure 5-3. Because of the degeneracy between Ω_Λ and h, a better constraint on the former will also improve the latter, as shown in Table 5.1. Similarly, because a change in Ω_Λ affects T/S, κ_{ri} and n_s on large scales, the limits on these parameters will also change. On the other hand, errors on $\Omega_b h^2$, $C_2^{(S)}$ and n_T do not significantly change. This example clearly shows that the effects of the underlying model can be rather significant for certain parameters, so one has to be careful in quoting the numbers without specifying the "true" parameters of the underlying model as well.

So far we only discussed flat cosmological models. CMBFAST can compute open cosmological models as well, and we will now address the question of how well can curvature be determined using temperature data. We consider models in a six parameter space $s_6 = (C_2^{(S)}, h, \Omega, \Omega_b, \kappa_{ri}, n_s)$, with no gravity waves and where $\Omega_\Lambda = 0$, so that $\Omega = \Omega_m$. We will consider as the underlying model $s_6 = (1122, 0.65, 0.4, 0.06, 0.05, 1.0)$. Fisher matrix results are displayed in Table 5.1. Within this family of models Ω can be determined very precisely by both MAP and Planck due to its effect on the position of the acoustic peaks. This conclusion changes drastically if we also allow cosmological constant, in which case $\Omega = \Omega_m + \Omega_\Lambda$. Both Ω and Ω_Λ change the angular size of the sound horizon at recombination so it is possible to change the two parameters without changing the angular size, hence the two parameters will be nearly degenerate in general. We will discuss this degeneracy in greater

detail in the next section, but we can already say that including both parameters in the analysis increases the error bar on the curvature dramatically.

To summarize our results so far, keeping in mind that the precise numbers depend on the underlying model and the number of parameters being extracted, we may reasonably expect that using temperature information only MAP (Planck) will be able to achieve accuracies of $\Delta C_2^{(S)}/C_2^{(S)} \sim 0.5(0.1)$, $\Delta h \sim 0.1(0.006)$, $\Delta\Omega_\Lambda \sim 0.6(0.03)$, $\Delta(\Omega_b h^2)/\Omega_b h^2 \sim 0.1(0.008)$, $\Delta\kappa_{ri} \sim 0.1(0.1)$, $\Delta n_s \sim 0.07(0.006)$, $\Delta(T/S) \sim 0.7(0.3)$ and $\Delta n_T \sim 1(1)$. It is also worth emphasizing that there are combinations of the parameters that are very well constrained, e.g. $\Delta(\Omega_m h^3)/\Omega_m h^3 \sim 0.04$ and $\Delta(C_2^{(S)})/C_2^{(S)} - 2\Delta\kappa_{ri} \sim 0.05$. For the family of models with curvature but no cosmological constant, MAP (Planck) will be able to achieve $\Delta\Omega \sim 0.007(0.0006)$, determining the curvature of the universe with an impressive accuracy.

These results agree qualitatively, but not quantitatively, with those in [3]. The discrepancy is most significant for $C_2^{(S)}$, h and Ω_Λ, for which the error bars obtained here are significantly larger. The limit we obtain for $\Omega_b h^2$ is several times smaller than that in [3], while for the rest of the parameters the results agree. The use of different codes for computing model predictions is probably the main cause of discrepancies and emphasizes the need to use high accuracy computational codes when performing this type of analysis.

5.3 Constraints from temperature and polarization data

In this section, we consider the constraints on cosmological parameters that could be obtained when both temperature and polarization data are used. To generate polarization, two conditions have to be satisfied: photons need to scatter (Thomson scattering has a polarization dependent scattering cross-section) and the angular distribution of the photon temperature must have a non-zero quadrupole moment. Tight coupling between photons and electrons prior to recombination makes the pho-

ton temperature distribution nearly isotropic and the generated polarization very small, specially on scales larger than the width of the last scattering surface. For this reason polarization has not been considered previously as being important for the determination of cosmological parameters. However, early reionization increases the polarization amplitude on large angular scales in a way which cannot be mimicked with variations in other parameters [7]. The reason for this is that after recombination the quadrupole moment starts to grow due to the photon free streaming. If there is an early reionization with sufficient optical depth, then the new scatterings can transform this angular anisotropy into polarization. This effect dominates on the angular scale of the horizon when reionization occurs. It will produce a peak in the polarization power spectrum with an amplitude proportional to the optical depth, κ_{ri}, and a position $l \sim 2\sqrt{z_{ri}}$, where z_{ri} is the redshift of reionization.

We first consider the six parameter space described in the previous section. Table 5.2 contains the one sigma errors on the parameters for MAP specifications. Compared to the temperature case, the errors improve particularly on the amplitude, the reionization optical depth and the spectral index n_s. Figure 5-2 shows the confidence contours for $C_2^{(S)}$ and κ_{ri} with and without polarization. One can see from this figure how the information in the polarization breaks the degeneracy between the two parameters by reducing the error on κ_{ri}, but does not really improve their non-degenerate combination, which is well determined from the temperature data alone.

We now allow for one more parameter, T/S. Again, polarization improves the errors on most of the parameters by a factor of two compared to the no-polarization case, as summarized in Table 5.2. The optical depth and the amplitude are better constrained for the same reason as for the six parameter model discussed above. Without polarization, the extra freedom allowed by the gravity waves made it possible to compensate the changes on large angular scales caused by the ISW, while the amplitude of small scale fluctuations could be adjusted by changing the optical depth and the spectral index. Changing n_s also changes the slope on large angular scales, compensating for the change caused by the ISW. When polarization is included, a

change on the optical depth produces a large effect in the spectrum: see the model with $\Omega_\Lambda = 0.6$ in Figure 5-2, which has $\kappa_{ri} = 0.1$. The difference in χ^2 between the two models in Figure 5-2 becomes 10 instead of 1.8 (for MAP).

Figure 5-5 shows how the confidence contours in the $\Omega_m - h$ and $\Omega_b - h$ planes are improved by including polarization. The 95% confidence contour corresponds roughly to the 68% confidence contour that could be obtained from temperature information alone, while the orientation of the error ellipsoids does not change. As before the well determined combination is constrained from the temperature data alone. The constraints on tensor parameters also improve when polarization is included. Again, this results from the better sensitivity to the ionization history, which is partially degenerate with the tensor contribution, as discussed in the previous section. The B channel to which only gravity waves contribute is not providing additional information in the model with $T/S = 0.28$ for MAP noise levels. Even in a model with $T/S = 1$ the B channel does not provide additional information in the case of MAP.

With its very sensitive bolometers, Planck has the potential to detect the B channel polarization produced by tensor modes: the B channel provides a signature free of scalar mode contribution [8, 9]. However, it is important to realize that even though for a model with $T/S = 1$ only 20% of the sensitivity of Planck to tensor modes is coming from the B channel. Planck can detected primordial gravity waves in models with $T/S \sim 0.3$ in the B channel alone. If the bolometer sensitivities are improved so that $w_P^{-1} = (0.015\mu K)^2$, then Planck can detect gravity waves in the B channel even if $T/S \sim 0.1$. We also analyzed the 8-parameter models presented in Table 5.2. For the models with $T/S = 0.28$ and $T/S = 0.1$, MAP will not have sufficient sensitivity to test the inflationary consistency relation $T/S = -7n_T$. Planck should have sufficient sensitivity to determine n_T with an error of 0.2 if $T/S \sim 0.1$, which would allow a reasonable test of the consistency relation.

Polarization is helping to constrain most of the parameters mainly by better constraining κ_{ri} and thus removing some of its degeneracies with other parameters. Planck will be able to determine not only the total optical depth through the amplitude of the reionization peak but also the ionization fraction, x_e, through its position.
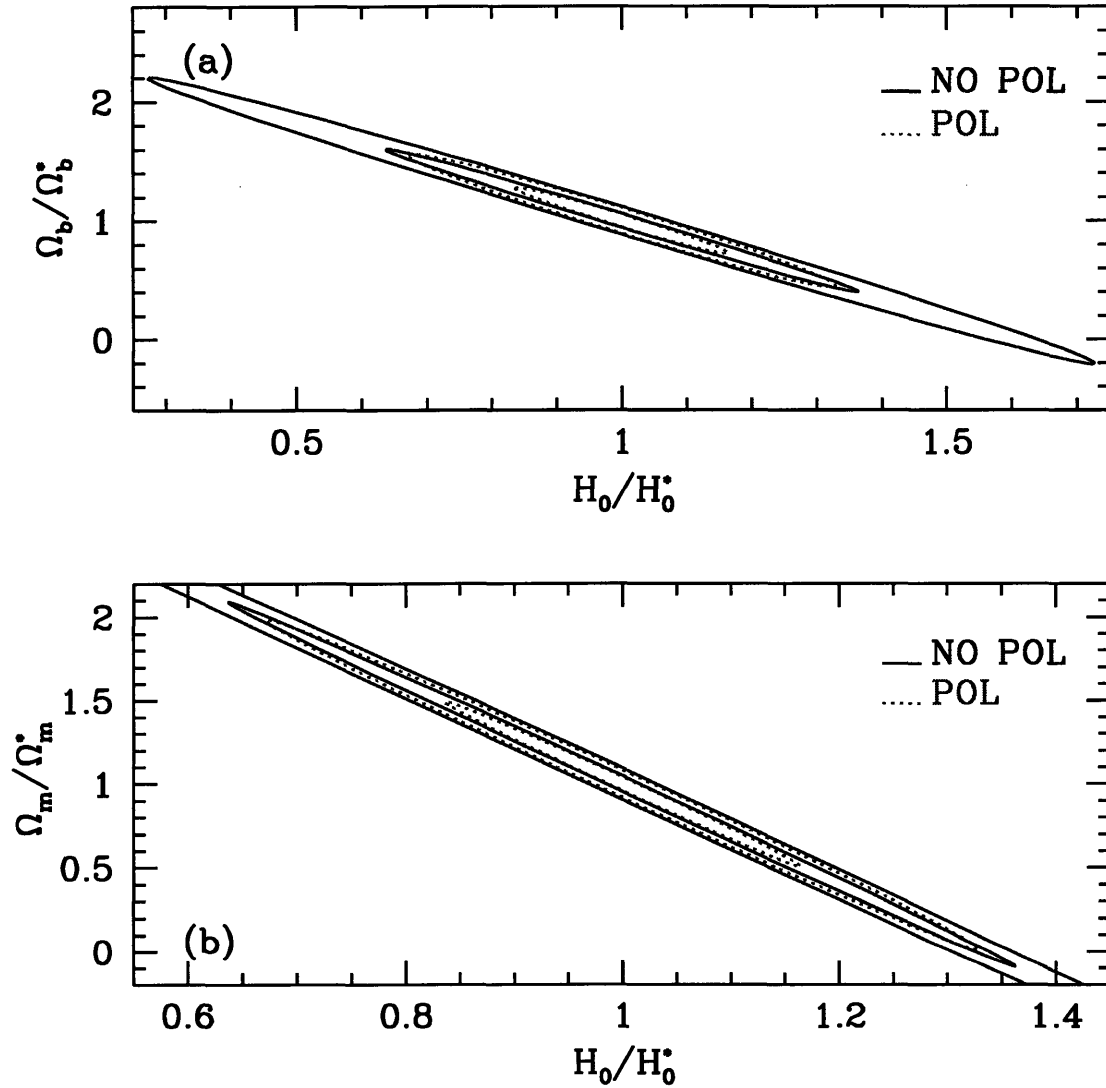
Figure 5-5: Confidence contours (68% & 95%) in the (a) $\Omega_b - h$ plane and (b) $\Omega_m - h$ plane for models in the seven parameter space described in the text with or without using polarization information.

To investigate this, we assumed that the universe reionized instantaneously at z_{ri} and that x_e remains constant but different from 1 for $z < z_{ri}$). The results given in Table 5.2 indicate that x_e can be determined with an accuracy of 15%. This together with the optical depth will be an important test of galaxy formation models which at the moment are consistent with wildly different ionization histories and cannot be probed otherwise [20, 21]. We also investigated the modified Planck design, where both polarization states in bolometers are measured. An improved polarization noise of $w_P^{-1} = (0.015\mu K)^2$ for Planck will shrink the error bars presented in Table 5.2 by an additional $6 - 20\%$. Error bars on Ω_Λ and $\Omega_b h^2$ are reduced by 20%, those in h, κ_{ri} and x_e $10 - 15\%$ and for T/S, n_T and n_s the improvement is approximately 6%.

We can examine in more detail how polarization helps to constrain different cosmological parameters by investigating the angular scales in the polarization power spectra that contribute the most information. To do so, we will consider the $T/S = 0.1$ model and perform a Fisher matrix analysis that includes all the temperature information, but polarization information only up to maximum l. Figures 5-6 (MAP) and 5-7 (Planck) show the increase in accuracy as a function of maximum l for various parameters. In the case of Planck, we added the ionization fraction after reionization as another parameter. Most of the increase in information is coming from the low l portion of polarization spectrum, primarily from the peak produced by reionization around $l \sim 10$. The first acoustic peak in the polarization spectra at $l \sim 100$ explains the second increase in information in the MAP case. The better noise properties and resolution of Planck help to reach the higher l polarization acoustic peaks, which add additional information for constraining h, $\Omega_b h^2$ and Ω_Λ. For Planck, on the other hand, some of the degeneracies will already be lifted in the temperature data alone and so less is gained when polarization data is used to constrain the ionization history.

An interesting question that we can address with the methods developed here is to what extent is one willing to sacrifice the sensitivity in temperature to gain sensitivity in polarization. A specific example is the 140 GHz channel in Planck, where the current proposal is to have four bolometers with no polarization sensitivity and eight bolometers which are polarization sensitive so that they transmit only one
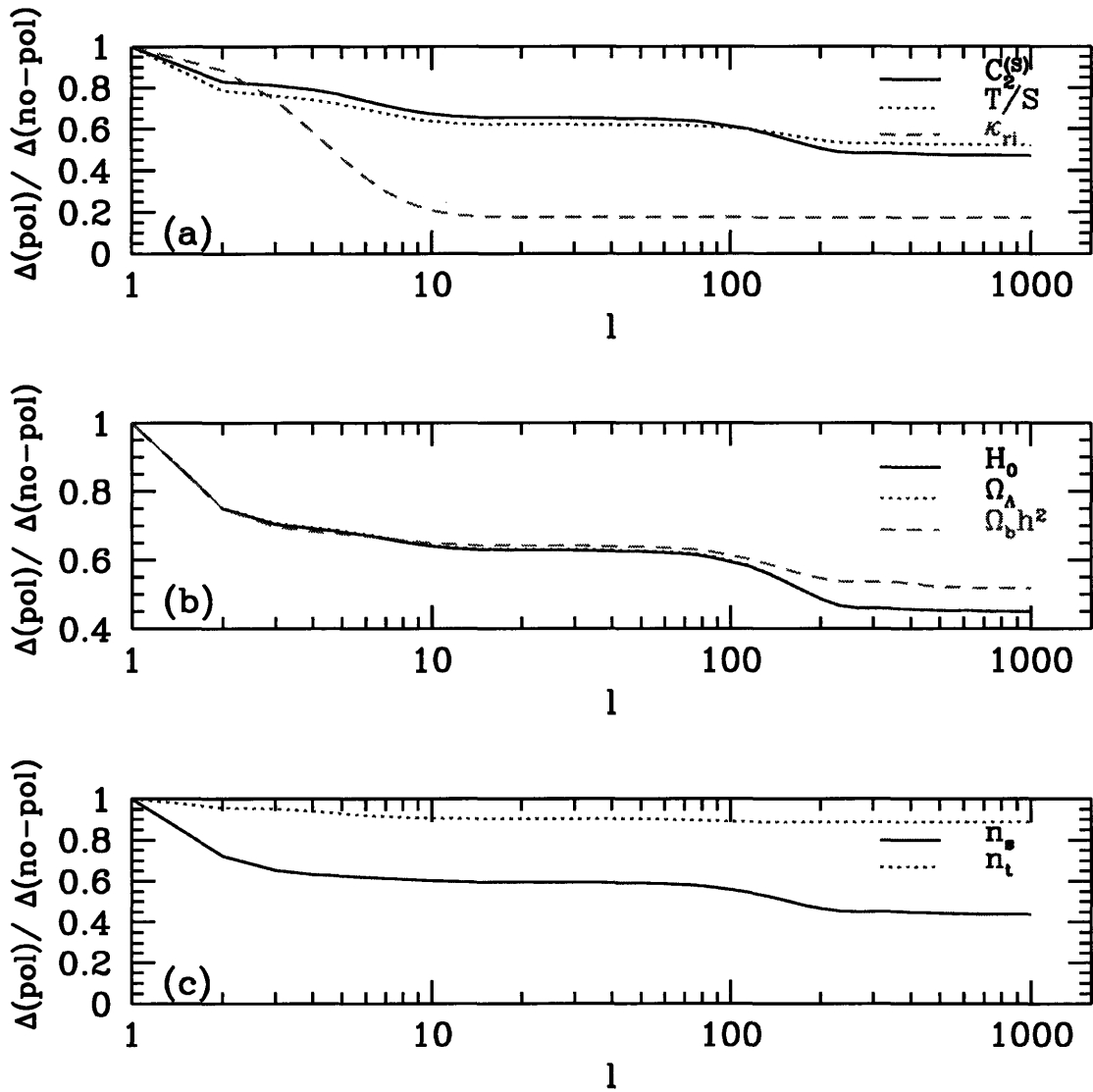
148

Figure 5-6: Relative improvement in the parameter estimation as a function of the maximum l up to which polarization information is used for the MAP mission.
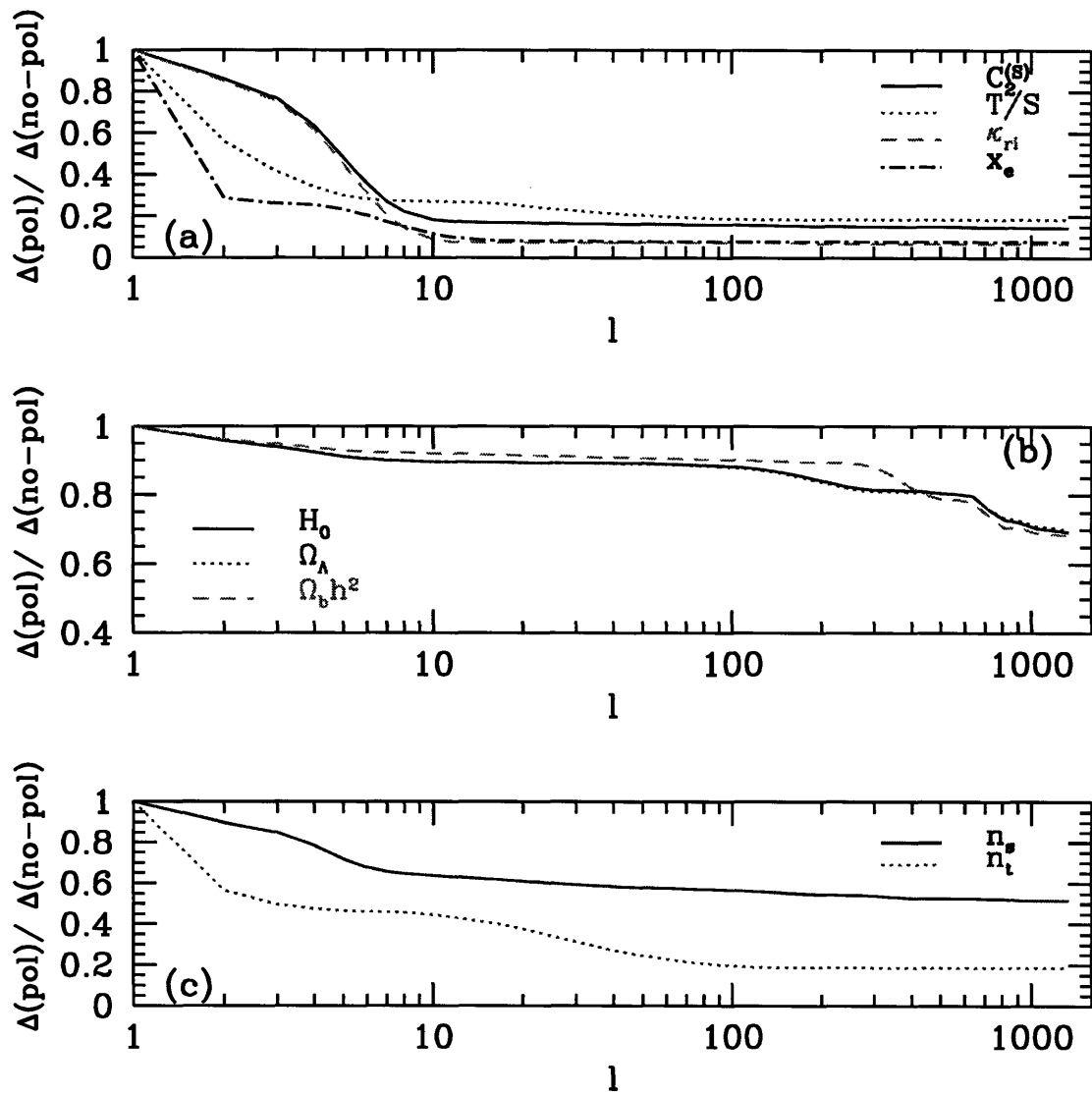
Figure 5-7: Same as figure 6 but for Planck mission parameters.

polarization state while the other is being thrown away. One can compare the results of the Fisher information matrix analysis for this case with the one where all twelve detectors have only temperature sensitivity, but with better overall noise because no photons are being thrown away. The results in this case for the 8 parameter model with $T/S = 0.1$ are 10-20% better than the results given in the fifth column of Table 5.1. These results should be compared to the same case with polarization in Table 5.2. The latter case is clearly better for all the parameters, especially for those that are degenerate with reionization parameters, where the improvement can be quite dramatic. Based on this example it seems clear that it is worth including polarization sensitivity in the bolometer detectors, even at the expense of some sensitivity in the temperature. However, it remains to be seen whether such small levels of polarization can be separated from the foregrounds.

The Fisher matrix results for the six parameter open models are presented in Table 5.2. As expected polarization improved the constraints on $C_2^{(S)}$ and κ_{ri} the most. So far we have explicitly left Ω_Λ out of the analysis; as discussed in Section 3 the positions of the peaks depends on both Ω and Ω_Λ and it is possible to change the two parameters without changing the spectrum. For any given value of Ω_m we may adjust h and Ω_b to keep $\Omega_b h^2$ and $\Omega_m h^2$ constant, so that acoustic oscillations will not change. If we then in addition adjust also Ω_Λ to match the angular size of the acoustic features, then the power spectra for two models with different underlying parameters remain almost unchanged. As mentioned in previous section the effect of Ω_Λ on the positions of the peaks is rather weak around $\Omega_m = 1$ and the peak positions are mostly sensitive to the curvature Ω. The lines of constant l_{peak}, the inverse of the angular size of acoustic horizon, roughly coincide with those of constant Ω near flat models, making it possible to weigh the universe using the position of the peaks. In the more general case, it is not Ω that can be determined from the CMB observations. but a particular combination of Ω_m and Ω_Λ that leaves l_{peak} unchanged. Figure 5-8 shows confidence contours in the $\Omega_m - \Omega_\Lambda$ plane. The contours approximately agree with the constant l_{peak} (dotted) line, which around $\Omega_m = 1$ coincides with the constant Ω line (dashed) but not around $\Omega_m = 0.4$. The squares and triangles correspond to the

151

minima found by the minimization routine when constrained to move in subspaces of constant Ω and agree with the ellipsoids from the Fisher matrix approach.

Figure 5-9 shows the temperature and polarization spectra for the basis model and one found by the minimization routine with $s_o = (1495, .87, 0.6, 0.033, 0.051, 1.0, 0.39)$ where the last number is now Ω_Λ. This model differs from the basis model by a $\chi^2 = 2$ and so is practically indistinguishable from it. Only on large angular scales do the two models differ somewhat, but cosmic variance prevents an accurate separation between the two. In this case, polarization does not help to break the degeneracy. The agreement on the large angular scales is better for polarization than for temperature because the former does not have a contribution from the ISW effect, which is the only effect that can break this degeneracy. When both Ω and Ω_Λ are included in the analysis the 1σ error bars for both MAP and Planck increase. The greatest change is for the error bars on the curvature that now becomes $\Delta\Omega = 0.1$ for both MAP and Planck. Note that improving the angular resolution does not help to break the degeneracy, which is why MAP and Planck results are similar. If one is willing to allow for both cosmological constant and curvature then there is a genuine degeneracy present in the microwave data and constraints from other cosmological probes will be needed to break this degeneracy.

5.4 Shape of the likelihood function, priors and gravitational lensing

As mentioned in Section 2, the Fisher information matrix approach used so far assumes that the likelihood function is Gaussian around the maximum. In previous work [3], this assumption was tested by calculating the likelihood along several directions in parameter space. This approach could miss potential problems in other directions, particularly when there are degeneracies between parameters. We will further test the Gaussian assumption by investigating the shape of the likelihood function varying one parameter at a time but marginalizing over the others. We fix the relevant parameter
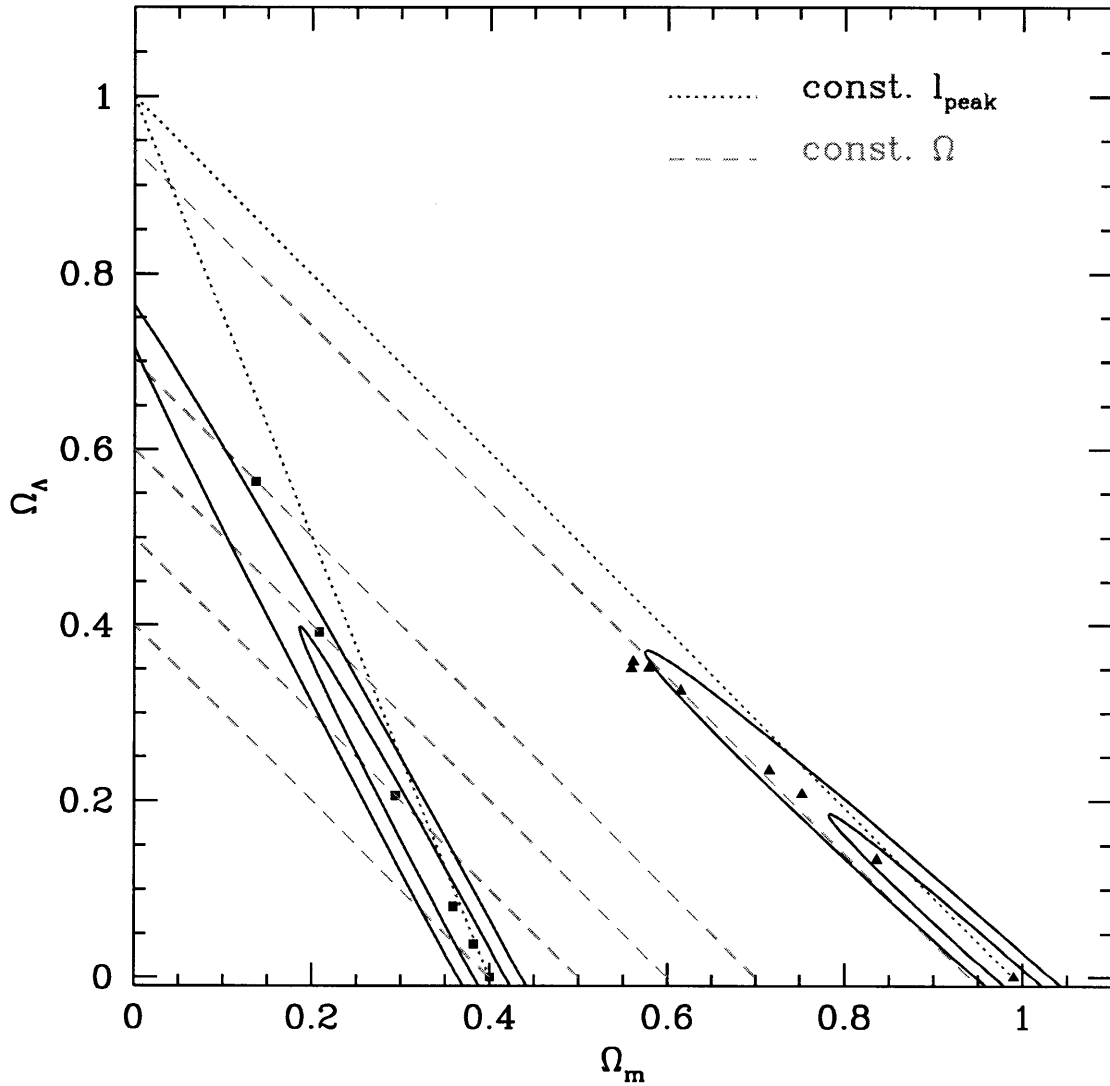
Figure 5-8: Confidence contours (68% & 95%) in the $\Omega_\Lambda - \Omega_m$ plane for open models in the seven parameter space described in the text. The dots show the positions of the χ^2 minima found by the minimization routine when constrained to a subspace of constant Ω.
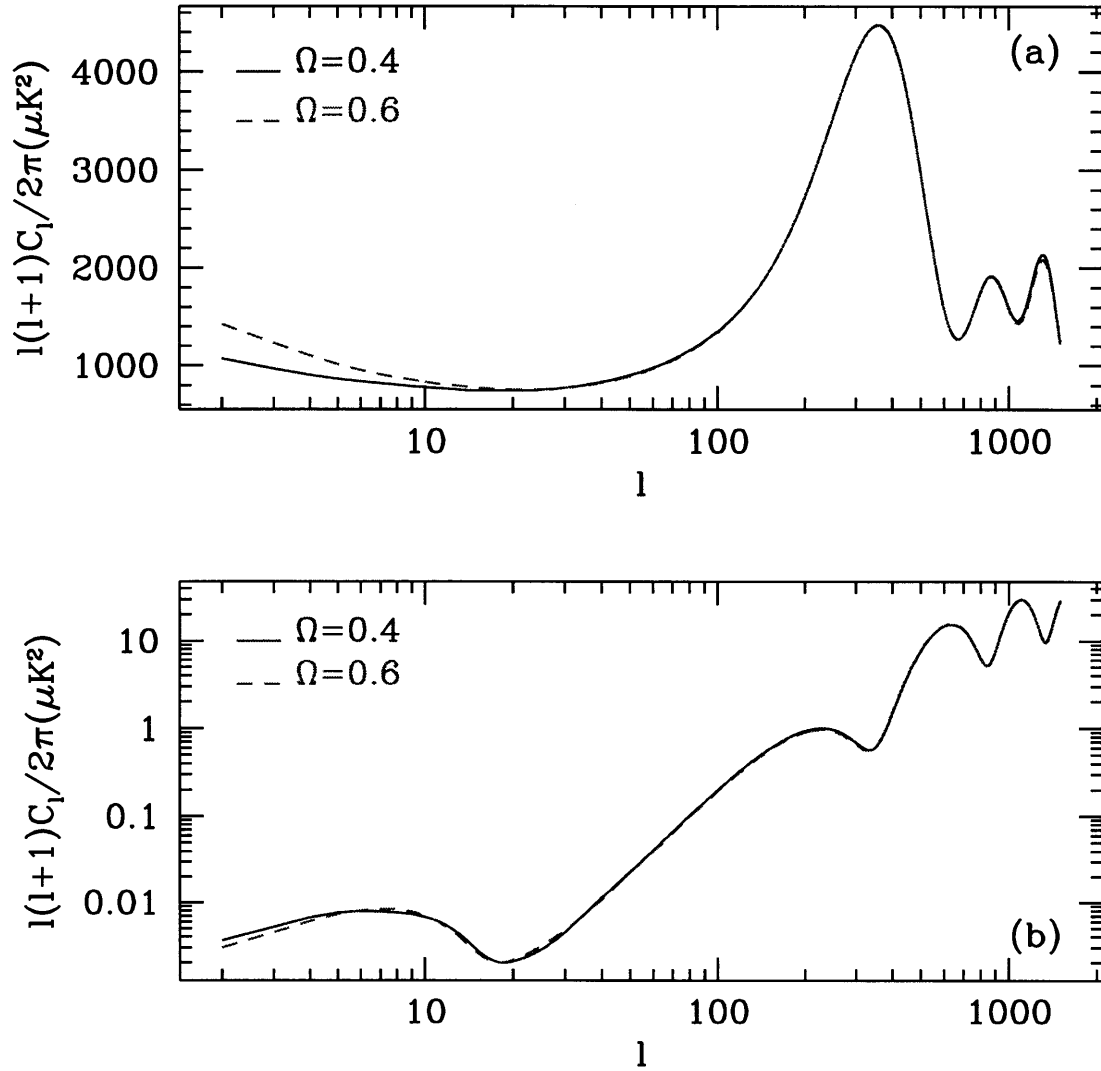
Figure 5-9: Power spectra for (a) temperature and (b) polarization. The model with $\Omega = 0.6, \Omega_\Lambda = 0.4$ is the output of the minimization code when made to fit the $\Omega = 0.4, \Omega_\Lambda = 0$ model. Temperature and polarization data were used for this fit. the two models differ in χ^2 by 2.

and let the minimization routine vary all the others in its search for the smallest χ^2. We then repeat the procedure for a different value of this parameter, mapping the shape of the likelihood function around the minimum. The minimization routine is exploring parameter space in all but one direction. These results may be compared with the prediction of the Fisher matrix which follow a parabola in the parameter versus log-likelihood plot. This comparison tests the gaussianity of the likelihood function in one direction of parameter space at a time.

The panels in Figure 5-10 show two examples of the results of this procedure. In most cases, the agreement between the Fisher matrix results and those of the minimization code is very good, especially very near the minimum (i.e., $\Delta\chi^2 \lesssim 2$). As illustrated in the Ω_b panel, there are cases when χ^2 increased more rapidly than predicted by the Fisher matrix. This is caused by the requirements that κ_{ri}, Ω, Ω_Λ and Ω_b are all positive, which can be enforced easily in the minimization code. Of course, such priors are most relevant if the underlying model is very close to the boundary enforced by the prior and are only important on one side of the parameter space. The importance of this effect therefore depends on the underlying model. If the amount of information in the CMB data on a given parameter is sufficiently high, then the prior will have only a small effect near the maximum of the likelihood function.

We also investigated the effect of gravitational lensing on the parameter reconstruction. As shown in [22], gravitational lensing smears somewhat the acoustic oscillations but leaves the overall shape of the power spectrum unchanged. The amplitude of the effect depends on the power spectrum of density fluctuations. Because the CMBFAST output consists of both CMB and density power spectra one can use them as an input for the calculation of the weak lensing effect following the method in [22]. The gravitational lensing effect is treated self-consistently by normalizing the power spectrum for each model to COBE. We find that the addition of gravitational lensing to the calculation does not appreciably change the expected sensitivity to different parameters that will be attained with the future CMB experiments. This conclusion again depends somewhat on the underlying model, but even for sCDM
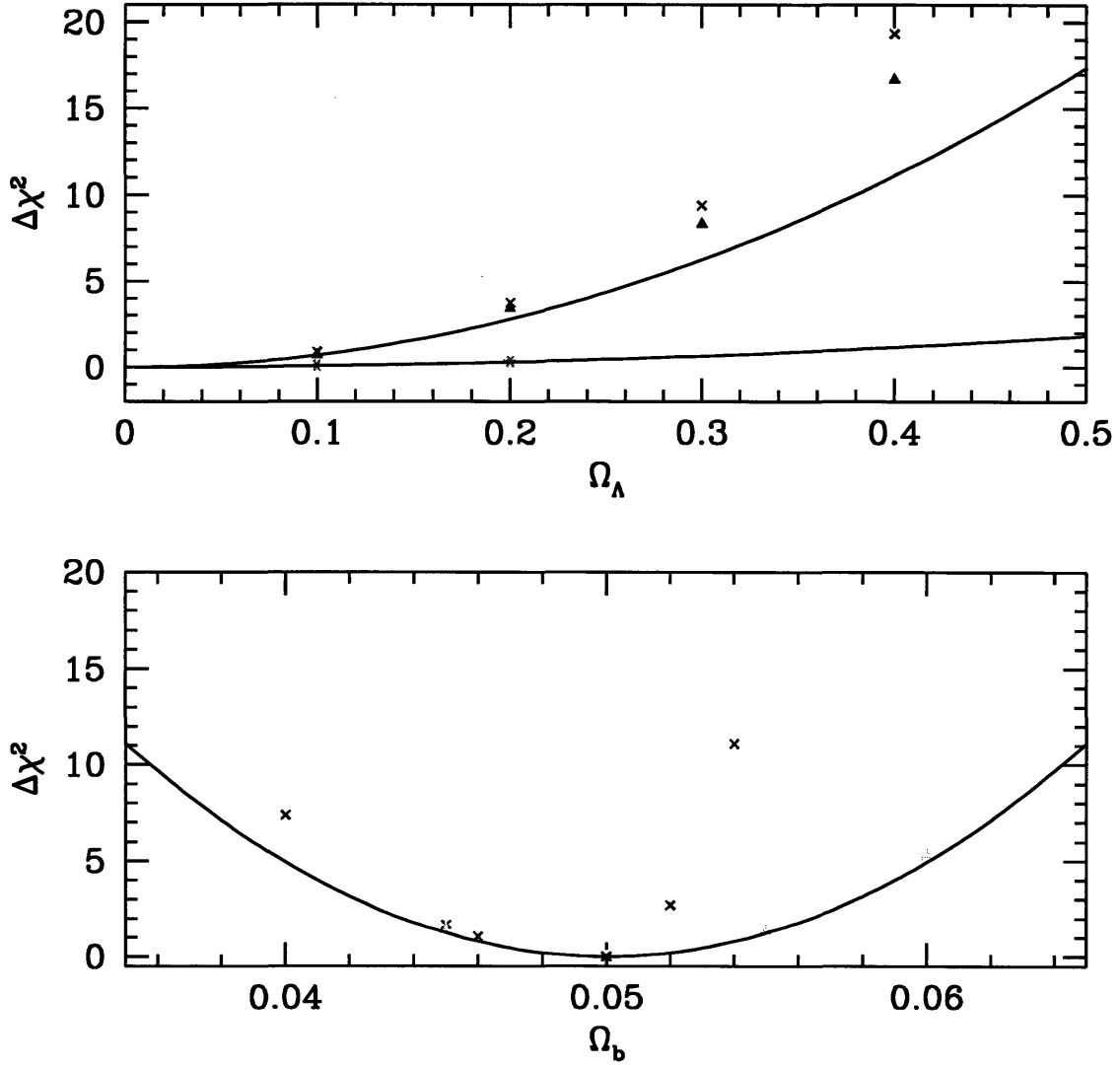
Figure 5-10: Comparison between the Fisher matrix expansion of the likelihood around the minimum (solid lines) and direct minimization for two different cosmological parameters. In most cases the agreement near the minimum is good. In the upper panel full triangles (crosses) correspond to fits of sCDM within the six parameter family described in the text, including (not including) the effects of gravitational lensing. The lower curve belongs to the $T/S = 0.28$ model in the eight parameter space. In the lower panel, the $\Omega_\Lambda > 0$ prior is reached for sCDM when $\Omega_b > 0.05$, which is why the minimization results differ from the Fisher matrix results.

where COBE normalization predicts two times larger small scale normalization than required by the cluster abundance data, the lensing effect is barely noticeable in the error contours for various parameters.

5.5 Conclusions

In this chapter, we have analyzed how accurately cosmological parameters can be extracted from the CMB measurements by two future satellite missions. Our work differs from previous studies on this subject in that we use a more accurate computational code for calculating the theoretical spectra and we include the additional information that is present in the polarization of the microwave background. We also investigate how the results change if we vary the number of parameters to be modeled or the underlying model around which the parameters are estimated. Both of these variations can have a large effect on the claimed accuracies of certain parameters, so the numbers presented here should not be used as firm numbers but more as typical values. Of course, once the underlying model is revealed to us by the observations then these estimates can be made more accurate. The issue of variation of the errors on the number of parameters however remains, and results will always depend to some extent on the prior belief. If, for example, one believes that gravity waves are not generated in inflationary models (e.g. [23]) or that they are related to the scalar perturbations through a simple relation (e.g. [24]), then the MAP errors on most parameters shrink by a factor of 2. Similarly, one may decide that models with both curvature and cosmological constant are not likely, which removes the only inherent degeneracy present in the CMB data.

Using temperature data alone, MAP should be able to make accurate determinations (better than 10%) of the scalar amplitude (σ_8), the baryon/photon ratio ($\Omega_b h^2$), the matter content ($\Omega_m h^2$), the power spectrum slope (n_s) and the angular diameter distance to the surface of last scattering (a combination of Ω and Ω_Λ). If we restrict ourselves to models with no gravity wave content, then MAP should also be able to make accurate determinations of Ω_Λ, the Hubble constant and the optical depth,

κ_{ri}. However, in more general models that include the gravity wave amplitude and spectral slope as additional parameters, the degeneracies between these parameters are large and they cannot be accurately determined.

Several other measurements of the CMB anisotropies from the ground and from balloons are now in progress and accurate results are likely to be available by the time MAP flies. This additional information will help constrain the models further, especially determinations of the power spectrum at the smaller angular scales.

Astronomical data can significantly reduce these degeneracies. The two nearly degenerate models, sCDM and a tilted vacuum dominated model ($\Omega_\Lambda = 0.6$) shown in Figure 5-3 can be distinguished already by current determinations of $\sigma_8 \Omega^{0.6}$, or by measurements of the shape of the galaxy power spectrum, or by measurements of the distance-magnitude relationship with SNeIa's.

MAP's measurements of polarization will significantly enhance its scientific return. These measurements will accurately determine the optical depth between the present and the surface of last scatter. This will not only probe star formation during the "dark ages" ($5 < z < 1300$), but will also enable accurate determination of the Hubble constant and help place interesting constraints on Ω_Λ in models with tensor slope and amplitude as free parameters.

Planck's higher sensitivity and smaller angular resolution will enable further improvements in the parameter determination. Particularly noteworthy is its ability to constrain Ω_Λ to better than 5% and the Hubble constant to better than 1% even in the most general model considered here. The proposed addition of polarization-sensitive bolometer channels to Planck significantly enhances its science return. Planck should be able to measure the ionization history of the early universe, thus studying primordial star formation. Sensitive polarization measurements should enable Planck to determine the amplitude and slope of the gravity wave spectrum. This is particularly exciting as it directly tests the predicted tensor/scalar relations in the inflationary theory and is a probe of Planck scale physics. The primordial gravity wave contribution can at present only be measured through the CMB observations. One may therefore ask how well Planck can determine T/S assuming that other cosmological parameters

are perfectly known by combining CMB and other astronomical data. The answer sensitively depends on reionization optical depth. Without reionization, $T/S \sim 0.1$ can be detected, while with $\kappa_{ri} = 0.1$ this number drops down to $T/S \sim 0.02$. The equivalent number without polarization information is 0.2, regardless of optical depth. Improvements in sensitivity will further improve these numbers, particularly in the B polarization channel which is not cosmic variance limited in the sense that tensors cannot be confused with scalars. A detection of a B component would mean a model independent detection of a stochastic background of gravitational waves or vector modes [8].

The most exciting science return from polarization measurements come from measurements at large angular scales (see Figures 5-6 and 5-7). These measurements can only be made from satellites as systematic effects will swamp balloons and ground based experiments on these scales. The low l measurements enable determinations of the optical depth and the ionization history of the universe and may lead to the detection of gravity waves from the early universe. Both foregrounds and systematic effects may swamp the weak polarization signal, even in space missions, thus it is important that the satellite experiment teams adopt scan strategies and frequency coverages that can minimize systematics and foregrounds at large angles.

We explored the question of how priors such as positivity of certain parameters or constraints from other cosmological probes help reduce the uncertainties from the CMB data alone. For this purpose, we compared the predictions from the Fisher information matrix with those of the brute-force minimization which allows the easy incorporation of inequality priors. As expected, we find that positivity changes the error estimates only on the parameters that are not well constrained by the CMB data. On the other hand, using some additional constraints such as the limits on the Hubble constant, age of the universe, dark matter power spectrum or q_0 measurements from type Ia supernovae can significantly reduce the error estimates because the degeneracies present in these cosmological tests are typically different from those present in the CMB data. The minimization approach also allows testing the assumption that the log-likelihood is well described by a quadratic around the minimum, which is implicit

in the Fisher matrix approach. We find that this is a good approximation close to the minimum, with no nearby secondary minima that could be confused with the global one. Finally, we also tested the effect of gravitational lensing on the reconstruction of parameters and found that its effect on the shape of the likelihood function can be neglected.

In summary, future CMB data will provide us with an unprecedented amount of information in the form of temperature and polarization power spectra. Provided that the true cosmological model belongs to the class of models studied here these data will enable us to constrain several combinations of cosmological parameters with an exquisite accuracy. While some degeneracies between the cosmological parameters do exist, and in principle do not allow some of them to be accurately determined individually, these can be removed by including other cosmological constraints. Some of these degeneracies belong to contrived cosmological models, which may not survive when other considerations are included. The microwave background is at present our best hope for an accurate determination of classical cosmological parameters.

Bibliography

[1] J. R. Bond et. al., Phys. Rev. Lett., **72**, 13 (1994)

[2] L. Knox, Phys.Rev. D 52, 4307 (1995)

[3] G. Jungman, M. Kamionkowski, A. Kosowsky & D. N. Spergel, Phys. Rev. Lett. **76**, 1007 (1996); Phys. Rev. D **54** 1332 (1996)

[4] J. R. Bond, G. Efstathiou & M. Tegmark, Mon. Not. R. Astron. Soc. **291**, 33 (1997)

[5] U. Seljak, Astrophys. J. **482**, 6 (1997)

[6] M. Zaldarriaga & U. Seljak, Phys. Rev. D **55**, 1830 (1997)

[7] M. Zaldarriaga,Phys. Rev. D **55**, 1822 (1997)

[8] U. Seljak & M. Zaldarriaga, Phys. Rev. Lett. **78**, 2054 (1997)

[9] Kamionkowski, M., Kosowsky, A. & Stebbins, A. Phys. Rev. Lett. **78**, 2058 (1997)

[10] U. Seljak & M. Zaldarriaga, Astrophys. J. **469**, 7 (1996)

[11] M. Tegmark, A. N. Taylor & A. F. Heavens, Astrophys. J. **480**, 22 (1997)

[12] M. Tegmark & G. Efstathiou G. MNRAS **281**, 1297 (1996)

[13] D. M. Gay, Computing Science Report No. 153, AT&T Bell Laboratories (1990)

[14] U. Seljak, Astrophy. J. **435**, L87, (1994)

[15] W. Hu & N. Sugiyama,Astrophys. J. **436**, 456 (1995)

[16] L. Kofman & A. Starobinsky, Sov. Astron. Lett. **11**, 271 (1985)

[17] J. A. Peacock, Mon. Not. R. Astron. Soc., **284**, 885 (1997)

[18] V. R. Eke, S. Cole & C. S. Frenk, Mon. Not. R. Astron. Soc. **282**, 263 (1996)

[19] S. Perlmutter, et al. Astrophys. J. **483**, 565 (1997)

[20] Z. Haiman & A. Loeb, Astrophys. J. **483**, 21(1997)

[21] N. Gnedin & J. P. Ostriker, Astrophys. J. **486** ,581 (1997)

[22] U. Seljak, Astrophy. J. **463**, 1, (1996)

[23] D. H. Lyth, Phys. Rev. Lett. **78**, 1861 (1997)

[24] M. S. Turner, Phys. Rev. D **48**, 4613 (1993)

Table 5.1: Fisher matrix one-sigma error bars for different cosmological parameters when only temperature is included. Table 5.3 gives the cosmological parameters for each of the models. Columns with + correspond to MAP and those with × to Planck.

Param.	sCDM$^+$	sCDM$^+$	$\frac{T}{S}=0.28^+$	$\frac{T}{S}=0.1^+$	$\frac{T}{S}=0.1^\times$	$\Omega_\Lambda=0.7^+$	Open$^+$	Open$^\times$
$\Delta\ln C_2^{(S)}$	$2.1\,10^{-1}$	$4.2\,10^{-1}$	$4.8\,10^{-1}$	$4.7\,10^{-1}$	$7.4\,10^{-2}$	$4.1\,10^{-1}$	$1.2\,10^{-1}$	$4.7\,10^{-2}$
Δh	$1.7\,10^{-2}$	$9.2\,10^{-2}$	$1.1\,10^{-1}$	$1.0\,10^{-1}$	$5.1\,10^{-3}$	$4.1\,10^{-2}$	$2.0\,10^{-2}$	$1.1\,10^{-3}$
$\Delta\Omega_\Lambda$	$9.8\,10^{-2}$	$5.3\,10^{-1}$	$6.1\,10^{-1}$	$5.8\,10^{-1}$	$2.9\,10^{-2}$	$5.0\,10^{-2}$	-	-
$\Delta\Omega_b h^2$	$3.0\,10^{-4}$	$1.0\,10^{-3}$	$9.8\,10^{-4}$	$1.2\,10^{-3}$	$1.2\,10^{-4}$	$9.7\,10^{-4}$	$1.1\,10^{-3}$	$1.3\,10^{-4}$
$\Delta\kappa_{ri}$	$1.2\,10^{-1}$	$1.3\,10^{-1}$	$1.4\,10^{-1}$	$1.1\,10^{-1}$	$8.2\,10^{-2}$	$1.9\,10^{-1}$	$7.2\,10^{-2}$	$3.3\,10^{-2}$
Δn_s	$9.8\,10^{-3}$	$5.9\,10^{-2}$	$6.7\,10^{-2}$	$6.4\,10^{-2}$	$5.9\,10^{-3}$	$2.9\,10^{-2}$	$2.4\,10^{-2}$	$3.3\,10^{-3}$
$\Delta\frac{T}{S}$	-	$3.9\,10^{-1}$	$6.8\,10^{-1}$	$5.3\,10^{-1}$	$2.5\,10^{-1}$	$3.2\,10^{-1}$	-	-
Δn_T	-	-	$3.9\,10^{-1}$	$9.1\,10^{-1}$	$9.4\,10^{-1}$	$9.9\,10^{-1}$	-	-
$\Delta\Omega$	-	-	-	-	-	-	$6.6\,10^{-3}$	$5.2\,10^{-4}$

Table 5.2: Fisher matrix one-sigma error bars for different cosmological parameters when both temperature and polarization is included. Table 5.3 gives the cosmological parameters for each of the models. Columns with + correspond to MAP and those with × to Planck.

Param.	sCDM$^+$	sCDM$^+$	$\frac{T}{S}=0.28^+$	$\frac{T}{S}=0.1^+$	$\frac{T}{S}=0.1^\times$	$\Omega_\Lambda=0.7^+$	Open$^+$	Open$^\times$
$\Delta\ln C_2^{(S)}$	$4.8\,10^{-2}$	$2.4\,10^{-1}$	$2.8\,10^{-1}$	$2.4\,10^{-1}$	$1.0\,10^{-2}$	$8.3\,10^{-2}$	$6.5\,10^{-2}$	$1.2\,10^{-2}$
Δh	$1.6\,10^{-2}$	$5.1\,10^{-2}$	$5.8\,10^{-2}$	$5.0\,10^{-2}$	$3.0\,10^{-3}$	$3.8\,10^{-2}$	$1.9\,10^{-2}$	$1.0\,10^{-3}$
$\Delta\Omega_\Lambda$	$9.3\,10^{-2}$	$2.9\,10^{-1}$	$3.3\,10^{-1}$	$2.9\,10^{-1}$	$1.7\,10^{-2}$	$4.6\,10^{-2}$	-	-
$\Delta\Omega_b h^2$	$2.8\,10^{-4}$	$6.1\,10^{-4}$	$7.1\,10^{-4}$	$6.2\,10^{-4}$	$5.7\,10^{-5}$	$8.9\,10^{-4}$	$9.5\,10^{-4}$	$1.1\,10^{-4}$
$\Delta\kappa_{ri}$	$2.1\,10^{-2}$	$2.1\,10^{-2}$	$2.0\,10^{-2}$	$2.0\,10^{-2}$	$5.5\,10^{-3}$	$2.0\,10^{-2}$	$3.2\,10^{-2}$	$3.5\,10^{-3}$
Δn_s	$4.8\,10^{-3}$	$3.1\,10^{-2}$	$3.5\,10^{-1}$	$3.0\,10^{-2}$	$3.0\,10^{-3}$	$2.6\,10^{-2}$	$1.7\,10^{-2}$	$2.6\,10^{-3}$
$\Delta\frac{T}{S}$	-	$2.2\,10^{-1}$	$4.3\,10^{-1}$	$3.0\,10^{-1}$	$4.5\,10^{-2}$	$2.1\,10^{-1}$	-	-
Δn_T	-	-	$3.9\,10^{-1}$	$8.1\,10^{-1}$	$1.7\,10^{-1}$	$7.8\,10^{-1}$	-	-
Δx_e	-	-	-	-	$1.4\,10^{-1}$	-	-	-
$\Delta\Omega$	-	-	-	-	-	-	$6.1\,10^{-3}$	$4.1\,10^{-4}$

Table 5.3: Cosmological parameters for the models we studied. All models were normalized to COBE.

Param.	sCDM	$\frac{T}{S}=0.28$	$\frac{T}{S}=0.1$	$\Omega_\Lambda=0.7$	Open
h	0.5	0.5	0.5	.65	.65
Ω_Λ	0.0	0.0	0.0	0.7	0.0
Ω_b	0.05	0.05	0.05	0.06	0.06
κ_{ri}	0.05	0.05	0.1	0.1	0.05
n_s	1.0	0.96	0.99	1.0	1.0
$\frac{T}{S}$	0.0	0.28	0.1	0.0	0.0
n_T	-	0.04	0.01	-	-
Ω	1.0	1.0	1.0	1.0	0.4

Appendix A

Spin-weighted functions

In this Appendix we review the theory of spin-weighted functions and their expansion in spin-s spherical harmonics. This was used in the main text to make an all-sky expansion of the Q and U Stokes parameters (Chapter 2). The main application of these functions in the past was in the theory of gravitational wave radiation (see e.g. [1]). Our discussion follows closely that of Goldberg et al. [2], which is based on the work by Newman and Penrose [3]. We refer to these references for a more detailed discussion.

For any given direction on the sphere specified by the angles (θ, ϕ), one can define three orthogonal vectors, one radial and two tangential to the sphere. Let us denote the radial direction vector with n and the tangential with $\hat{e}_1$, $\hat{e}_2$. The latter two are only defined up to a rotation around n.

A function $_sf(\theta, \phi)$ defined on the sphere is said to have spin-s if under a right-handed rotation of $(\hat{e}_1, \hat{e}_2)$ by an angle ψ it transforms as $_sf'(\theta, \phi) = e^{-is\psi} \, _sf(\theta, \phi)$. For example, given an arbitrary vector $\mathbf{a}$ on the sphere the quantities $\mathbf{a} \cdot \hat{e}_1 + i\mathbf{a} \cdot \hat{e}_2$, $\mathbf{n} \cdot \mathbf{a}$ and $\mathbf{a} \cdot \hat{e}_1 - i\mathbf{a} \cdot \hat{e}_2$ have spin $1, 0$ and -1 respectively. Note that we use a different convention for rotation than Goldberg et al. [2] to agree with the previous literature on CMB polarization.

A scalar field on the sphere can be expanded in spherical harmonics, $Y_{lm}(\theta, \phi)$, which form a complete and orthonormal basis. These functions are not appropriate to expand spin weighted functions with $s \neq 0$. There exist analogous sets of functions

that can be used to expand spin-s functions, the so called spin-s spherical harmonics $_sY_{lm}(\theta, \phi)$. These sets of functions (one set for each particular spin) satisfy the same completness and orthogonality relations,

$$\int_0^{2\pi} d\phi \int_{-1}^{1} d\cos\theta \, _sY^*_{l'm'}(\theta, \phi) \, _sY_{lm}(\theta, \phi) = \delta_{l'l}\delta_{m'm}$$

$$\sum_{lm} {}_sY^*_{lm}(\theta, \phi) \, _sY_{lm}(\theta', \phi') = \delta(\phi - \phi')\delta(\cos\theta - \cos\theta'). \quad \text{(A.1)}$$

An important property of spin-s functions is that there exists a spin raising (lowering) operator $\eth$ ($\bar{\eth}$) with the property of raising (lowering) the spin-weight of a function, $(\eth \, _sf)' = e^{-i(s+1)\psi}\eth \, _sf$, $(\bar{\eth} \, _sf)' = e^{-i(s-1)\psi}\bar{\eth} \, _sf$. Their explicit expression is given by

$$\eth \, _sf(\theta, \phi) = -\sin^s(\theta)\left[\frac{\partial}{\partial\theta} + i\csc(\theta)\frac{\partial}{\partial\phi}\right]\sin^{-s}(\theta) \, _sf(\theta, \phi)$$

$$\bar{\eth} \, _sf(\theta, \phi) = -\sin^{-s}(\theta)\left[\frac{\partial}{\partial\theta} - i\csc(\theta)\frac{\partial}{\partial\phi}\right]\sin^s(\theta) \, _sf(\theta, \phi) \quad \text{(A.2)}$$

In this paper we are interested in polarization, which is a quantity of spin ±2. The $\bar{\eth}$ and $\eth$ operators acting twice on a function $_{\pm2}f(\mu, \phi)$ that satisfies $\partial_\phi \, _sf = im \, _sf$ can be expressed as

$$\bar{\eth}^2 \, _2f(\mu, \phi) = \left(-\partial\mu + \frac{m}{1 - \mu^2}\right)^2 \left[(1 - \mu^2) \, _2f(\mu, \phi)\right]$$

$$\eth^2 \, _{-2}f(\mu, \phi) = \left(-\partial\mu - \frac{m}{1 - \mu^2}\right)^2 \left[(1 - \mu^2) \, _{-2}f(\mu, \phi)\right], \quad \text{(A.3)}$$

where $\mu = \cos(\theta)$. With the aid of these operators one can express $_sY_{lm}$ in terms of the spin zero spherical harmonics Y_{lm}, which are the usual spherical harmonics,

$$_sY_{lm} = \left[\frac{(l - s)!}{(l + s)!}\right]^{\frac{1}{2}} \eth \, ^sY_{lm} \quad, (0 \leq s \leq l)$$

$$_sY_{lm} = \left[\frac{(l + s)!}{(l - s)!}\right]^{\frac{1}{2}} (-1)^s \bar{\eth} \, ^{-s}Y_{lm} \quad, (-l \leq s \leq 0). \quad \text{(A.4)}$$

165

The following properties of spin-weighted harmonics are also useful

$$
\begin{aligned}
{}_sY^*_{lm} &= (-1)^s {}_{-s}Y_{l-m} \\
\eth \, {}_sY_{lm} &= [(l-s)(l+s+1)]^{\frac{1}{2}} \, {}_{s+1}Y_{lm} \\
\bar{\eth} \, {}_sY_{lm} &= -[(l+s)(l-s+1)]^{\frac{1}{2}} \, {}_{s-1}Y_{lm} \\
\bar{\eth}\,\eth \, {}_sY_{lm} &= -(l-s)(l+s+1) \, {}_sY_{lm}
\end{aligned}
\tag{A.5}
$$

Finally, to construct a map of polarization one needs an explicit expression for the spin weighted functions,

$$
{}_sY_{lm}(\hat{n}) = e^{im\phi} \left[\frac{(l+m)!(l-m)!}{(l+s)!(l-s)!} \frac{2l+1}{4\pi} \right]^{1/2} \sin^{2l}(\theta/2)
$$
$$
\times \sum_r \binom{l-s}{r} \binom{l+s}{r+s-m} (-1)^{l-r-s+m} \cot^{2r+s-m}(\theta/2).
\tag{A.6}
$$

For the special case $|s| = 2$ a more useful expression (2.13) is provided in Chapter 2.

Bibliography

[1] K. S. Thorne, Rev. Mod. Phys. **52**, 299.

[2] J. N. Goldberg *et al.*, J. Math. Phys. **8**, 2155 (1967).

[3] E. Newman and R. Penrose, J. Math. Phys. **7**,863 (1966).